Investigation of K$^+$ meson production in C + C collisions at 2 A GeV with HADES

Alexander Sadovsky

Februar 2007

WISSENSCHAFTLICH-TECHNISCHE BERICHTE

Alexander Sadovsky

Investigation of K+ meson production in C + C collisions at 2 A GeV with HADES

**Forschungszentrum**
Dresden Rossendorf

Institut für Kern- und Teilchenphysik
Fakultät Mathematik und Naturwissenschaften
Technische Universität Dresden

Investigation of K^+ meson production in C + C collisions at 2 A GeV with HADES

Dissertation

zur Erlangung des

akademischen Grades

Dr. rer. nat.

vorgelegt von

Alexander Sadovsky

geboren am 10.08.1974 in Protvino/Russische Föderation

Dresden   2007
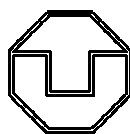
Eingereicht am 16. Juni 2006

1. Gutachter: Prof. Dr. E. Grosse

2. Gutachter: Prof. Dr. B. Kämpfer

3. Gutachter: Prof. Dr. J. Stroth

Verteidigt am 24. Januar 2007

Contents

List of Figures

List of Tables

1   Introduction

1.1   Heavy-ion collisions

When two heavy ions collide, a considerable compression and heating of the nuclear matter occurs in the overlap region, often called fireball. In contrast to high-energy particle physics, where new particle species and their interactions are studied in vacuum, experiments with heavy ions are focused on studying particle properties in dense nuclear matter as well as the behavior of the matter itself.

Studying collisions of compound objects, such as atomic nuclei, posed new challenging requirements to the experimental techniques, like the ability to detect high multiplicities of the reaction products. In parallel, an adequate description of the complex interactions taking place in heavy-ion collisions was needed and lead to dedicated theoretical developments for interpretations of experimental results.

1.1.1   Phase diagram of nuclear matter

Similar to macroscopic matter at normal conditions on Earth, it is expected that the nuclear matter also appears in different phases, depending on some measurable parameters (see Fig. 1.1). These parameters are the temperature T, which is a measure of the average kinetic energy of the particles and the baryonic chemical potential[1] μ_B, which is related to the density ρ at a certain temperature.

The connection to the baryonic density can be established within the thermodynamical approach. The baryonic number densities are given by grand canonical ensemble of non interacting fermions (see e.g. [Lan76]). In each co-moving reference frame the baryonic particle densities are given as integrals over particle momenta $\mathbf{k}$:

$$\rho_i = g_i \int \frac{d^3\mathbf{k}}{(2\pi)^3} \frac{1}{e^{(E_i - \mu_B)/T} + 1},$$

(1.1)

where ρ_i is the density for baryon species $i = \{p, n, \Lambda, ...\}$, g_i is the corresponding spin-isospin degeneracy factor, $\mathbf{k}$ is the momentum and E_i is the total energy of the baryon (in free gas approximation $E_i = \sqrt{m_i^2 + \mathbf{k}^2}$). Therefore, at a given temperature, μ_B determines the density. This relation allows a qualitative translation of the phase diagram from the (T, μ_B) parameterization to the (T, ρ_B) parameterization similar to the classical description in temperature and density.

---

[1] Under the baryonic chemical potential of nuclear matter μ_B one understands the energy which is needed to remove one baryon from the closed system. In the quark-gluon plasma region of phase diagram the baryon potential is defined via corresponding quark content $\mu_B = 3\,\mu_q$.

According to our current understanding at least two phases of the nuclear matter, a "liquid phase" ($T < 16 \, \text{MeV}$) and a "hadron gas" are possible to distinguish, while some more phases are predicted, see Fig. 1.1.
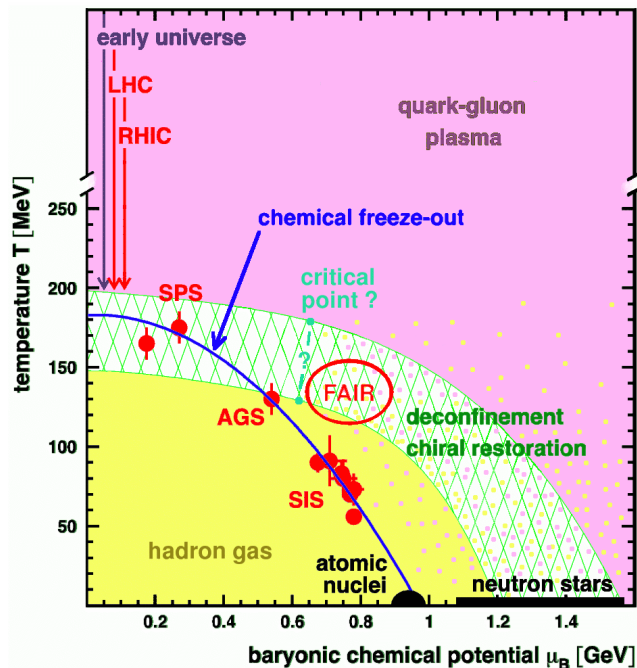
Figure 1.1: Sketch of phase diagram of hadronic matter. The hadron gas phase (yellow region) and the quark gluon plasma phase (purple region indicating quark deconfinement and chiral restoration) are separated by the green hashed area illustrating a possible phase transition between the first two. The possibility of a critical point is indicated ($?$) in cyan color. The temperature T and the baryonic potential μ_B are derived from yield ratios of particles produced in nucleus-nucleus collisions. Red full circles are experimental results [Ave97, Bra95, Bra95, Hon98a, Sto98]. The blue solid curve through the data points represents chemical freeze-out of hadronic matter. The picture is taken from [Sen99, Ave97] and modified for illustrational reasons. The abbreviations for various accelerators are explained in text.

The term "liquid phase" of nuclear matter originates from observations made in nuclear physics. Ordinary nuclei can be described by the droplet model, where protons and neutrons behave like atoms of a liquid, i.e. without much friction, allowing no compression or spatial overlap. Characteristic temperatures are up to $16 \, \text{MeV}$ and densities are about the saturation value of nuclear density $\rho_0 \approx 0.17 \, \text{nucleon/fm}^3$.

The hadron gas is a phase, which can be created from liquid phase by adding a sufficient amount of energy, for example in nucleus-nucleus collisions at relativistic energies. It is characterized by higher temperatures, about $20...200 \, \text{MeV}$, and densities lower or somewhat higher than ρ_0. In the hadron gas phase, the so called "chemical freeze-out" of hadrons at a later expansion stage of heavy-ion collisions happens. Basing on the framework of a statistical model assuming that the system leaves chemical equilibrium, observed hadron multiplicities can be converted into common values of T and μ_B, then serving as land markers in the phase diagram. In Fig. 1.1, points accessed by different experiments on the set of existing accelerators (see below) are depicted together with an interpolating curve.

One can further consider a "solid phase" for nuclear matter as the states which might be realized in the crust of neutron stars [Mag02], where internal excitations (temperature) are low but the density is high compared to the ρ_0. Some arguments [Pet98] suggest that under these conditions liquid crystal phases are realized, rather than rigid solids.

At much higher temperatures where quarks are no longer confined inside hadrons, the so-called "quark-gluon plasma" phase is predicted. This state of matter may have existed in the early universe during the first moments after the Big Bang and could be found today

in the core of dense stellar objects such as neutron stars. The quark-gluon plasma phase is subject to heavy-ion collision experiments at ultrarelativistic energies.

Similar to known macroscopic materials, it is expected that in nuclear matter there are phase transitions between different states as well. The phase transitions between the hadron gas and quark-gluon plasma can be related to the restoration of chiral symmetry. If such effects are confirmed, one may further assume the existence of a critical point at the transition curve between the hadron gas and quark-gluon plasma phases.

To investigate this possibility, several heavy-ion collision experiments with various ion beams (with respect to the ion mass and the beam energy) cover different regions of the phase diagram. The already performed experiments at AGS, SPS and SIS[2] are depicted by red points, the access region of LHC at CERN and RHIC in Brookhaven[3] are indicated with arrows while a corresponding estimate for the GSI future project FAIR is emphasized by the red oval in Fig. 1.1. The corresponding heavy-ion beams of SIS-18, AGS, SIS-100/300, SPS, RHIC and LHC have kinetic energies up to $4(Z/A)$ GeV, $29(Z/A)$ GeV, $45(Z/A)$ GeV, $400(Z/A)$ GeV, $\sqrt{s} = 200$ AGeV and[4] $\sqrt{s} = 5.5$ ATeV, where Z denotes the charge and A is the mass number of the projectile nuclei.

The represented processes cover an extended energy-density range from interstellar vacuum till supernova explosions and neutron stars. However, only a limited fraction of these states can be achieved under laboratory conditions. Since the technical ability to place a detector inside the hot and dense nuclear matter does not exist yet, many of our measurements are limited to the late (freeze-out) stage of the time evolution, where most of the interesting processes have already been completed. Directly accessed can only be the final reaction products after they have cooled down. Therefore, experimentalists often rely on indirect observations supported by theoretical models describing the dynamic evolution of matter from the early stage on. In contrast, direct probes, such as photons or dileptons probe the entire course of a heavy-ion collisions. Other observables are sensitive to stages, where maximum densities and temperatures are achieved.

1.1.2 Equation of state of nuclear matter

The intermediate state of a heavy-ion collision may involve as many as 500 particles already at energies of 0.1 AGeV in a small volume, while at high energies around 100 AGeV the number of particles involved in a reaction may go up to several thousand [Cse94]. Such a small system can be already a subject of application for statistical and kinetic physics description. Both equilibrium and non-equilibrium processes may occur at different stages of the collision, sometimes one can identify and study them separately.

The bulk thermodynamic properties of nuclear matter in statistical equilibrium (or near equilibrium) are described to a large extent by the Equation of State (EOS), a relation between three thermodynamic variables. The common selection of the variables in nuclear matter is the internal energy E, the temperature T and the density ρ. The internal energy can be represented as a sum of two parts: a thermal excitation energy per nucleon $E_{thermal}$

---

[2]The acronyms denote the accelerators AGS (Alternating Gradient Synchrotron at Brookhaven National Laboratory, Long Island), SPS (Super Proton Synchrotron at the European Organization for Nuclear Research, CERN in Geneva) and SIS (Schwerionen Synchrotron at GSI, Darmstadt).

[3]LHC (Large Hadron Collider) at CERN, RHIC (Relativistic Heavy-Ion Collider) at BNL.

[4]$\sqrt{s}$ means the total energy per nucleon pair in the center of mass system.

and a compressional part E_{compr}. Therefore, the EOS can be written as [Sto86b]

$$E(\rho, T) = E_{thermal}(\rho, T) + E_{compr}(\rho, T = 0) + E_0, \tag{1.2}$$

where E_0 stands for the ground state energy per nucleon, see also the illustration in Fig. 1.2. The excess of total energy of the system above the $T = 0$ isocurve is stored in the thermal
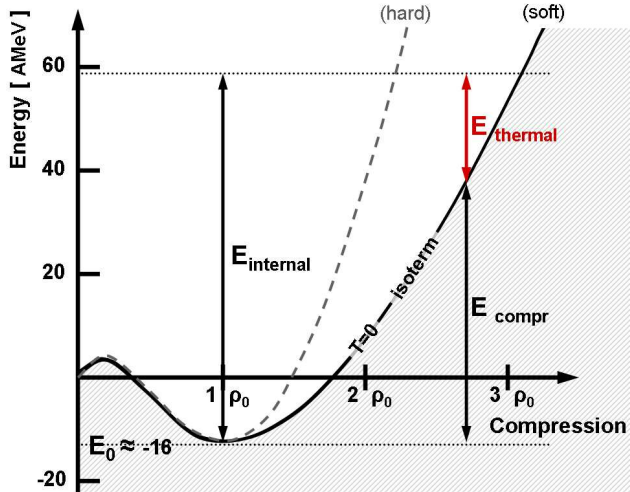
Figure 1.2: A schematic illustration of density dependence of various energy terms used for the equation of state. The black solid curve stands for compressional energy at $T = 0$ corresponding to a soft EOS (high compressibility), while the dashed curve corresponds to a hard EOS (low compressibility). The thermal energy is the excess energy above the $T = 0$ isocurve. The compressional energy E_{compr} is a part of internal energy characterizing the achieved compression of baryonic matter. See text for more details.

excitation energy (which is zero at $T = 0$, by definition). The compressional energy E_{compr} is zero for isospin-symmetric matter at normal nuclear density $\rho = \rho_0$ ($\rho_0 \approx 0.17$ nucleon$/fm^3$, $E_0 \approx -16$ MeV per nucleon, considering a nuclear state of infinite volume, i.e. an idealized system without Coulomb and surface forces) and grows with compression[5]. Therefore, the compressional energy E_{compr} is defined as the energy excess with respect to the energy E_0 of extended nuclear matter in the ground state.

The isothermal incompressibility of the nuclear matter κ is defined by the second order derivative over the particle number density at the ground state, $\rho = \rho_0$, as

$$\kappa = 9\rho_0^2 \left(\frac{\partial^2 E_{compr}}{\partial \rho^2} \right)_{\rho = \rho_0, T = 0}. \tag{1.3}$$

It provides second order Taylor expansion of compressional energy as a function of density. Once κ is known, we have access to a universal equation of state near ρ_0, which is applicable in heavy-ion collisions, but also in processes held at early stage of universe and, in particular, in neutron stars. The higher the incompressibility is, the more energy is stored in compression, the less thermal energy is available at a certain density. This is directly related to the number (multiplicity) of secondary particles produced in the heavy nuclei reaction reaching a certain density. Thus, a lower incompressibility causes higher multiplicity of secondary particle production [Stu01b] at certain nuclear density $\rho > \rho_0$.

An experimental measurement of incompressibility can be performed accessing different nuclear densities by using ion beams of different atomic number in relativistic ion collisions. Observations of giant isoscalar monopole resonances [You99, Pie04] offer another approach

---

[5] The ground state energy for an average nucleus is different $E_0^{nucleus} \approx -8$ AMeV due to the compression caused by Coulomb and surface forces [Sto86b].

to estimate the incompressibility. In addition, the observation of in-plane sidewards flow of nucleons in near-central heavy-ion collisions at ultrarelativistic energies [Sto86b] and, especially, near-threshold production of K^+ mesons in heavy-ion reactions at energies around 1 AGeV [Aic85a, Har06] must be sensitive with respect to the EOS compressibility. Some details of the latter aspect are discussed in section 1.2.

When global equilibrium is not reached, the EOS can be still applied in certain cases, e.g. assuming local equilibrium in time or in space. Therefore, statistical concepts have been successfully applied in theoretical description of nuclear collisions.

1.1.3 In-medium effects

The Standard Model (SM) of particle physics, developed in early 1970s had great success in explaining experimental results. It requires at least 19 different input parameters whose values must be derived from measurements, among them are quark masses, stemming from symmetry breaking in the electroweak sector via Higgs mechanism. The masses of hadrons in vacuum are not free parameters, and they are calculable from Quantum Chromo-Dynamics (QCD). An interesting question concerns the behavior of hadrons embedded in a strongly interacting medium, e.g. nuclear matter.

From atomic physics it is known that the spectral lines of atoms are affected (shifts, splitting) by the external electromagnetic fields and it can be understood within the framework of Quantum Electro-Dynamics (QED). QCD treats hadrons as vacuum excitations, therefore, similar modifications of their properties may occur, when they are surrounded by strongly interacting matter [Koc97]. More generally speaking, the spectral functions of hadrons will be modified. In a simplified notion, mass shifts and/or broadening of resonance widths at higher baryon densities and temperatures are expected. Phrased in a conventional way, studying mass changes of hadrons may contribute to understanding the phenomenon of "mass of particle".

Particularly for vector mesons, early predictions were based on the Brown-Rho scaling hypothesis [Bro91], where the masses of the light vector mesons are assumed to be proportional to the chiral quark condensate, $m_V^2 \sim <\bar{q}q>$. A non-vanishing value[6] of the quark condensate $<\bar{q}q>$ expresses the spontaneous breakdown of chiral symmetry. Nowadays this simplistic relation is revised, but the idea behind remains the same: masses of light mesons are connected to the quark condensate $<\bar{q}q>$ and other condensates. $<\bar{q}q>$ plays a role of an order parameter for the chiral restoration transition; it goes to zero at a critical temperature or density and seems to coincide with deconfinement.

Recently, see e. g. [Rup06], Brown-Rho scaling is discussed with respect to scaling of in-medium vector meson masses with the quark condensate according to the relation

$$\frac{m_V^*}{m_V} = \left(\frac{<\bar{q}q>^*}{<\bar{q}q>} \right)^\alpha , \qquad (1.4)$$

where α corresponds to scaling parameter (e.g. $\alpha = 1/2$ for the original Brown-Rho scaling, but also 1/3, 1/4, etc.), m_V^* corresponds to in-medium mass of vector meson and m_V is the one in vacuum. For small values of ρ and T, the change of $<\bar{q}q>$ can be determined from

---

[6] The Gell-Mann-Oakes-Renner relation [Gel68] establishes a relation between pion mass and decay constant on one side and the quark condensate expectation value in vacuum and quark current masses on another side, resulting to $<\bar{q}q>_0 \approx (-230 \, \text{MeV})^3 \simeq -1.6 \, \text{fm}^{-3}$, [Wei96].

first principles with same approximation. The change of the chiral quark condensate value with nuclear density as well with temperature is shown in Fig. 1.3. Based on the chiral quark condensate the vector meson mass change in a medium is estimated [Zsc02] exploiting the QCD sum rules technique.
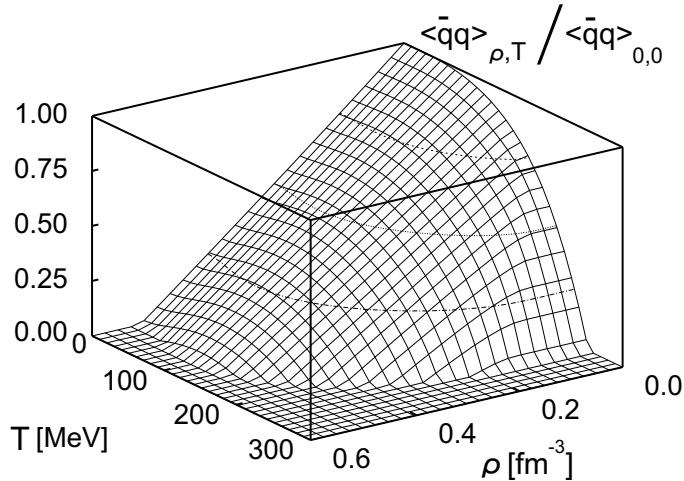
Figure 1.3: The dependence of quark condensate $| < \bar{q}q > |$ on density and temperature of nuclear medium at small densities and temperatures (the theoretical approach is reliable for densities $\rho < \rho_0$ and temperatures $T < 100\,\mathrm{MeV}$, but the plot is extrapolated to higher values of ρ and T). Figure from [Zsc02].

A suitable, but technically challenging way to experimentally access the properties of vector mesons in matter is to measure the products of their dileptonic decays [Hua94, Ull96]. These leptons carry the information out of the decay region practically undisturbed by the surrounding hadronic matter due to the low electroweak interaction probability. The main focus of the HADES experiment to be described in detail below lies in this research topic.

Various hadronic models have been proposed, many of them deliver even qualitatively different estimates. To resolve the situation, experimental evidence is required. Predictions on in-medium effects for hadrons are shown for example in [Wei96]. In-medium modifications for pions are expected to be small, while for strange mesons observable changes are predicted and presumably experimentally verified. Charged kaons turned out to be a sensitive probe. In particular, the effective masses of $K^{\pm}$ mesons undergo splitting as a function of nuclear matter density [Sch94, Kol95, Lee96, Waa96], see for example Fig. 1.4.
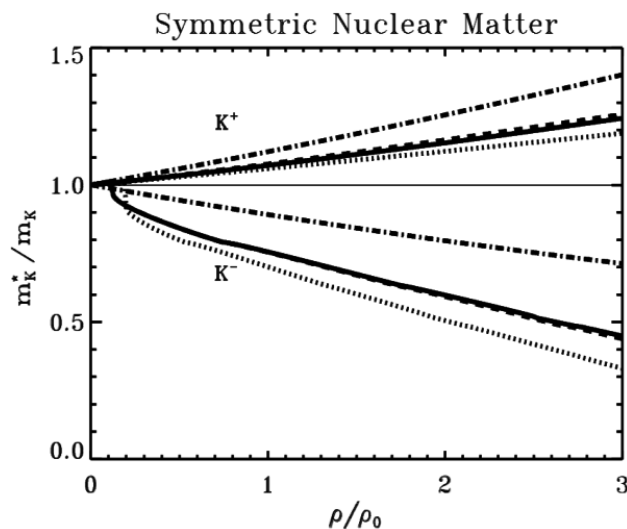
Figure 1.4: Effective K^+ and K^- masses in symmetric nuclear matter $\rho_n \approx \rho_p$ as a function of nuclear density $\rho = \rho_n + \rho_p$ for several approaches in evaluation of effective Lagrangian taking into account Pauli blocking and nucleon-nucleon short range correlations. Several theoretical assumptions are depicted with different lines, all of them predict an observable K^+–K^- mass splitting growing with nuclear density, see [Waa96] for details.

The experimental results on K^+, K^- in-medium effects can be condensed in density dependence of the effective masses $m^*_{K^+} = (1 + \frac{\rho}{\rho_0}V_{K^+})m_{K^\pm}$ with slightly repulsive K^+ potential $V_{K^+} \approx (20...30)\,\text{MeV}$ and $m^*_{K^-} = (1 + \frac{\rho}{\rho_0}V_{K^-})m_{K^\pm}$ with attractive K^- potential $V_{K^-} \approx -(80...110)\,\text{MeV}$, where ρ and ρ_0 are nuclear densities in medium and in vacuum, see [Cas99, Her96, Sch06].

The knowledge of in-medium properties of hadrons, especially K^- mesons, provide important ingredients for the understanding of astrophysical phenomena, like supernova explosions and formation of neutron stars [Gle01].

1.2   Kaon production in heavy ion collisions

Partial chiral symmetry restoration is thought to influence the yield of strange particles production in heavy-ion collisions[7]. It lowers the energy threshold of quark-antiquark production and enhances the fraction of strange quark $\bar{s}s$ pair production. Strange quarks couple with other non-strange quarks forming strange hadrons in case of subsequent freeze out, see table 1.1. Some properties of $K^\pm$, K^0 and $\overline{K}^0$, known from particle physics are listed in table 1.2.

meson	K^+	K^-	K^0	$\overline{K}^0$
quarks	$u\bar{s}$	$\bar{u}s$	$d\bar{s}$	$\bar{d}s$

Table 1.1: Quark structure of kaons.

Kaons, $K^\pm$, K^0, $\overline{K}^0$ together with $\pi^\pm$, π^0 and η are Goldstone bosons in $SU(3)$ flavor quark symmetry and can be systematically presented as members of an SU(3) octet, see Fig. 1.5.
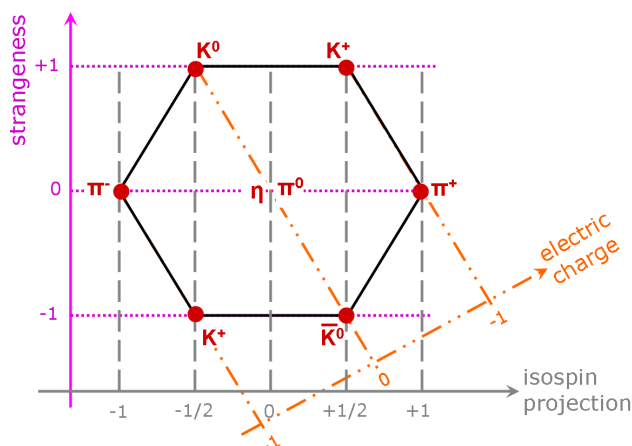
Figure 1.5: The octet of pseudoscalar mesons. The picture is taken from [Muh74] and modified for illustrational reasons.

---

[7]In contrast to the explicitly broken chiral symmetry, where effective quark masses are of the order of several hundred MeV, in the case of the partial chiral symmetry restoration the effective masses of the quarks are reduced to their current masses ($m_u \approx m_d$ around several MeV, and $m_s \approx 150\,\text{MeV}$).

meson	K^+	K^-	K_S^0	K_L^0
CP operator eigenstate	$\|K^+>$	$\|K^->$	$\|K_S^0>$	$\|K_L^0>$
in terms of strangeness operator eigenstates	$\|K^+>$	$\|K^->$	$\frac{(\|K^0>-\|\overline{K^0}>)}{\sqrt{2}}$	$\frac{(\|K^0>+\|\overline{K^0}>)}{\sqrt{2}}$
mass	493.68 MeV/c^2		497.67 MeV/c^2	
mean life time τ	$1.238{\cdot}10^{-8}$ s		$0.896{\cdot}10^{-10}$ s	$5.18{\cdot}10^{-8}$ s
$c\tau$	3.713 m		2.676 cm	15.51 m
dominant decay channels with branching (BR>1%)	$\mu^+\nu_\mu$ (63.4%) $\pi^+\pi_0$ (21.1%) $\pi^+\pi^+\pi^-$ (5.6%) $\pi^0\mu^+\nu_\mu$ (3.3%)	charge conjugates to K^+ decay modes	$\pi^+\pi^-$ (69.0%) $\pi^0\pi^0$ (31.0%) other $<1\%$	$\pi^\pm e^\mp\nu_e$ (38.8%) $\pi^\pm\mu^\mp\nu_e$ (27.2%) $3\pi^0$ (21.1%) $\pi^+\pi^-\pi^0$ (13.0%)

Table 1.2: Properties of pseudoscalar ($isospin(spin^{parity}) = \frac{1}{2}(0^-)$) kaon ground states, from [Eid04].

The interest in the investigation of K^+ and K^- meson production in physics of relativistic ion collisions is suggested by their quark content and predictions from theoretical models toward the expected in-medium modifications (see section 1.1.3).

The formation of a new hadron requires the creation of quark-antiquark pairs and subsequent rearrangements with the quarks forming the original nuclei. In case of strange quarks, the quark and antiquark from an $s\bar{s}$ pair mixes with light u and d quarks in medium forming strange particles. In practice one observes them in associated strangeness production, see e.g. [Gaz96]. Various processes related to $K^\pm$ production in heavy-ion collisions at intermediate energies are summarized in table 1.3.

K^+	K^-	Type
$BB \to BYK^+$	$BB \to BBK^+K^-$	Strangeness production primary/secondary
$\pi B \to YK^+$	$\pi B \to BK^+K^-$	Strangeness production secondary
	$BY \to BBK^-$	Strangeness exchange
	$\pi Y \to BK^-$	Strangeness exchange
$YK^+ \to \pi B$		Strangeness absorption
$BK^+ \leftrightarrow BK^{+/0}$	$BK^- \leftrightarrow BK^-(\overline{K^0})$	Elastic/charge exchange

Table 1.3: Elementary hadronic reactions relevant to kaon dynamics in heavy-ion collisions at intermediate energies according to [Fuc06]. Here B stands for nucleon or nucleon resonance (N, Δ, N^*), while Y for the hyperon Λ or Σ. Under abbreviation $BK^+ \leftrightarrow BK^{+/0}$ one understands, e.g. $pK^+ \leftrightarrow pK^+$, $pK^+ \leftrightarrow nK^0$ reactions, while under $BK^- \leftrightarrow BK^-(\overline{K^0})$, correspondingly $pK^- \leftrightarrow pK^-$, $pK^- \leftrightarrow n\overline{K^0}$.

For not too high beam energies in nucleus-nucleus or nucleon-nucleon collisions there is a high population of light quarks brought in by the projectile nucleons. Consequently, the reabsorption of the antiquark from the newly created $u\bar{u}$ or $d\bar{d}$ pair is a frequent process. Therefore, pions created at high nuclear density of the collision should undergo several reabsorptions and leave the interaction zone without clear information on early stages of the fireball.

For antiquarks originating from heavy quark pairs, $s\bar{s}$ or $c\bar{c}$, the reabsorption is rare, due to the low population of corresponding heavy quarks in the fireball. The reason is that a strange quark is not a part of proton or neutron and can only be created independently as a part of $s\bar{s}$ pair. Therefore, strange quarks and antiquarks live in hadrons until they undergo weak decay via Cabibbo-Kobayashi-Maskawa mixing $s(\bar{s})$ into $u(\bar{u})$ with subsequent annihilation of light quarks. This affects the properties of K^{+} mesons since they contain a heavy antiquark, in addition, the u quark of K^{+} meson feels a repulsive potential from the nucleons of in medium (repulsive $K^{+}N$ potential). Thus, K^{+} mesons have a long mean free path in nuclear medium ($\lambda \approx 5\,\mathrm{fm}$ [Dov77, Dov82]). This suggests that the measured properties of K^{+} mesons would characterize to a large extend the original conditions inside the nuclear medium. For light nuclei it must be already sufficient to leave undisturbed by the fireball region. Concerning the K^{+} production, in the reaction of ^{12}C+^{12}C (which is analyzed in this thesis) it should be still valid. The estimate of ^{12}C radius is $r = r_0 \cdot A^{1/3} \approx 2.74\,\mathrm{fm}$ ($r_0 \approx 1.2\,\mathrm{fm}$), i.e. the diameter is about the mean free path. Thus, experimental studies of the K^{+} production with this system is of particular interest.

In-medium potentials are essential ingredients of transport models of heavy ion collisions. The repulsive in-medium $K^{+}N$ potential affects the K^{+} mass shift up (while the attractive $K^{-}N$ potential shifts K^{-} mass down) according to various transport models as already mentioned in section 1.1.3 (see also Figure 1.4).

Kaon production in heavy-ion collisions near the threshold beam energies[8] is sensitive to the compressibility of nuclear matter [Aic85b, GQL95]. This makes an experimental study so interesting. Observations made for sub-threshold production of K^{+} in heavy-ion collisions involves collective effects, such as multiple nucleon-nucleon collisions (e.g. where the internal Fermi motion of nucleons is required to be added to the relative kinetic energy of two nucleons to be sufficient for the kaon production) as well as secondary processes like $\pi N \rightarrow K^{+}\Lambda$. The conclusions [Fuc97] concern the nuclear equation-of-state and can be used for a comparison with the predictions from transport models. From another side, some decrease of K^{+} yield in the dense matter due to the increase of the K^{+} production energy can be expected due to the repulsive $K^{+}N$ potential, according to [Sch97].

In contrast, the K^{-} meson feels an attractive $K^{-}N$ potential due to presence of the $\bar{u}$ antiquark in it. This makes it favorable for the interaction with light quarks in a nuclear medium. Thus it can not be used as a convenient probe for a direct information on the early stage of the fireball. Due to the expected decrease of K^{-} meson effective mass with increasing density it must be strongly influenced by the compressibility of matter. Therefore it can be used to determine the nuclear Equation of State.

The production of both K^{+} and K^{-} mesons was studied by the KaoS experiment [Stu01b] with heavy ^{197}Au + ^{197}Au and light ^{12}C + ^{12}C systems at different beam energies. Results were explained with a "soft" Equation of State [Fuc01, Fuc06] with an incompressibility around $\kappa = 200\,\mathrm{MeV}$.

---

[8]E.g. $E_{beam}^{threshold} = 1.58\,GeV$ for $NN \rightarrow K^{+}\Lambda N$ and $E_{beam}^{threshold} = 2.5\,GeV$ for $NN \rightarrow K^{+}K^{-}NN$

Some experiments related to charged kaon production delivered differential cross sections in limited phase spaces and yield ratios like $K^{\pm}/\pi^{\pm}$, K^+/K^- for several energies and colliding systems [Sch82, Sho82, Abb90a, Mis94, Pan95, Deb96, Elm96, Ahn97, Bar97, Sch00]. Other put efforts in extrapolations to total K^+ production cross section, see e.g. [Sch89] for p + A and A + A data, see also the compilation of [Gaz96] for p + p data, [Sch06] for p + C and p + Au data and [Ahl98, Bes97, Ahl99, Lau99, Lau00, Men00, Stu01b] for heavy ion collisions. The total K^+ yields for kinetic beam energies around 2 GeV/nucleon are summarized in tables 1.4 and 1.5. It was noticed [Lau00] that, in contrast to pions, the values for K^+ multiplicities per nucleon, $M(K^+)/<A_{part}>$, are very similar for C+C and C+Au collisions at 1 AGeV and 1.8 AGeV.

E_{beam} [AGeV]	system	$N(K^+)$	T [MeV]	σ_{tot} [mb]	reference
0.78	Au+Au	1200	67 ± 4	8.5 ± 1.2	[Stu01b]
0.96	Au+Au	3200	82 ± 4	31 ± 4.0	
1.10	Au+Au	1100	90 ± 6	64 ± 10	
1.46	Au+Au	2900	100 ± 5	267 ± 30	
1.00	C+Au	770	68 ± 5	1.2 ± 0.2	[Lau00]
1.80	C+Au	13000	80 ± 6	30 ± 5	
1.00	Ni+Ni	1280	75 ± 6	2.7 ± 0.5	[Bar97]
1.80	Ni+Ni	9360	88 ± 7	57 ± 15	
1.06	Ni+Ni	120		3.5 ± 0.9	[Bes97]
1.45	Ni+Ni	500		20 ± 5	(*)
1.93	Ni+Ni	3000		87 ± 22	
1.00	C+C	1200	58 ± 6	0.1 ± 0.02	[Lau99]
1.20	C+C	2400	64 ± 4	0.3 ± 0.05	
1.50	C+C	7000	74 ± 5	1.3 ± 0.2	
1.80	C+C	17000	75 ± 5	3.0 ± 0.3	
2.00	C+C	11000	78 ± 5	5.0 ± 0.5	
2.10	Ne+NaF		122	23 ± 8	[Sch89]
2.10	Ne+Pb			150 ± 90	[Sch82]
2.10	d+NaF			2.4 ± 0.8	
2.10	d+Pb			14 ± 5	
2.10	p+NaF			1.8 ± 0.6	
2.10	p+Pb			11 ± 4	
1.60	p+C		45.6	0.070 ± 0.006	[Sch06]
2.50	p+C		69.9	0.89 ± 0.08	
3.50	p+C		88.2	2.04 ± 0.25	
1.60	p+Au		49.0	0.83 ± 0.05	[Sch06]
2.50	p+Au		73.0	8.53 ± 0.95	
3.50	p+Au		90.8	20.74 ± 1.69	
2.90	p+Be			3.7 ± 1.5	[Bue96]

Table 1.4: Yields of K^+ mesons in A + A and p + A reactions with beam kinetic energies around 2 AGeV for various systems extrapolated to 4π. For some reactions, also the number of detected kaons and the temperature parameter T can be presented. Results marked with star (*) report the production probability but are scaled here to σ_{tot}.

P_{beam} [GeV/c]	E_{beam} [GeV]	system	multiplicity	σ_{tot} [μb]	reference
3.2	2.40	p+p	$(2.6 \pm 0.7) \cdot 10^{-3}$	(71 ± 18)	[Ree68]
3.349	2.54	p+p	$(2.2 \pm 0.4) \cdot 10^{-3}$	(61 ± 10)	[Hog68]
3.67	2.85	p+p	$(4.6 \pm 0.7) \cdot 10^{-3}$	(129 ± 25)	[Lou61]
3.701	2.88	p+p	$(4.4 \pm 0.8) \cdot 10^{-3}$	(123 ± 21)	[Hog68]
3.86	3.03	p+p	$(5.7 \pm 1.0) \cdot 10^{-3}$	(160 ± 29)	[Hog68]
4.95	4.10	p+p	$(6.9 \pm 1.0) \cdot 10^{-3}$	(180 ± 30)	[Bie61]

Table 1.5: K^+ production yields in p + p reactions around $2\,$AGeV beam kinetic energy. The values for multiplicity are from [Gaz96]. The total cross section estimates are from the quoted original publications.

Besides multiplicities and rapidity binned transverse momentum spectra, an additional observable is provided by the investigation of kaon flow in experiments comparing longitudinal and radial flows of charged pions and kaons. The flow parameters extracted from experiments deliver additional information on the size of the created fireball, and the results can be explained again by the assumption of repulsive K^+N potential and attractive K^-N potential [Shi98, Uhl05, Fuc06].

The detailed investigation of K^+ production in intermediate energies delivers, therefore, valuable information on the processes occurring in the dense nuclear matter. This knowledge is expected to improve our current description of nuclear matter. It has direct applications, e.g. in cosmology, description star evolution dynamics and, more pragmatically, for understanding the new possibilities for energy sources.

1.3   HADES as a hadron spectrometer

Experimental investigation of strangeness production in nucleus-nucleus collisions was initiated at AGS/Brookhaven and Synchrophasotron/JINR [Har81, Ani82, Sch82, Ani83, Kur88, Abb90b] and continued with a much broader set of nuclei at SIS/Darmstadt at intermediate energies [Mis94, Rit95] and at SPS/CERN [Eva97] up to current experiments at RHIC [Bac02, Ars05, Ada05] with ultra-relativistic energies.

The K^+ production investigation in heavy-ion collisions has a comparatively long history, but most of the previous experiments were restricted to small acceptance measurements [Sch82, Kur88]. Some [Ahl98, Lau00] were performed around the mid-rapidity region and were able to cover a wider acceptance as a set of separated measurements, each dedicated to a small acceptance region. The experiment [Bes97] already covers a wide fixed acceptance region. It measures simultaneously both, positively and negatively charged particles emitted in different polar and azimuthal angles within one measurement setting.

The primary goal of the HADES spectrometer is the measurement of e^+e^- pair production from rare decays of light vector mesons ρ, ω and ϕ. The wide acceptance and good charged particle momentum resolution makes it an attractive tool for hadron physics. The acceptance of HADES is comparable to the one of FOPI [Bes97], but with better access to the K^+ mid-rapidity region. Thus, HADES spectrometer can be a competitive tool with respect to the strangeness production in heavy-ion physics. This is of particular interest for the K^+ production study, which is investigated in this thesis.

As mentioned above, many facts on K^+ production in heavy-ion collisions have been already collected. They can be used for a "calibration/performance" survey of the HADES detector, with respect to the detector alignment, efficiency and the reliability of the analysis software at the beginning of the HADES experimental program. Therefore, it is necessary to perform a high-demanding level of analysis, which would be complementary to the main goal of the experiment with respect to the dielectron spectra from one side, but from another side, would offer the possibility of detailed cross-check comparing to the existing measurements, providing the fact that multiplicities of the triggered e^+e^- yield and the non-triggered K^+ yield are on the same order of magnitude. Thus, the K^+ production investigation is the process which investigation demands comparable efforts to the primary dielectron investigation program of HADES.

The second motivation was an investigation of the feasibility of the HADES spectrometer with respect to the strange physics in parallel to its primary goal. The possibility to extend the measurement [Lau99] of $C + C \rightarrow K^+ + X$ at beam kinetic energy of $E_{beam} = 2\,\mathrm{AGeV}$ outside the midrapidity region allows a more detailed characterization of the fireball in the C+C system.

1.4   Outline of the thesis

This thesis consists of seven chapters, three appendices and a conclusion. In chapter 2 an overview of the detectors installed in the setup of the HADES spectrometer during the experiment in November 2002 is given. The analyzed data sample is taken of the run in November 2002, $^{12}\mathrm{C}(\mathrm{AGeV}) + {}^{12}\mathrm{C}$.

Since one of the motivations of this work was a cross check of the detector performance for rare process the unavoidable part of the data handling, namely the quality control applied to the obtained data, is discussed in chapter 3 and few details are provided in Appendix C.

In the chapter 4, a brief introduction to the tracking part of analysis of the HADES experiment is given. Emphasis is devoted to the Runge-Kutta tracking which plays a key role in this analysis. Implementation details and tests of the Runge-Kutta tracking are provided in Appendix A, for convenience of the reader.

The K^+ identification is discussed in chapter 5, where the corresponding selection cuts are explained, and the background estimate is given within different parts of K^+ meson acceptance.

The efficiency correction scheme is straightforward. It is described in chapter 6, where also the normalization of the total K^+ meson cross section is established relative to the charged pion yields. The influence of the sequence of triggers applied for $e^+\ e^-$ detection is taken into account to provide a minimum bias estimate of the total cross section for the process of $C + C \rightarrow K^+ + X$.

In chapter 7, the double differential spectra of the K^+ production in transversal momentum and rapidity are used to produce one dimensional spectra of differential cross sections in transverse mass with subsequent exponential fits. The slope parameters for different rapidity intervals and the rapidity density distribution are estimated. This measurement extends previous measurement for this system and energy of the KaoS experiment by going outside the midrapidity region.

The work is summarized in chapter 8, while few technical details used in chapter 6 are listed in Appendix B.

2   The HADES spectrometer

The <u>H</u>igh <u>A</u>cceptance <u>Di</u>-<u>E</u>lectron <u>S</u>pectrometer (HADES) was constructed by a collaboration of scientists from 19 institutes of 9 countries in research center GSI[1] [GSI], located near Darmstadt. HADES is a fixed-target experiment, designed to study matter via particle production in collisions by using various beams (pion, proton, heavy-ion). The available ion beam energies provided by the heavy ion accelerator SIS-18 are up to a few GeV per nucleon. The design of the experiment is optimized for studies of vector meson production via the
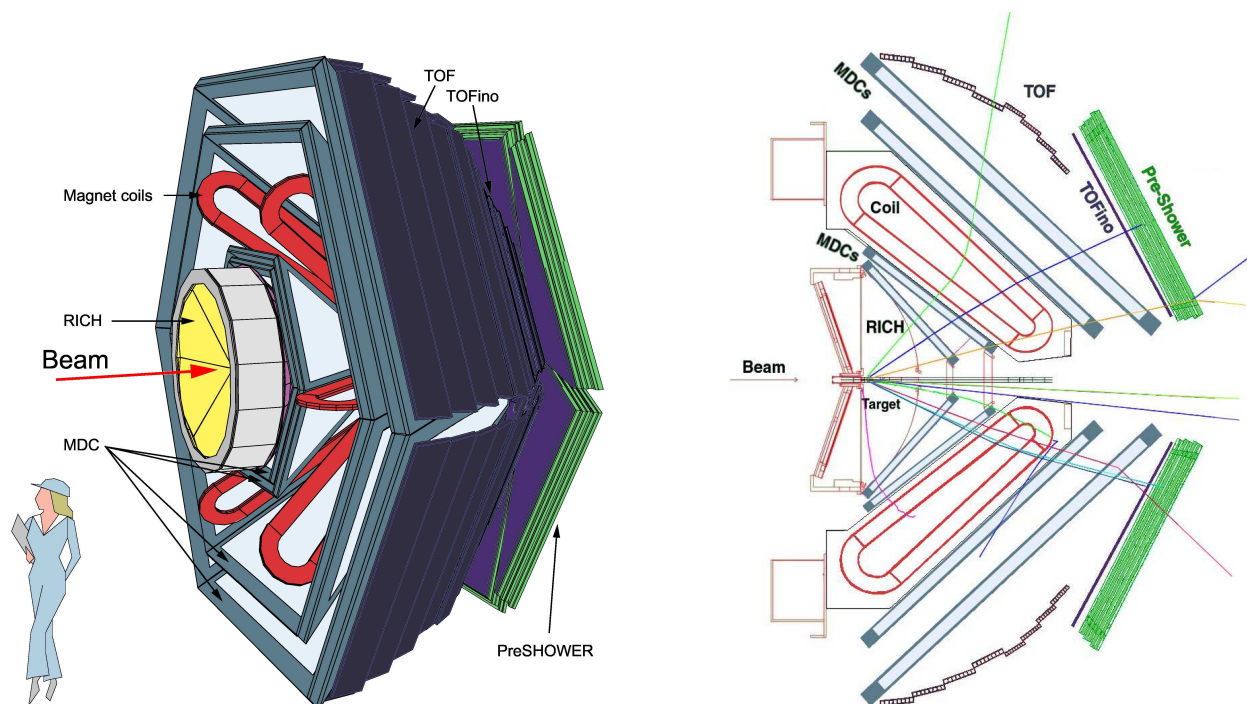
Figure 2.1: Schematic view of the HADES spectrometer. The left panel gives a three dimensional view, while the right one shows a vertical cross section of the spectrometer, where two opposite sectors out of six are displayed. The spectrometer consists of following detectors: Start-Veto counters placed around Target, RICH, four MDCs, a magnet, TOF and TOFINO/Preshower.

di-electron decay channel with high acceptance and with sufficient invariant mass resolution. Therefore, the following characteristics determined the concept of the spectrometer:

---

[1]<u>G</u>esellschaft für <u>S</u>chwer<u>i</u>onenforschung mbH.

- The solid angle coverage in the laboratory system is about 2π, to allow for almost complete reconstruction of events with several decay products in the forward hemisphere.

- Good particle identification for all charged particle tracks inside the acceptance area with special capability of separating electrons and positrons from hadrons.

- High angular and momentum resolution to achieve e^+e^- pair invariant mass resolution of about 1%.

- Capability to work with high loads of secondary tracks for experiments with heavy-ion collisions up to Au(2AGeV)+Au.

- Capability and stability at high event rates up to 10^6 events/second to allow measurements of rare processes during reasonable time.

- Dedicated trigger for e^+e^- pairs: investigation of light vector mesons (ρ, ω meson production at SIS energies is $\approx 10^{-3}$/event) via leptonic decay channel (e^+e^- branching ratio is $\approx 10^{-5}$) needs to overcome these two factors, which are established with a special trigger.

- Minimization of particle production outside of the target area and minimization of material in the acceptance region of the detector in order to reduce secondary particle production with the corresponding reconstruction ambiguities.

From the point of view of technical realization, the HADES detector is divided in six equal sectors covering 60° in azimuthal angle, made nearly rotationally symmetric around the beam pipe, as shown in Fig. 2.1. The spectrometer consists of several dedicated detectors. A Start-Veto detector surrounds the target and provides the common start signal for the electronics. It is fixed in the beam pipe inside the RICH detector. The following detectors are split in six sectors: the RICH detector is meant for electron-positron identification; the four MDC modules (tracking stations) enclosing a superconducting magnet (two modules in front of the magnet and two behind the magnet); the META station: a group of time-of-flight detectors (TOF and TOFINO) with a Preshower detector (installed behind the TOFINO).

The geometrical acceptance of HADES is from 18° to 85° in polar angle and nearly 360° in azimuthal angle. In the beam energy region of 1-2 AGeV, the corresponding geometrical acceptance for e^+e^- pair detection from ω meson decay is about 40% with a mass resolution of 1% estimated with realistic numerical simulation [Sch96]. HADES has also good geometrical acceptance for single hadron tracks ($\approx$ 47% for π^+, $\approx$ 49% for π^-, $\approx$ 30% for K^+), as well as for hadron pairs (about 19% for $\pi^+\pi^-$ pairs from K_s^0 decay [Zum05], about 22% for π^-p pairs from Λ decays [Kan06]), which also makes it an interesting tool for hadron physics.

2.1   The START-VETO detectors

In order to recognize whether an incoming beam particle undergoes an interaction with the target the HADES experiment uses a combination of START and VETO detectors.

Both detectors have identical design of octagonal shape. They are made from polycrystalline diamonds synthesized using Chemical Vapor Deposition technique [Ber99] to meet the requirements of radiation hard and ultra-fast detectors, to be operational with heavy-ion beams of low and intermediate energies up to 2 AGeV with rates up to 10^7 ions/s. The characteristic size of START and VETO detectors in the HADES experiment is 25 mm in the outer dimensions (where only 15 mm matching the beam spot). The thickness of each detector is 100 μm to ensure both low multiple scattering and low production probability of secondaries. When the beam particle crosses the diamond there are electron-hole pairs produced which are then collected on the front/back surfaces covered with thin metal layers at certain potential voltage, connected to amplifier electronics.

The START and the VETO detectors are positioned 75 cm upstream and 75 cm downstream the target, respectively, and work in anti-coincidence, see Fig. 2.2. The reason is that ions which do not interact with the target nuclei are passing both START and VETO detectors and hence deliver signals for a veto of the corresponding events. Ions which interacted with the target are passing the START detector, but not the VETO. If a collision of ions takes place, the VETO detector normally does not deliver a signal. The reason is that the probability to cross the VETO for secondary charged particles formed in the reaction is very small because the VETO detector covers very small solid angle.

By construction, each detector plate is divided in 8 strips of various width. The width of individual strips is optimized such that a coincidence of one START strip with three VETO strips is sufficient for VETO efficiency of 96.5%, as well as achieved count rate per strip is nearly the same. This construction allows one to use START detector as spill monitor and beam focus monitor, connecting a fast counter to each detector strip.

The time resolution of START and VETO detectors for the C(2AGeV)+C HADES experiment is about 30 - 50 ps. This timing is very important, because other timing detectors in the HADES experiment are measuring times relative to the signal provided by the START detector.
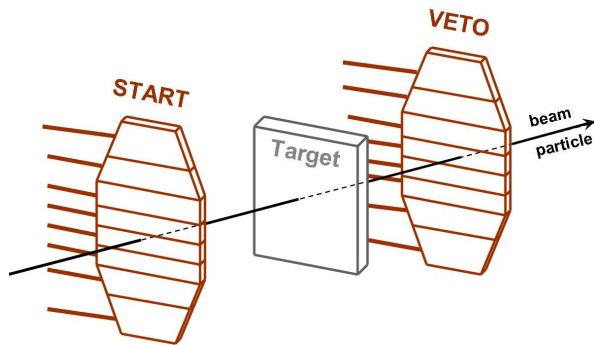
Figure 2.2: A schematic view of START and VETO detectors, which are placed 75 cm upstream and 75 cm downstream the beam line around the target. Both detectors are made identical and consist of eight strips each.

2.2 The Ring Image Cherenkov detector

The Vavilov-Cherenkov effect was discovered in 1934 [Che34]. Cherenkov detectors are used for particle identification basing on the fact that charged particles emit Cherenkov photons when the speed of the particle is larger than the speed of light in the medium. For the past 70 years Cherenkov detectors evolved from differential Cherenkov counters to Cherenkov detectors with full absorption [Bin86]. They are widely used in particle physics
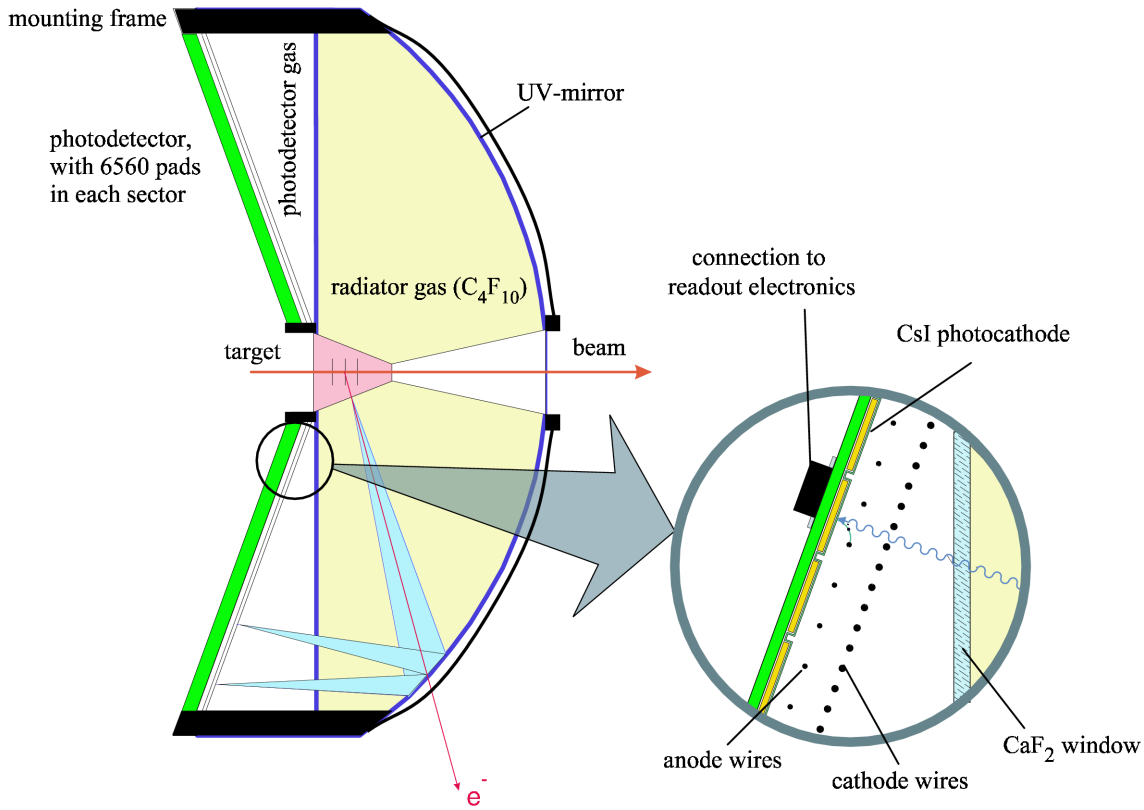
Figure 2.3: Schematic view of RICH detector [Böh99].

and neutrino detection experiments. In order to provide electron-positron selection in a wide angular range of the HADES spectrometer, one requires a Ring Image CHerencov (RICH) detector. In contrast to the old type of differential Cherenkov detectors designed for the case where all particle trajectories are parallel and the spherical mirror projecting the Cherenkov light to the fixed ring of photomultipliers would be sufficient, the technique used in the HADES experiment is much more advanced. In the focal plane of the RICH mirror there are photo detectors which are responsible for the registration of the rings from Cherenkov light with different radii and positions corresponding to particle tracks at different directions. The ring radius is related to the Cherenkov light cone angle θ_c and allows one to measure the speed of the particle $\beta = 1/(n \cos \theta_c)$, where n is a refraction index of the radiator material. The position of the ring center can be calibrated to a measure of the angular coordinates of the particle track.

Additional constraints for RICH design were to fulfill measurement requirements of the HADES experiment. RICH (see Fig. 2.3) is placed next to the target allowing to cover full geometrical acceptance in polar angle range of 18° to 85° while keeping at its minimum the detector transversal size and related assembly costs. This also allows one to place the photo detectors backward to beam direction, i.e. just in front of the target, so that the particles produced at the target do not interact with the material of the photo detectors. The active volume in longitudinal direction of RICH is given by the selected radiator gas to be able to detect Cherenkov rings from electron/positron pairs with sufficient reliability. HADES RICH is operated in the "hadron-blind" regime, to reduce load of the detector and its readout electronics which has to be stable at high interaction rates (10^6 collisions/spill),

material	C_4F_{10}	CFL beam pipe	CFL tank shell
radiation length X_0 [cm]	3200	30	30
$X_0(\theta = 15°)$ [cm]	38.5	0.23	0.04
$\Theta_{ms}(\theta = 15°)$ [mrad]	2.5	1.9	0.74
$X_0(\theta = 85°)$ [cm]	67.6	0.06	0.04
$\Theta_{ms}(\theta = 85°)$ [mrad]	3.4	0.93	0.74

Table 2.1: Radiation length x_0 and multiple scattering Θ_{ms} angle for RICH components calculated in [Kas00] for 500 MeV electrons. "CFL" stands for Carbon Fibre Laminate material used in components of the detector. The radiation length of $X_0 = 28$ cm of the carbon fiber mirror has to be taken into account in addition to the table values.

keeping $e^{\pm}$ signal registered. Therefore, C_4F_{10} gas mixture at normal atmospheric pressure was chosen as the radiator. It produces Cherenkov photons for electrons with momenta $p > 100 \, \text{MeV/c}$ and has low photo conversion as well as high transparency to ultraviolet light which is then registered by the photo detector. To reflect Cherenkov light cone (which has $\theta_c \approx 3.18°$ for particles with speed of light) into ring image on the photo detectors a spherical thin carbon fiber mirror of radius $R = 870 \, \text{mm}$ is used. The mirror is coated by a reflective Al layer (with a thin cover of MgF_2 to prevent Al oxidation). The reflectivity of the mirror is about 85% in the ultraviolet wave length region, while its radiation length is kept small $X_0 \approx 1\%$. The distance from mirror focus and central target point is $d = 0.55R$ (see for details [Sch95, Fab03]). This geometry selection brings polar anisotropy in radiation length and multiple scattering due to material in RICH. In addition, one has to take into account the contribution of the beam pipe material. Radiation length and multiple scattering contribution was calculated for electrons with momentum $p \approx 500 \, \text{MeV/c}$ [Kas00] and summarized in Tab. 2.1. The e^+/e^- detection efficiency of RICH is more effective for high polar angles. One can see that tracks with different polar angles pass different amount of medium and therefore have different multiple scattering.

The cone of Cherenkov photons is reflected into the photo detector, composed of six modules. Each module consists of a multi-wire photo-sensitive proportional chamber with a cathodic pad-plane and has azimuthal coverage of $60°$ (see [Fab03, Fri99] for details). The volume of the photo detector is separated from the radiator volume by a CaF_2 window, and filled with CH_4 gas [Fab03].

2.3   Tracking system

The HADES tracking system consists of four Multiwire Drift Chambers (MDCs) and a superconducting magnet. It covers a range of $18°...85°$ in polar angle. Two chambers, MDC1 and MDC2, are placed before the magnet and two others, MDC3 and MDC4, behind. This allows one to measure the particle direction before and after the track bending inside the magnetic field. The main requirement to the tracking system is to provide an invariant mass resolution of $\Delta m/m \approx 1\%$ for electron/positron pairs in ρ, ω mass region. It is also necessary to minimize multiple scattering and conversion processes in the material of the tracking detectors and to ensure high efficiency of the track detection.

2.3.1   The superconducting magnet

In order to allow for precise momentum measurement of charged particles, a magnetic spectrometer setup is chosen for the HADES experiment. The magnet consists of six superconducting coils surrounding the beam axis (see Fig. 2.4) producing a toroidal magnetic field. The design is optimized to occupy minimal space in the tracking area and to allow the momentum resolution e.g. for electrons and positrons on the level better than 1.5% at beam energies up to 2 AGeV. That means that a strong magnetic field has to be achieved in order to bend tracks of high momentum particles, while keeping the region occupied by the RICH detector free from magnetic field. A compact size of the magnet is needed to reduce costs of outer tracking detectors behind the magnet. These technical requirements to the magnet design of HADES spectrometer as well as the kinematics consideration that higher momentum particle tracks are dominating at smaller polar angles would require a higher magnetic field in this region (compare to larger polar angles) to allow for a good momentum resolution for both fast and slow particles. In this way there is no loss of angular acceptance for slow and for fast particle tracks. A sophisticated design with the help of strongly inhomogeneous magnetic field enabled the realization of these requirements for the HADES magnet; a detailed description can be found in [Bre99].

Figure 2.4: The superconducting magnet of HADES during its installation phase. The coils of the magnet are mounted on two support circles leaving space for RICH detector and free path for the beam axis in its center of symmetry as well as for tracks of particles produced in case of interaction. No detectors were installed at the time when the photograph was taken.

The magnet is equipped with a cooling system based on liquid helium. The maximal operational current is 3665 A at a temperature of 4.6 K. This corresponds to a maximum magnetic field 3.7 T around the coils and of about 0.8 T in the regions between coils. During the C(2AGeV)+C experiments the magnet was operated with a lower value magnetic field (the current inside coils was 2497 A) to avoid significant magnetic fields in the regions around MDC2 and MDC3 which would cause loops of low-momentum particles inside the tracking detector regions.

2.3.2   Multiwire Drift Chambers

The HADES tracking system is needed to reconstruct the momentum of the charged particles produced in the collision from their track direction change within a magnetic field. It is primarily focused on detection of tracks originating from a region around the target area.

Other interactions which may take place outside the target area, as well as some unstable particles which decay far behind the target area, are not among the main interests of the experiment. Therefore, only four planes with one Multiwire Drift Chamber (MDC) module in each plane per sector are sufficient. All sectors have the same construction design. Each of them covers 60° in azimuthal angle and a region from $\approx 18°$ to $\approx 86°$ in azimuthal angle. Two inner MDCs (MDC1 and MDC2) are installed in front of the magnet and two outer MDCs (MDC3 and MDC4) behind the magnet. Therefore, the HADES MDC detectors are used in six sectors, with four MDC modules in each, totally 24 MDC modules. Each MDC detector provides a high resolution coordinate measurement for the track position.

Every MDC module is manufactured as a set of 13 layers of wires fixed on a trapezoidal shape Stesalit© frame. The frames carrying wire layers are hold together by stiffeners made of stainless steel compensating the wire tension forces. The active gas volume of the module is separated from outside with a thin Mylar foil of thickness $12\,\mu m$ (Fig. 2.6). The wires in each layer have the same direction within the layer. Since the multiplicity of tracks produced in heavy ion reactions can be as large as 200 charged particles in the HADES acceptance for reactions Au(2AGeV)+Au [Gar98], it may cause an ambiguity arising in wire based detectors while measuring high loads of tracks, thus an over-determination of a hit position obtained from track passing the MDC is needed. Therefore, six layers of sense wires oriented in five different directions are implemented in each MDC detector, see Fig. 2.5. The directions of layers with sense wires are { $+40°$, $-20°$, $+0°$, $-0°$, $+20°$, $-40°$ }.
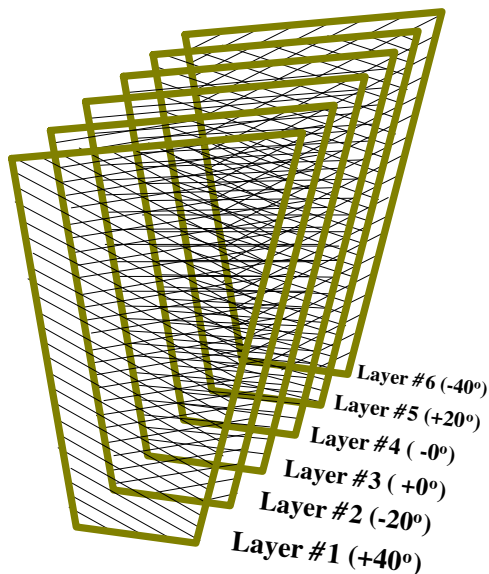
Figure 2.5: A schematic illustration of orientation of six layers of sense wires fixed in Stesalit© frames inside MDC. This construction allows to exploit the tracking detector in case of high multiplicity of tracks per event.

The remaining seven layers are cathode layers have the same orientation of 90° and supplied with high voltage. They provide electrostatic separation between different layers of sense wires. Each layer with sense wires contains two kinds of wires the sense wires themself which are anode wires and an equal number of so called field wires, needed to separate different sense wires of the same layer from each other electrostatically (which is illustrated on the right part of the Fig. 2.6). During the operation, the cathode and field wires are connected to high voltage, of a negative potential about -1700 V ... -2400 V. The applied value of high voltage differs depending on the cell size of the module. Sense wires carry the ground potential. They are connected to read-out channels of electronics, which is a chain

of amplifier, signal discriminator and digitizer with data storage buffer. There are 1100 read-out channels per module independent of its size. The dimensions of modules, cell sizes, radiation thickness and nominal potential settings are summarized in Tab. 2.2. An average experimental[2] spatial drift cell resolution is below $140\,\mu m$ for all modules [Mün]. The mean coordinate resolution achieved by MDC module depends on several factors, like efficiency of the layers and calibration quality of TDCs, which is studied using numerical simulations in [Mar05], see Tab. 2.3.
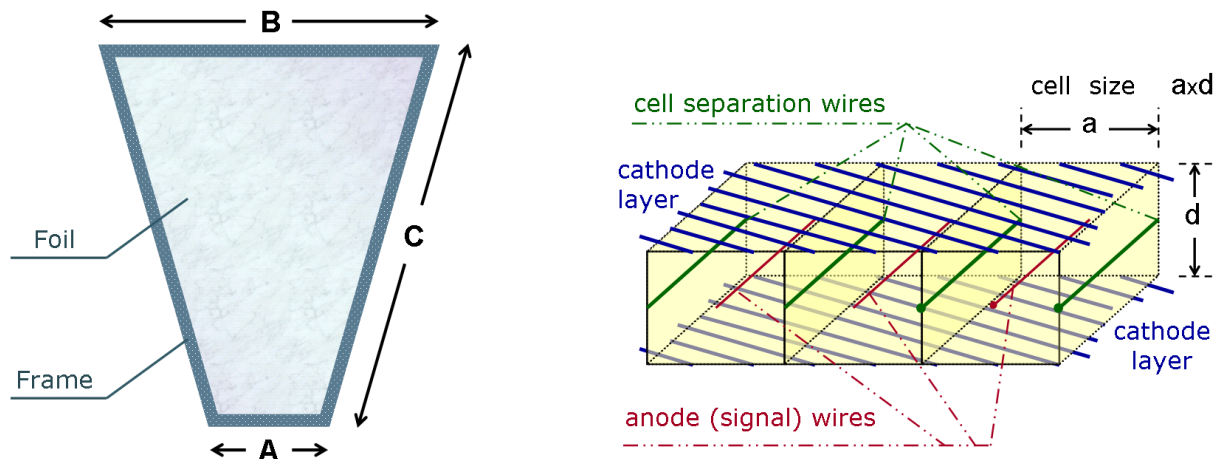
Figure 2.6: Left panel: front view and the definition of dimensions for MDC module. Right panel: illustration on drift cells formed by different wire layers; three neighboring cells are shown, while different wires are depicted with color lines; also the definition of the cell size is given.

Module	MDC1	MDC2	MDC3	MDC4
Cell size a×d [mm^2]	5×5	6×5	12×8	14×10
Dimension A [mm]	139.21	205.00	310.43	345.46
Dimension B [mm]	767.38	905.00	1804.80	2224.05
Dimension C [mm]	839.19	1049.27	2139.05	2689.04
Surface [m^2]	0.34	0.49	1.88	2.83
Volume [l]	11.99	20.58	150.4	197.8
Cathode wire diameter [μm]	80	80	80	100
Potential wire diameter [μm]	80	80	100	100
Signal wire diameter [μm]	20	20	20	30
Radiation thickness (X/X_0)	$0.56 \cdot 10^{-3}$	$0.53 \cdot 10^{-3}$	$0.48 \cdot 10^{-3}$	$0.48 \cdot 10^{-3}$
Field wires potential [V]	1750	1800	2000	2350

Table 2.2: MDC modules design summary [Str98, Mar05]. The quantities a, d, A, B and C are defined in Fig. 2.6.

The radiation length of tracking detectors is also reduced to minimum to reduce the amount of material along particle track. The drift chambers are constructed from thin

---

[2]The test was performed during the experiment of C(2AGeV)+C with $2.1\,\mathrm{GeV/c}$ momentum protons.

Module	TDC calibration error	σ_x [μm]	σ_y [μm]
MDC1	2%	95.2	48.4
	10%	108.3	55.2
MDC2	2%	99.0	45.3
	10%	111.0	53.7
MDC3	2%	127.9	53.4
	10%	186.5	88.0
MDC4	2%	133.3	61.8
	10%	211.9	106.8

Table 2.3: The coordinate resolution of different MDC modules depending on possible error of TDCs calibration, studied with simulations in [Mar05]. The difference in x and y coordinate resolution is caused by the design orientation of layers in the MDCs.

wires. The cathode and field wires are made of aluminium, while sense wires are made from tungsten coated by gold, see Tab. 2.2. The gas used for drift chambers operation is a mixture of He-Isobutane in proportion of 60/40 at normal pressure.

When a charged particle crosses the gas mixture inside the MDC detector it undergoes several interactions with molecules of gas on its way. This causes excitations and ionizations of atoms of the molecules, with subsequent deliberation of electron-ion pairs which are moving inside the electrostatic field of MDC formed by cathode, field and anode wires. The unbounded electrons move towards the anode of the nearest cell, accelerated by the field. On their way they also undergo several interactions with the gas causing additional ionization of the medium. The process keeps going till the moment when the electrons reach the anode. The corresponding ions move much slower, without noticeable secondary ionization of medium and reach cathode much later. Each anode (signal) wire is connected to a channel of front-end electronics with preamplifier followed by a shaper (constant fraction discriminator), realized in a 16 channel-daugterboard with four ASD-8 chips. These daugterboards inserted in motherboards contain either 4 or 6 such chips, i.e. processing 64 or 96 channels. Motherboards are mounted directly on the frame of the MDC module to be close to wires. On one side this allows to minimize signal losses but on another side, if a serious problem with ASD-8 chips occurs, there is practically no possibility to exchange it during the experimental run. Any damaged daughterboard stays there, disabling some part of geometrical acceptance. One reason leading to failures of ASD-8 chips is the temperature sensitivity of motherboards. Therefore, a special control system was developed to monitor temperatures and cool the front-end electronics. This allows to keep the number of damaged ASD-8 chips low. During November 2002 HADES beam time the problem was not yet explored which has lowered the efficiency and spatial resolution of tracking detectors in some areas of acceptance. More details on HADES MDC electronics and tools to control the MDC stability/quality are described in [Wüs05].

For every wire hit in the MDC the information from front-end electronics is digitized using Time-to-Digital Converters (TDC) and is delivered into storage buffer. On trigger request all relevant information is transported to the Data Acquisition System (DAQ). When the electron cloud causing the signal on the anode wire arrives, the TDC delivers

its first measurement called t_1. At the moment when nearly all electrons released by the passed particle are collected, the second time measurement t_2 is provided by the TDC. The t_1 information can be converted into a distance between the wire and the track causing the signal on that wire. In practice, all the timing information in experiment is counted relative to the signal from the START detector, hence one needs to take into account a certain time delay caused by the fact that each MDC is located at a certain distance from START as well as that there is an additional delay of the signal inside the MDC due to finite propagation velocity of the electric signal along the wire. In addition, the t_1 and t_2 signals depend on the threshold setting of the corresponding constant fraction discriminator. Therefore, each TDC channel has to be properly calibrated. The calibration process is described in detail in [Mar05]. The t_2 signal is important to discriminate true signals from signals caused by electric noises induced by currents in surrounding channels of electronics (so called cross currents). The difference between t_1 and t_2 measurements has different signatures for the real and the electrically induced signals, which is used in off-line analysis to reject noise contribution in MDCs before execution of tracking algorithms.

2.4   META detectors

The Multiplicity/Electron Trigger Array (META) is a set of detectors needed for additional selection of trigger conditions. It is located behind the fourth plane of tracking detectors. A trigger on charged particle multiplicity larger than some threshold number is directly connected to the centrality selection of the triggered events. Two plastic scintillator detectors, namely TOF and TOFINO, are used "on-line" to determine the multiplicity of the event to be used within trigger conditions if an enhancement of central events is needed. In addition to the on-line work, during the off-line analysis the time of flight information in combination with momentum determination by the MDC detectors is used for the identification of charged particles heavier than electrons.

Electrons themselves, due to their small mass, have velocities close to the speed of light, and therefore can not be easily distinguished from muons and pions of high momenta. This suggests the usage of another detector, the Preshower, in addition to RICH. Since, at energies of the SIS accelerator, hadrons emitted at polar angles larger than 45° are not any longer fast ones, one needs the Preshower detector only in the inner part of the acceptance, namely for polar angles of 18° till 45°, where the separation between electrons and light hadrons based on velocity and momentum might be insufficient.

Finally, META consists of 3 different detectors, with some internal granularity each. This allows one to use these detectors as a supplementary coordinate measurement system, which is important to enable matching between tracks reconstructed with help of magnet/MDC and hits in META detector delivering also the time-of-flight information. All detectors are arranged in six sectors, defined by the six coils of the superconducting magnet.

2.4.1   Time-Of-Flight detector

The Time-Of-Flight (TOF) detector [Ago02] contributes to both the multiplicity trigger and to the information used for particle identification, providing the time interval between the signal from Start detector and the signal from TOF. Identical TOF detectors are installed in all six sectors of HADES, see Fig. 2.7. Each TOF sector consists of a set of 8 blocks with

8 scintillator bars per block. It covers nearly 60° in azimuthal angle and from 44° to 88° in polar angle. The scintillator bars of the inner 4 blocks have cross section of $2 \times 2\,\mathrm{cm}^2$, while
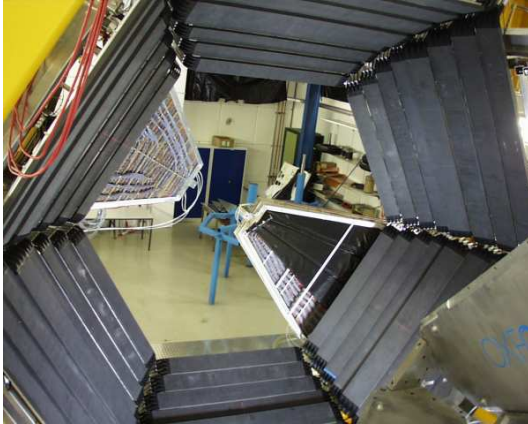
Figure 2.7: A photo of the TOF detectors. The view is from the target area. All six sectors are mounted. In the right bottom corner a part of the magnet is visible. Two sectors of Preshower detector are installed in the center. The right bottom Preshower sector is partially covered be the TOFINO detector (only 3 blocks out of 4 were installed at the time when the photo was made).

that of the outer blocks is $3 \times 3\,\mathrm{cm}^2$. The length of the scintillator bars ranges from $1475\,\mathrm{mm}$ to $2365\,\mathrm{mm}$, depending on polar angle position. An estimate [Sch95] of the probability to have two particles hitting the same scintillator bar is less than 20% for central collision of Au(2AGeV)+Au.

An estimate [Ago02] of the overall registration efficiency of the TOF detectors is about $(96.0\pm0.2)\%$ for all charged particles measured in a C(1AGeV)+C experiment, and the time resolution is better than or about $150\,\mathrm{ps}$. Due to its granularity, TOF allows to measure the y coordinate (in the module reference system) but also the x coordinate due to the design of the signal readout. A particle crossing the TOF bar produces the fluorescence in scintillator. The light is traveling along the scintillator in two directions. There are two photomultipliers registering the light signal amplitude and its time of arrival, one from left and another from right side of the bar. One can show [Ago02] that

$$x = \frac{x_r - x_l}{2} = \frac{t_r - t_l}{2} v_{gr}, \qquad (2.1)$$

where t_r and x_r are the time and distance to the signal origin and the right photomultiplier respectively, while t_l and x_l are the same variables for the left photomultiplier; $v_{gr} \approx 16\,\mathrm{cm/ns}$ is the group velocity of light in TOF bar material. The x coordinate resolution is better than or about $2.5\,\mathrm{cm}$.

The amount of light is proportional to the energy loss of a charged particle traversing the scintillator strip. It is also measured with photomultipliers and digitized with an ADC. The corresponding energy resolution measured with slow protons is $\Delta E/E \approx 10\%$. Naturally, these characteristics allow the TOF detector to play an important role in the HADES experiments, allowing to measure not only the time of flight but also the particle coordinate and energy loss information.

2.4.2   TOFINO detector

An analog of Time-Of-Flight detector, TOFINO, is installed in the region of lower polar angles from 18° to 45°. Each TOFINO sector consists of 4 individual plastic scintillator paddles, shown in Fig. 2.8, which are read out with photomultipliers from one side. The

time resolution is about 450 ps. The energy loss of a particle is measured as in case of TOF and the resolution is $\Delta E/E \approx 10\%$ [Gol05, Gol02]. The coordinate resolution for particle tracks in this polar angle region is provided by the Preshower detector installed right behind the TOFINO.
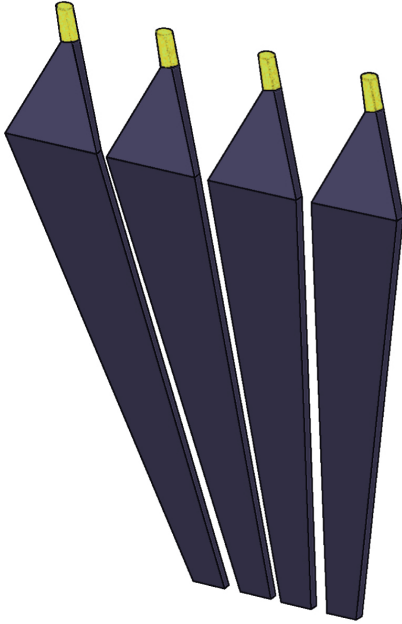
Figure 2.8: A schematic view of one TOFINO sector, which consists of four scintillator paddles covered by non-transparent shield and is connected via a light guide to a photomultiplier (not shown). The position of TOFINO in the HADES setup is shown in Fig. 2.7.

Having poor granularity in the region of high density of tracks, the probability to have two or more particles crossing the same TOFINO bar is about 20% already for C(2AGeV)+C reactions which has to be taken into account during analysis. To work with heavier systems, another detector with a higher granularity and better time resolution is foreseen to substitute the TOFINO in future, namely Resistive Plate Chambers (RPC) [Fon01, Gar05].

2.4.3   Preshower detector

The Preshower detector [Bal04] is installed in addition to TOFINO detector to identify electrons produced in pion, proton and heavy ion-induced reactions in the momentum range $0.2\,\mathrm{GeV/c} < p < 1.5\,\mathrm{GeV/c}$. The Preshower is needed for better electron identification in the region of low polar angles when the time-of-flight resolution becomes poor as compared to the time of flight itself and therefore insufficient for the discrimination of fast pions against electrons. The identification of electrons is based on the shower appearing in a converter material (made of lead) due to the effect of bremsstrahlung [Leo87]. The geometrical acceptance of each sector of Preshower detector covers nearly $60°$ in azimuthal angle and $18° < \theta < 45°$ in polar angle. Each sector of the Preshower is composed of a stack of three trapezoidal wire chambers (pre-chamber, post1-chamber, post2-chamber), separated by two lead converter plates as shown in Fig. 2.9. The converter material is made from lead with thickness of 1 cm, which corresponds to about 2 radiation length. Each chamber is filled with a mixture of Ar, Isobutane and Heptane gases in proportion of 33:65:2. The gas mixture is enclosed from outside by two planes, the steel plane and the read-out plane (which keeps also the cathode plates). The layer of wires in the middle plane of each chamber consists of
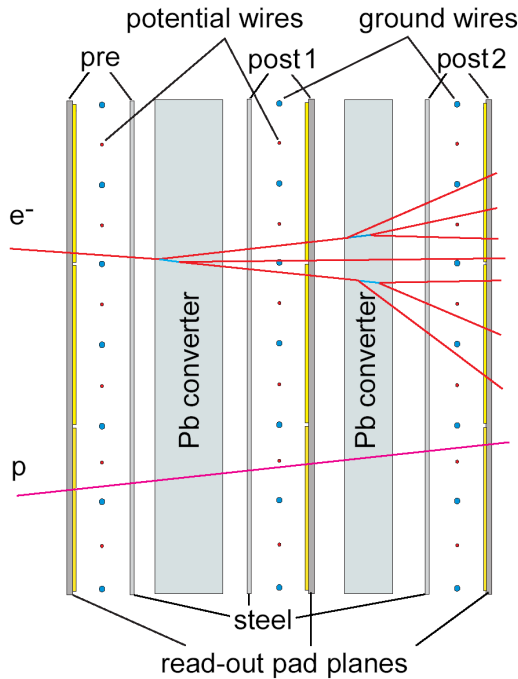
Figure 2.9: A schematic view of the Preshower detector which consists of three wire chambers separated by two layers of converter material [Bal04]. The cathode plates (at the read-out panes) are indicated by yellow color.

two wires under two different potentials forming corresponding anode and cathode at every second wire. A charged particle passing through the gas chambers produces an ionization avalanche with electrons drifting towards the closest anode wire. Moving electrons induce a positive charge on the nearby cathode pads connected to charge-sensitive preamplifiers. The integrated charge around the spot, where the particle crosses the chamber, is proportional to the avalanche charge. The chambers operate in a Self-Quenching Streamer mode [Ale80], [Ata82] such that the collected charge is independent of the deposited energy but depends only on the number of particles crossing the chamber.

The granularity of the pad is optimized [Bal04] such that the double-track probability in a single pad is less than 5 % for Au(1GeV)+Au collisions. There are 32 pads in Y direction and from 20 to 32 pads in X direction (larger number for higher polar angles). The corresponding pad dimension varies from $22 \times 30 \, \text{mm}^2$ till $57 \times 45 \, \text{mm}^2$ (X×Y). This variable pad size roughly ensures equal occupancy of the corresponding electronic channels. The efficiency of electron/positron identification with the Preshower detector is about 80%, while the efficiency of the fake-electron registration is estimated to be about 10% for $p = 850 \, \text{MeV/c}$. Including the cut on time-of-flight, $t_{TOF} < 8.7 \, \text{ns}$, from TOFINO detector one may suppress about 90% of hadrons. Finally, the Preshower detector together with TOFINO provides good selection capability for electrons as well as it allows to estimate the track coordinate at the inner part of the META detector, which is useful for the matching with corresponding information from MDC detectors.

2.5   Trigger system

The HADES spectrometer was constructed to operate with ion beams from the SIS-18 accelerator complex [GSI]. SIS-18 can deliver ion beams for various stable nuclei from hydrogen till uranium. The energy range varies approximately from 1 to 4.5 GeV per

nucleon depending on ion charge-to-mass ratio. The maximum beam intensity at the exit of SIS-18 reaches up to 10^{10} ions per second for light nuclei and up to 10^9 for heavy ones like gold and uranium [Ste92]. However, on average, the beam intensities used during long term operations are normally lower, about $10^7, ..., 10^8$ ions per spill.

The target thickness is taken less than 1% of interaction length to minimize event pile-up, photoproduction of electron-positron pairs and multiple scattering. The maximum event rates are in the order of 10^6 Hz. The fraction of light vector mesons decaying into e^+e^- pairs is in the order of $10^{-5}...10^{-6}$, i.e. very much suppressed. Therefore, to achieve its primary purpose, a considerable number of e^+e^- pairs from the decay of light vector mesons has to be collected by HADES. The corresponding raw data rate of several kB/event would be equivalent to a data stream of some few GB/second, which requires data storage capacity of more than 10^6 GB for two weeks of experiment. A compromise, taking into account present status of data storage technique, is required: a set of dedicated trigger conditions is used to preselect only a small fraction of all events, relevant for the analysis. The schematic view of the Trigger system used in HADES experiment is presented in Fig. 2.10.
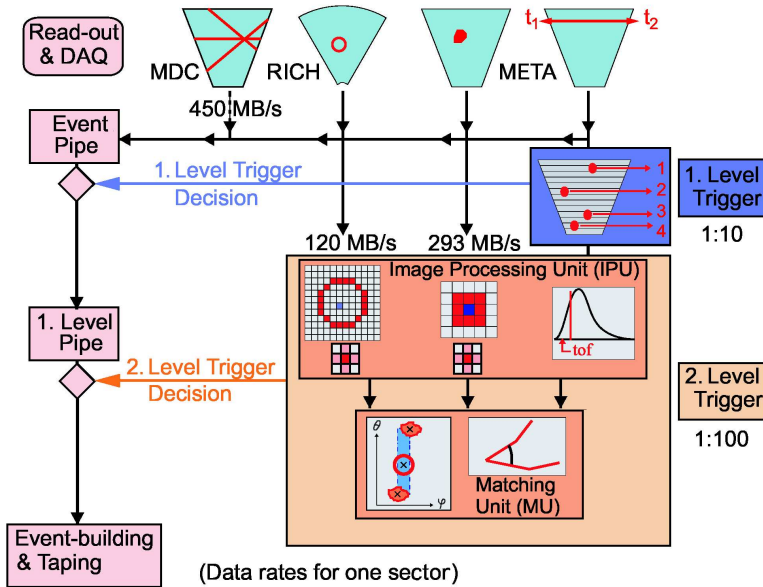
Figure 2.10: A schematic chart of HADES Trigger functionality. The diagram follows the order of the Trigger functionality.

Presently, the Trigger system of HADES consists of two levels [Toi04]. The first-level (LVL1) trigger selects only events with charged particle multiplicities higher than a certain value. This is done to preselect central heavy-ion collisions, where higher densities and temperatures of nuclear matter are achieved compared to peripheral ones. The concept of multiplicity trigger takes advantage of the relation between the centrality of heavy-ion collisions and the number of participants in the overlap region as resulting from simple geometrical models. Signals from TOF and TOFINO detectors are collected by the multiplicity trigger unit which is responsible for the LVL1 trigger decision. The decision is taken during a time interval of 100 - 200 ns. A reduction factor of 10 can be achieved with the help of centrality trigger in Au+Au collisions of 1 - 2 AGeV. For light nuclei the relation between reaction multiplicity and centrality is not so direct. According to the Ultrarelativistic Quantum Molecular Dynamics (UrQMD)[3] simulations for C(2AGeV)+C reactions,

---

[3]UrQMD is an event generator for simulation of particle production in heavy-ion collisions at high

the multiplicity trigger requiring more than four charged particles in HADES acceptance would keep about 1/3 of the original events.

The second level (LVL2) trigger enriches the events with signatures of e^+e^- pairs from decays of light vector mesons. It combines information from RICH, TOF and TOFINO (with Preshower) to make the decision.

- The RICH Image Processing Unit performs an on-line search and recognition of rings from the e^+e^- signals in the pad plane of RICH detector [Leh99, Leh00, Leh03]. The total delay of the trigger decision due to the ring recognition itself as well as the formatting and the transfer time to the Multiplicity Trigger Unit is about $30 - 40\,\mu$s, depending on the event size.

- The TOF Image Processing Unit [Lin01] searches for e^+ or e^- candidates among the charged particles reaching the TOF detector. The analysis of TOF signals consists of time-of-flight computation from two measured TDC channels for each TOF strip with subsequent conversion to a coordinate along the strip and computation of polar and azimuthal angles. The computations are performed only for small times, comparable with the time of flight taken by electrons to reach the TOF detector. Due to the small amount of data and the necessity of floating point computations, the readout and the algorithm is realized in a dedicated board with Digital Signal Processors using pipelined architecture.

- The Shower Image Processing Unit searches for e^+ or e^- candidates in the Preshower detector. Electrons or positrons form showers in the detector which can be characterized by a growing multiplicity of the shower formation process across the three proportional chambers (Pre, Post1 and Post2), see Fig. 2.9. A pattern recognition algorithm is realized similar to RICH IPU [Pet00].

The final LVL2 trigger decision is taken by the Matching Unit which establishes a matching between the combinations of ring images in RICH with coordinates estimated by META. The Matching Unit works independently in each sector of the detector. Matching is established on the basis of an azimuthal angle correlation. This requirement reduces the number of events by a factor 10 [Toi04]. Additionally, but not activated in previously performed experiments, for all matched RICH-META combinations it can provide a momentum estimate, based on Kickplane Tracking approach [Gar03]. A short description can be found in section 4.1. There, the target position and one coordinate from RICH IPU before the magnetic field are used, one more coordinate is provided by the IPU of META (TOF and Preshower) detectors. This approach is proven to provide a reliable estimate of the $e^\pm$ momentum in the range of $50\,\text{MeV/c} < p < 1000\,\text{MeV/c}$. The polarity of the lepton candidate is estimated from the deflection in the magnetic field. Therefore, lepton pairs as $e^+\,e^-$ combinations can be constructed and respective invariant mass estimates can be provided already on-line. The LVL2 trigger decision can be produced depending on opening angle and on invariant mass estimate of the $e^+\,e^-$ pair candidate. In case of demanding a $e^+\,e^-$ opening angle of $\alpha_{e^+e^-} > 20°$, the final reduction of 1/100 due to LVL2 trigger would be achieved.

---

energies based on transport model approach [Bas98].

3 HADES Quality Assessment

"Проблемы есть, проблемы будут
и никогда Вас не забудут..."
Неизвестный автор

3.1 Introduction

Hundreds of millions events per beam time of typically one week duration are recorded in several experiments performed with the HADES detector. This amount of data is stored at the GSI tape robot. For example, in November 2001 during the HADES beam time the amount of stored data was about 490 Gb. Already in November 2002 (both test and production) beam time about 1190 Gb (220 millions triggered events) of raw data were recorded.

To obtain physical results one needs to create Data Summary Tapes (DST) which store not the raw, but already partially analyzed data. They represent the first analysis step which requires calibration of detectors and their relative alignment. In order to achieve this step one needs to decide which raw files contain information of satisfactory quality for the calibration of the respective detectors. To accomplish this, it is necessary to use a Quality Assessment (QA) framework which is a set of methods to evaluate and establish the quality control of the data. HADES QA is split into two parts. First, a so called online QA may run in parallel to the data production, i.e. during the experiment. It can be used by the shift crew as a compressed source of warning information if some detectors do not work properly. Despite of being a very useful source of information, it can not detect all possible problems during the experimental run. That is why an offline QA was developed as well. Offline QA is used for two main reasons. One is to help in preselecting of good raw date files, the so called HLD (HADES List-mode Data) files for the calibration of respective detectors. Another reason is to assist in qualifying data for DST production. In HADES experiments these two offline-QA branches are called Low Level QA and DST QA, respectively.

3.2 Low Level QA for MDC

Low Level Quality Assessment was developed in particular to perform a preselection of HLD files for TDC slope and offset calibration of the MDC detectors. It has access to each event stored in HLD file to guarantee that all events can be investigated, so that if a problem occurs it will show up in the resulting diagnostic plots. The access to the data is possible

Figure 3.1: An example of MDC Low Level QA plot used for the preselection of stable intervals for calibration of MDC3 detectors (example from November 2001 beam time). The distribution of mean values of t_1 is shown as a function of file number. Different colors correspond to different sectors. In this experiment, only 4 out of 6 MDC detectors were installed in plane 3 of the HADES setup. The file name is indicated as vertical text field (hardly readable in this figure size) for each of the file numbers. This allows the user to have all information available at once.

before and after time cuts which allows to check how well the time cuts were selected, and if they were stable during the time of date accumulation for this file.

Low Level QA monitors the stability of t_1 (time of the appearance of the first electron from the particle track in MDC, see section 2.3.2) and t_2 (time of the last electron from electron cloud in a drift cell caused by the track) information respectively, with time cuts applied or not. It also monitors the electronic noise when only one, two or three wires per event fire in a single MDC, which indicate simply the case of no real track in the chamber (but only the induced noise is present). Another noise factor can be monitored through the multiplicity of cells fired. The multiplicity of neighboring cells inside one layer supply information about the level of noise induced by cross currents in electronics. All these values are presented as a trend plot averaged over a certain number of events (typically 5000 events per step). Thus, one monitors the stability of MDC operation within one data file. The plot for the mean value of t_1 with or without time cuts helps monitoring of the High Voltage (HV) settings indirectly. This is important because the stability of the TDC offset calibration is very sensitive to the HV value of the MDCs.

Another point is to monitor the stability of these values from one HLD file to another. For that reason one needs only to take the mean value of a considered variable (e.g. t_1, t_2, noise levels etc.) averaged over the whole file and plot this quantity for each file involved as a trend plot versus file number. As an example of such Low Level QA plot, the distribution of mean values of t_1 for MDC3 drift chamber is presented in Fig. 3.1. This part of "summary" plots of Low Level QA was normally used to make a decision for preselecting stable condition regions for TDC offset calibration of MDC. As one sees, this approach immediately gives an impression about files with unstable conditions which are to be excluded from the list of good/stable files for calibration. If one has doubts while deciding concerning the quality of some particular file it is always possible to inspect complementary trend plots of the files as mentioned above. The feature of serious problems is that they are normally reveal in several trend plots simultaneously. Observed problems are eliminated by excluding the corresponding files from further consideration.

3.3   HADES Quality Assessment of DST production

The purpose of HADES Data Summary Tape Quality Assessment (DST QA) is to provide diagnostic information (histograms and scalers) during Data Summary Tape (DST) production in order to assess the data quality for higher levels of physics analysis. Initially, the program was modeled after the STAR QA/QC (quality assurance/quality control) package [Ray03].

QA works in parallel to DST production; it creates one output per DST file. The output is stored in several formats, as PS or PDF format, as well as ROOT-file format [Bru05] in order to allow for convenient access to the user or with dedicated ROOT scripts.

One of the features of DST QA is that all diagnostics is done for the same conditions of analysis of HLD data to prepare DST data level. That means all calibrations and cuts (for example, time cuts for MDCs) are included. In most cases one can not create and compare diagnostics with and without cuts applied. Thus, we need to keep Low Level QA for testing conditions without cuts applied. What one can see in DST QA is, how stable the result is with respect to the cuts applied during the experiment. This may be used for diagnostics of the detector performance.

Presently, the program includes 92 diagnostic plots, several of these are overlays of six different sectors represented in different colors (see, e.g., Fig. 3.2).

Each physical detector of the HADES setup as well as two logical units, Kickplane and Trigger, are covered. The design of program is open for additional diagnostic plots. In order to illustrate the typical amount of diagnostic information created for each analyzed data file, some numbers are provided here. For DST generation 4 of November 2001 beam time 116 histograms and trend plots for each of 232 files were produced. For November 2002 beam time already 249 histograms and scalers were created in each diagnostic file (i.e. for about 360 files from preparation part plus 320 files from production part of the beam time).

3.4   Principles of diagnostics

Presently, DST QA includes following sections: Start, RICH, MDC, TOF, TOFINO, SHOWER, KICKPLANE, TRIGGER detectors and corresponding variation histograms and scalers as a conclusion. For each item we can have a pattern plot or a digit which has to be assigned/selected by experts. Normally, the user has to look and compare the actual file plot with diagnostic one. Up to a certain level this procedure can be done automatically with a special program, see for example next subsection.

By type of diagnostic plot we can have 1-dim., 2-dim. and trend plot histograms. To compare 1-dim. and 2-dim. histograms with corresponding pattern either Kolmogorov or χ^2 test may be used [Ead71]. To compare 1-dim. histograms for a certain group of plots the method of central moments [Ead71] can be used. It is simple but useful method is explained later. These two methods are sufficient to satisfy the requirements of DST QA analysis at the moment.

3.4.1   General tool for post-analysis of QA-output

In order to be able to analyze or even simply to look over thousands of DST-QA output histograms during reasonably limited time one needs a special software. To fulfill this
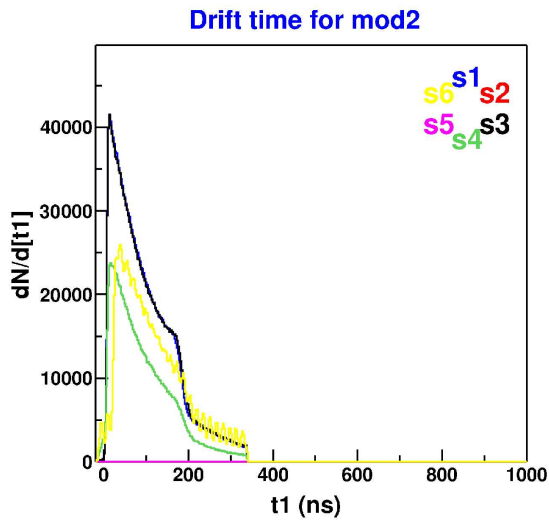
Figure 3.2: Examples of DST QA plots produced for each file of DST production. On the upper left panel a picture representing t_1 distributions for MDC3 detector is shown for one of the files from November 2002 beam time. The picture is extracted from MDC page of the DST QA report. On the right panel a whole page from the DST QA report is shown representing tracking QA: mass distributions for tracks in TOF and TOFINO parts of the detector reconstructed by three different tracking methods are shown. Different colors correspond to different sectors of the spectrometer.
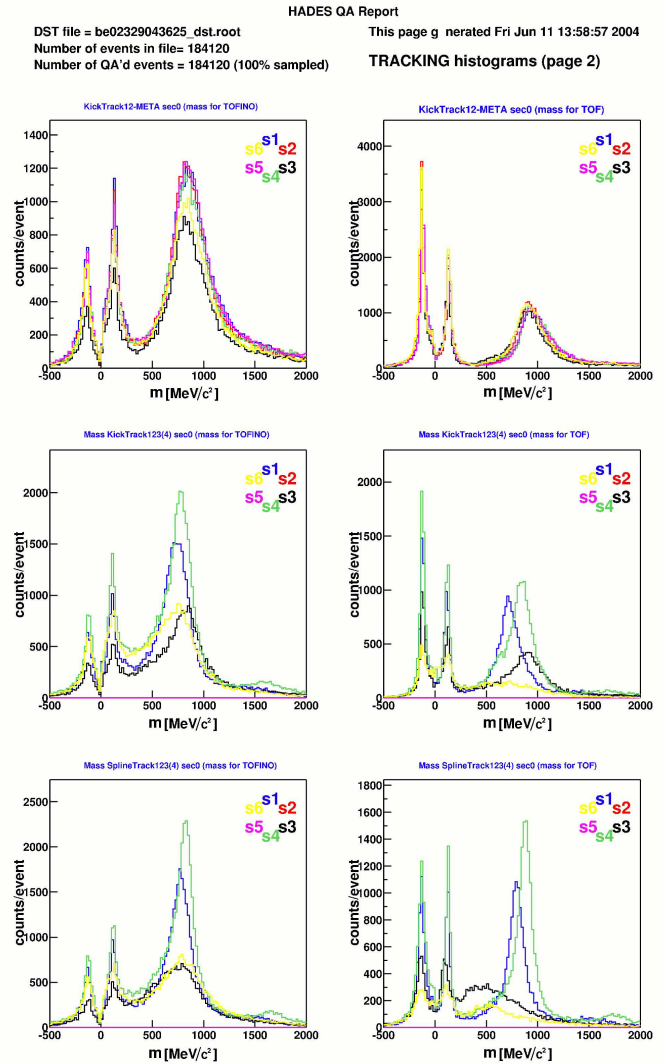
requirement a dedicated Graphical User Interface (GUI) oriented program was written under pure ROOT GUI classes [Bru05]. It includes several methods integrated into one common interface and allows the user to perform an observation how a certain QA histogram develops in time during the experiment.

The basic principle is taken from the early era of high energy physics, when experimentalists were looking through hundreds of bubble chamber films trying to find characteristic signatures of a particular decay process. Nowadays, the situation is somewhat similar, except the fact that we do not monitor our tracks by bare eye, but we still watch how our detectors work in the course of time. The time interval (observation quant) depends normally on the amount of data collected and written under the same conditions, or simply a time interval during which it is safe to assume that conditions were unchanged. In the HADES experiment, this quantity of time during which the conditions were assumed to be the same is practically limited by the time of collecting/writing the data into one HLD file. According to the rules of the shift crew, in case some conditions were changed the DAQ operator has to stop writing into the current file and to start a new one if necessary.

This allows simple realization of the post-analysis QA monitoring. The quality control histograms are created for each data file, and their dependence on time (file number) is monitored as a course of file number. Making this work easy for the user turned out to be a crucial point of QA analysis after HADES started to deliver hundreds of data files. Using computing power of a modern PC equipped with the ROOT software within several minutes it is possible to make an analysis of the quality of one histogram filled during entire beam time. The functionality of the tool for post-analysis of DST QA-output is given in Appendix C. One illustration of the method applicability is given in Fig 3.3, where the reconstructed proton mass is monitored as a course of DST files for the experiment of November 2002. This plot summarizes whole amount of analysis of the DST generation. The position of the mass peak depends of quality of calibration of tracking and time-of-flight detectors and the quality of their relative alignment. The variation of the mass peak indicates the time stability quality as the result of all necessary calibrations. Strong deviations from the mean value indicate serious changes. Thus, the observed drop of the proton mass peak in Fig. 3.3 corresponds to data files taken without target for test reasons (see also Appendix C). These files were excluded from the K^+ analysis, described below.
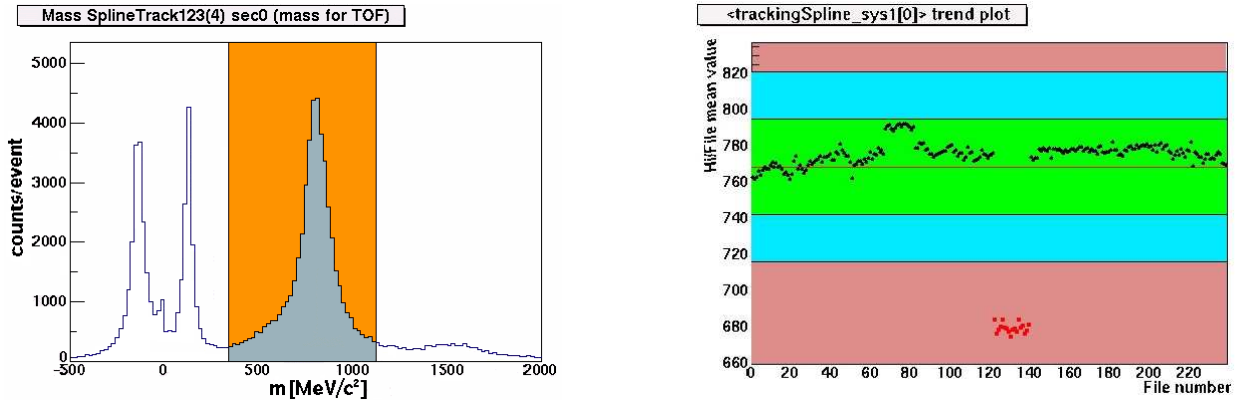

Figure 3.3: Example of the off-line DST QA diagnostics. The mean value of the reconstructed mass distribution of charged particles is calculated from the orange interval, shown in left panel. In the right panel the mean value of proton mass is monitored from file to file. A reason for fluctuations is an instability of calibration of TOF-Start detectors. The points marked in red correspond to a set of files collected without target. The proton mass peak disappears from the distribution on the left panel. Consequentially, the mean value of the distribution strongly deviates from the proton mass position. This picture is made with the help of DST QA post-analysis tool, see Appendix C.

One has to keep in mind that this is still a quite moderate result as it does not support any automatic pattern recognition, which might be desirable in case of even larger amount of QA plots. Nevertheless, the developed tool brought serious progress into the file preselection routine for DST analysis. It allows the user to perform all necessary work within several hours. Currently it is sufficient for the needs of DST QA of HADES experiment, which relies on about hundred histograms describing the quality of different detectors and subdetectors.

4 Overview of HADES tracking software

The tracking of the HADES experiment is based on the information from detectors providing coordinate measurements delivered by MDC planes. To some extend, a rough position estimate can be also done with META detectors (TOF, TOFINO and Preshower) which played an important role during the installation phase of the HADES spectrometer, when some of MDC3 and MDC4 planes were not yet installed. Therefore, we distinguish between so-called *low resolution tracking* and *high resolution tracking*. The high resolution tracking is the tracking involving the full setup of MDC1, MDC2, MDC3 and MDC4 planes installed, while the low resolution tracking is based on a mixture of (normally) two MDCs before the magnetic field (MDC1 and MDC2) and low resolution coordinate information from the META. Under the *middle resolution tracking* one understands a combination where only three MDCs are used for the tracking. The low coordinate resolution of the META detectors in case of high resolution tracking remains useful for most cases as an independent coordinate measurement used mostly for the matching of the track combinations behind the magnetic field. The RICH detector, as already mentioned in chapter 2, can be calibrated to provide the track angle measurement, might also be included in the tracking[1]. Despite the fact that the separation between tracking and non-tracking detectors is not so strict, the main principle is the same for all of them, i.e. the determination and localization of a signal left by the charged particle inside the corresponding detector (so-called hit or cluster finding procedure) and the determination of its coordinate in space. In this chapter, the focus is on the MDC tracking but the procedure can be extended to any available coordinate information from other detectors, too.

Since each MDC has 6 planes of sense wires oriented in 5 different directions, one can reconstruct the position where a track crossed the detector. It is done with the Cluster Finder routine of HYDRA[2]. The main idea is illustrated in Fig. 4.1, using a method which projects each wire with produced signal into a plane parallel to the surface of the MDC presenting the result of the projection into a two-dimensional histogram. Since the signal layers of MDC are oriented in different angles, they define paths along the corresponding wires. When the track crosses the MDC plane the corresponding wires from the layers register a signal. Each signal defines a path along the wire inside the corresponding layer, which is added to two-dimensional histogram according to the wire position and direction. After adding paths from all the wires in the event to this histogram one recognizes the signal as a spot with a peak (in three dimensional representation of the histogram) at a cross point

---

[1] Because it mainly concerns $e^{\pm}$ tracks its information is not included in the analysis presented in this work.

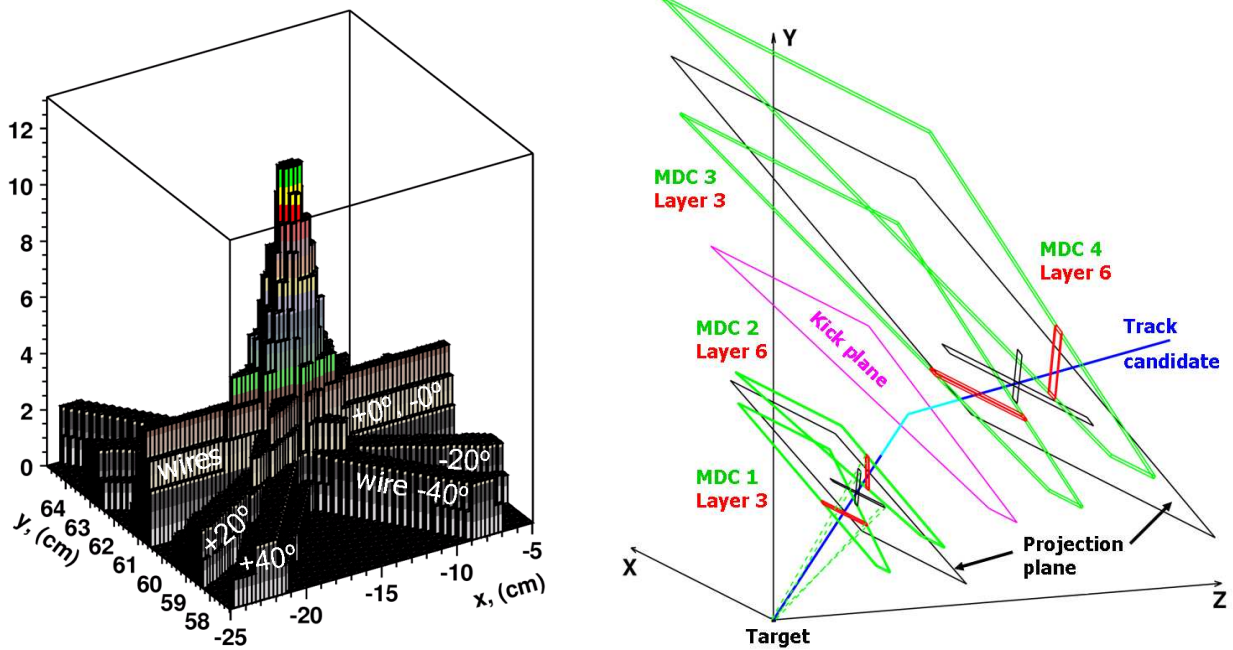[2] HYDRA is the official analysis software of the HADES experiment.

Figure 4.1: Cluster finder technique based on the projection of each "fired" MDC wire to some virtual plane represented as three dimensional plot (left panel). The region around the cluster, where all corresponding wires meet in one place, is shown here, and the inclinations of the wires are depicted. In the right panel, an illustration of the selection of the projection planes and the matching method for two segments of a track candidate is given. Figures are from [Aga00, Aga01].

of the wires. This peak is found by the routine and its position on the plane is fitted which allows one to get a good estimate of the crossing point between the track and the MDC.

The initial estimate of a hit position from the two-dimensional image is normally affected by the track inclination to the plane, because the projections of wires from different layers to the middle plane of the drift chamber depend on the orientation between track and the chamber. Therefore, this information is not a final one and has to be improved while refitting only the distance between the track and each of the wires contributing to the hit. The drift time of the avalanche electrons collected by a sense wire (measured by the corresponding TDC channel) depends on the distance between the wire and the track. Therefore, such a fit is performed directly with the time information and not with the distance, keeping in mind the distance-to-time dependence. This procedure [Aga00] is performed for each MDC detector, and as a result one gets an array of hits along the experimental setup for each event.

Such a set of hits is not the ultimate goal of the tracking. In a next step straight segments are constructed from the hit combinations. Some combinations might occur as a result of coincidence (combinatorically). Therefore, they have to be filtered out. To implement such a filter, the coincidence combination of two MDC planes (two planes before the magnet or two planes after the magnet) is used. The same two-dimensional wire image is constructed as a projection of "fired" wires to some projection plane from all wires of MDC1-MDC2 bundle[3] (and analogously from MDC3-MDC4 bundle). The projection plane is selected for each

---

[3] The information from two MDCs in this case can be considered as a whole object in a first approximation.

MDC bundle under assumption that the track originates from the target area. Therefore, some wrong combinations can be rejected at this stage, namely the ones which are not in agreement with the assumption that the track under consideration is coming from the target area [Aga01] because they would not form a peak on such projection plane.

In the outer MDCs (MDC3, MDC4) there is no target reference possibility, because these MDCs are located behind the bending magnetic field. In this case, a segment matching can be done using the intersection point provided by the first MDC segment with the surface of so called "Kick Plane" which is described in the next section. This procedure (see also Fig. 4.1) allows one to get two segments from MDC detectors and already to perform some preliminary matching of the inner and outer segments. At this point, one can proceed with the momentum determination of the track candidate.

4.1 Kickplane tracking

During the early stage of the HADES experiment some of the tracking detectors behind
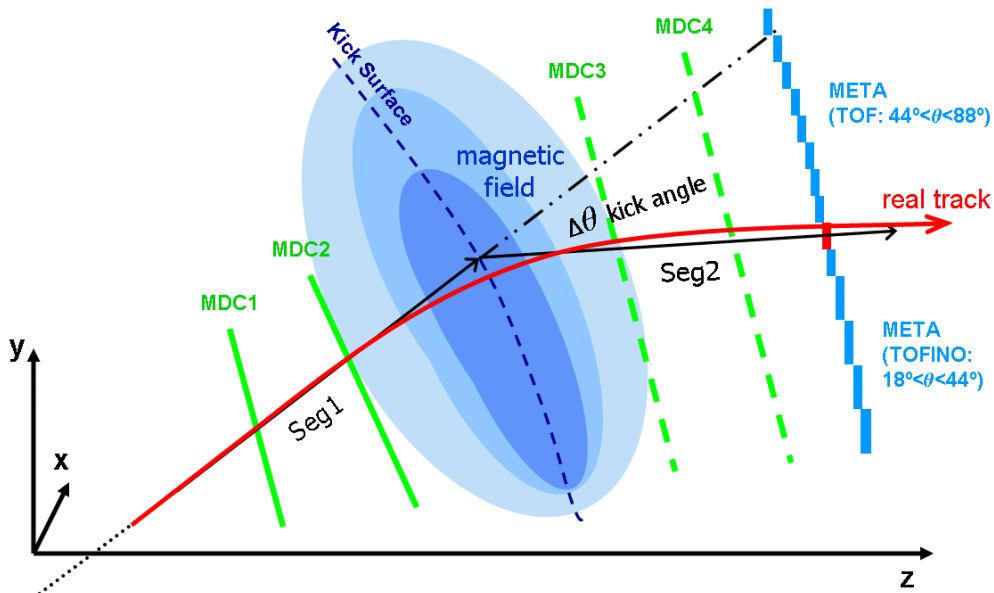

Figure 4.2: Schematic illustration of the "Kick Plane" method. The two first MDC detectors, MDC1-MDC2, and the META detector are used in this case for a coordinate measurement. The real track is shown as red curve. Having defined a Kick Surface and two hits in front of the magnetic field one can propagate a segment "Seg1" until intersection with the "Kick Plane" surface. Another segment "Seg2" is then defined by a point on the Kick Plane and the point measured by META detector. The momentum kick is done at the Kick Plane surface, and a momentum value is obtained from a lookup table provided along with Kick Plane parameterization.

the magnetic field of the spectrometer were not yet assembled. For this purpose a special tracking software based on a "Kick Plane" method was developed [Gar03]. This method is based on the knowledge that the deflection of a charged particle in a magnetic field is proportional both to the strength of the field and to the length of the path passed by the particle in the field. An approximation, where the magnetic field is assumed to be reduced in space with corresponding increase of the absolute value of the magnetic field while

keeping the same deflection as in a real case, is the principle of the "Kick Plane" method, implemented as `HKickTrack` method in HYDRA software. In practice, the implementation is based on the ultimate approximation of the particle track behavior together with magnetic field. The magnetic field along the track trajectory is assumed to be concentrated in an infinitely thin region – so called Kick Surface – which is assumed to deflect the track direction at once in the point of an intersection of the track with the Kick Surface, see Fig. 4.2. Since the deflection takes place at a certain point (in this approximation), the track trajectory is assumed to consist of two straight lines, before and after the Kick Surface. The momentum of a particle candidate before the field is $\vec{p}_{in} = \vec{Seg}_1 \cdot p$, and after the field it is $\vec{p}_{out} = \vec{Seg}_2 \cdot p$, where $\vec{Seg}_1$ and $\vec{Seg}_2$ are the direction vectors of inner and outer segments, p is the momentum of the particle, while the motion is assumed to be non-dissipative i.e. $|\vec{p}_{in}| = |\vec{p}_{out}|$. The momentum change for the track candidate is obtained from its deflection in the magnetic field. It can be defined in this approach by

$$|\vec{p}_{in} - \vec{p}_{out}| \equiv |\Delta\vec{p}| = 2p \cdot sin(\theta/2). \tag{4.1}$$

Taking into account that centrifugal force is balanced by centripetal force $B_\perp\rho = mv/q$ (where $B_\perp$ is a component of the magnetic field perpendicular to the velocity $\vec{v}$ of the particle) and a geometrical consideration which determines the relation between the track curvature radius ρ with infinitesimal length path dl and the corresponding angular change of the trajectory $d\theta$ is $d\theta = dl/\rho$, one gets

$$d\theta = \frac{q}{p}Bdl. \tag{4.2}$$

The deflection in the magnetic field can be represented as an integral along the track path

$$\Delta\theta = \frac{q}{p}\int_{l_2}^{l_1} B(\vec{r})dl = \frac{q}{p}K(l_2 - l_1), \tag{4.3}$$

where the assumption of a toroidal magnetic field configuration is taken into consideration $(B_\perp = B)$, which is a good approximation for HADES due to the design of the magnet. K is a constant being different for each track in case of a non-uniform magnetic field, and $l_2 - l_1$ is the track's length path inside the magnetic field. One can show that $l_2 - l_1 \approx a + b \cdot sin(\theta/2) + c \cdot sin^2(\theta/2)$ and therefore, using $sin\theta \approx \theta$ (for more details see [Gar03]), one gets

$$\frac{p}{q} = \frac{A}{sin(\theta/2)} + B + C \cdot sin(\theta/2). \tag{4.4}$$

In this assumption, the parameters A, B and C depend on the magnetic field region passed by the particle. This allows one to estimate the set of parameters {A, B, C} from a simulation for groups of track trajectories and use them again for the same sample of tracks while analyzing the real data. In practice, this means a tabulation of the three constants for different track groups. They depend on the track origin and the initial direction of the track. The realization results in a hyperspace look-up table for constants {A, B, C}. The realistic description of the detector in simulations is provided by GEANT simulations. This approach potentially allows one to take into account even the energy losses for different particles.

"The Kick Plane" surface is obtained for tracks originating from the same target region as intersection of the inner track segment before magnetic field and the corresponding outer segment behind the field. Correspondingly, for any initial direction of the track a unique point in space is given. Assuming that during the reconstruction procedure the emission point of tracks (target) is the same as in the simulation one can use this "Kick Plane" surface to get a virtual kick point from initial segment direction.

One can see that this approach is extremely useful, because it allows one to obtain a good momentum estimate having at hand only three measured points (one segment before and one point behind the magnetic field). In addition, it does not require much computing time during the analysis stage[4]. In case of two measured points being available behind the magnetic field, the "Kick Plane" method gives better results than for one point, although it requires a dedicated parameterization.

The achieved momentum resolution of the method was estimated in [Gar03]. It varies from 2 % to 24 % for the case of two MDCs before magnetic field with a third point measured in META detector behind the field. In the case where the MDC1-MDC2 + MDC3-META combination is used, the resolution of momentum is estimated within a range from 1 % to 7 %. The MDC12-MDC34 combination delivers a momentum resolution from 1 % to 2.2 %. All above mentioned resolutions are related to electrons within a momentum range of 150 MeV/c to 1400 MeV/c.

4.2   Spline tracking

The next generation of track reconstruction software in the HADES experiment is realized as "Spline Tracking" algorithm [Rus03]. This method, uses more realistic assumptions compared to "Kick Plane" tracking. It does not assume a single kick point of the track trajectory, but describes it as a quintic-order polynomial of coordinates inside the magnetic field and with a linear trajectory outside the field region. The assumption that the particle trajectory stays in the same plane before and after passing through the magnetic field region, which is an essential point of the "Kick Plane" method, is not required here. This allows one to make very good momentum reconstruction for the particles with negligible energy losses within more complicated magnetic field regions with reasonably limited inhomogeneity. The systematic deviations of the reconstructed particle trajectories (based on the track model[5]) from the actual one appear in momentum and also in polar and azimuthal angles. They are observed mostly in the low momentum region, occurring due to the chosen assumptions on the track model. These systematic deviations are subject of corrections afterwards, made with the help of numerical simulations, where all the effects like multiple scattering and energy loss are taken into account.

One has to mention that the quintic-spline track approximation in coordinate space means a cubic-spline approximation in space of the second derivatives which are matter of the equation of motion of charge particle in magnetic field (see Eq. (4.5) below). The principles of the method and its mathematical formalism are described, for example, in [Win74, Bug81]. A feature of the method is that, in each step of the track propagation, the integration of differential equations of motion is approximated by a spline function of fifth

---

[4]Of course, prior to the analysis phase a parameterization of the "Kick Plane" has to be done, which requires dedicated realistic simulations and takes several days of computing on a fast Pentium-III PC.

[5]The track model defines a sequence of solutions approximating the reconstructed track.

order in coordinate space. Therefore, it is a fast method including the fitting procedure (to fit splined track model to measured points in space), however it hardly gives an exact solution. This reason makes it also problematic when applied in some strongly inhomogeneous regions of HADES's toroidal magnet.

An advantage of the method is that, due to the use of interpolation, it allows one to construct the track model for practically any combination of measured points of the track. But this advantage can be reversed into a disadvantage for some cases, because in the possible fit procedure there are no extra degrees of freedom left to construct a sensitivity factor qualifying the reliability of the input data (in reality, all track points are measured with some errors). Strictly speaking, the problem of the method is its insensitivity to the noise admixture to the signal at the input of the track reconstruction model. Finally, the "Spline Tracking" method is found to be an ideal solution for a first stage of data analysis, i.e. the stage of track candidate momentum determination. It is fast and almost 100% efficient. It shows excellent results in noise-free data samples. The intrinsic momentum resolution σ_p/p is below 1%. The realistic resolution is around 2 % for electrons (again, for a momentum region from $200\,\mathrm{MeV/c}$ to $1400\,\mathrm{MeV/c}$) obtained with simulations of carbon-carbon interaction at $2\,\mathrm{GeV}$ per nucleon, where energy loss, multiple scattering and the designed resolution of the MDC detectors were taken into account [Rus03].

4.3   Runge-Kutta tracking

In some cases, especially when searching for rare particles, the background contributions become a very critical point of the analysis. The disadvantage of "Spline Tracking" mentioned above, providing momenta for all combinations of hits without a strong hint on how realistic the input was, leaves one with a need of either strong cuts or of selection of certain patterns from the input data. To avoid this, another tracking method based on the exact numerical solution of the equations of motion has been investigated. The determination of the particle trajectory is possible in this case using a step-by-step propagation in the magnetic field. Although, this needs an information on the initial coordinate, the charge, the mass, the velocity of the particle and the magnetic field in each point of space.

Mathematically one starts (like in other tracking methods) from Lorentz's force law $\vec{F} = q \cdot [\vec{v} \times \vec{B}]$ to be used in the equations of motion for an electric charge in a magnetic field,

$$\frac{d^2\vec{r}}{dl^2} = \frac{q \cdot k}{p} \left[\frac{d\vec{r}}{dl} \times \vec{B}(\vec{r}(l)) \right],\tag{4.5}$$

where $\vec{r} = \{x, y, z\}$ is the particle's coordinate vector of the track at given path position and time, l is the track path length [cm], p denotes the particle momentum [MeV/c], $\vec{B}(\vec{r}) = \{B_x(\vec{r}), B_y(\vec{r}), B_z(\vec{r})\}$ represents the magnetic field vector at each point $[kG]$, and $k = 0.2998$ $[(\mathrm{MeV/c})(1/\mathrm{cm\ kG})]$ is a scale factor.

The solution of Eq. (4.5) is equivalent to the solution of a system of two coupled differential equations of first order for the dimensionless vector $\vec{\nu(l)}$,

$$\begin{cases} \dfrac{d\vec{r}}{dl} = \vec{\nu}(l), \\ \dfrac{d\vec{\nu}}{dl} = \dfrac{q \cdot k}{p} \left[\vec{\nu}(l) \times \vec{B}(l) \right]. \end{cases}\tag{4.6}$$

Thus, the propagation through the magnetic field is given by the solution of the system (4.6). This is normally done numerically using a Runge-Kutta step-by-step integration along the trajectory. Each i-th step prediction of $\vec{\nu}_{i+1}$ is computed from the knowledge of $\vec{\nu}_i$ and $\vec{B}_i = \vec{B}(l_i)$ of the second line of (4.6) which is then used to integrate the first formula and to obtain $\vec{r}_{i+1}$ as well.

To gain precision and stability at the same step size, the fourth order Runge-Kutta integration was used which is also known as Nyström method [Abr64]. It is optimized for rounding errors and solves Eq. (4.5) numerically, actually reformulating it as

$$\frac{d^2\vec{r}}{dl^2} = f(\frac{d\vec{r}}{dl}, \vec{r}, l) \tag{4.7}$$

with expansions of $f(r', r, l)$ up to fourth order, neglecting the fifth- and higher-order corrections to the step size $h = l_{k+1} - l_k$. Defining

$$r = r_k = \vec{r}(l_k),$$

$$r' = \frac{d\vec{r}}{dl} = r'_k = \vec{r}'(l_k),$$

Eq. (4.7) then reads

$$\frac{dr'_k}{dl} = r''_k = f(r'_k, r_k, l).$$

In the method, one step h along trajectory from point "k" to point "$k+1$" is divided into four computational parts [Pre92, Bug81]:

$$\underline{\text{Part1}}: \quad K_1 = f(r'_k, r_k, l_k),$$

where the notation "k" implies that radius vector $\vec{r}(l_k)$ and magnetic field $\vec{B}(\vec{r}(l_k))$ are used also at the starting point "k";

$$\underline{\text{Part2}}: \quad K_2 = f(r'_k + \frac{h}{2}K_1, r_k + \frac{h}{2}r'_k + \frac{h^2}{8}K_1, l_k + \frac{h}{2}).$$

Here, the magnetic field is taken at $r = r_k + \frac{h}{2}r'_k + \frac{h^2}{8}K_1$, which is very close the to the step $l_k + \frac{h}{2}$. Actually, the third argument in the function $f(...)$ stays only for understanding convenience. It can be omitted without any loss of information. Here it illustrates to which step along the trajectory the current situation is referring to. The next step is

$$\underline{\text{Part3}}: \quad K_3 = f(r'_k + \frac{h}{2}K_2, r_k + \frac{h}{2}r'_k + \frac{h^2}{8}K_1, l_k + \frac{h}{2}).$$

Basically this would be identical to the previous one, but the derivative is computed at a slightly corrected position by the previous step. Finally,

$$\underline{\text{Part4}}: \quad K_4 = f(r'_k + hK_3, r_k + hr'_k + \frac{h^2}{2}K_3, l_k + h)$$

and an approximation for the "$k+1$"-st point is given by

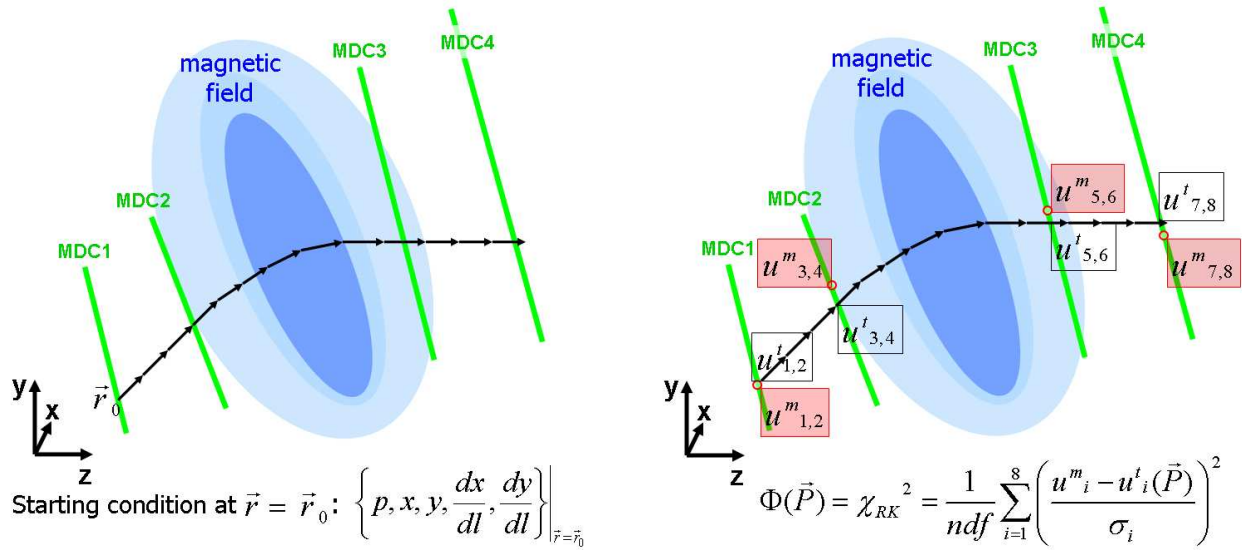$$r_{k+1} = r_k + hr'_k + \frac{h^2}{6}(K_1 + K_2 + K_3),$$

Figure 4.3: Illustration of Runge-Kutta propagation in a magnetic field with 4 measured points using start parameters (left panel) and track fitting (right panel).

$$r'_{k+1} = r'_k + \frac{h}{6}(K_1 + 2K_2 + 2K_3 + K_4),$$

where K_1, K_2, K_3, K_4 are vectors with 3 components (x, y, z) as well as r, r' and r".

These formulas show clearly the difference to the simple integration with the Runge-Kutta procedure of first order, where terms with K corrections would be absent.

To start the propagation procedure, a boundary condition is needed which is normally the one of measured track points, see also Fig. 4.3.

One can show that it is possible to find a reference frame, where the track is defined by five independent parameters $\{x, y, u_x, u_y, p\}$ which are two coordinates on a track $(l = l_0)$, two directions of a track curve at this point and a scalar momentum variable[6].

4.3.1   Track fitting

The Least Squares Method was used for the track determination from measured coordinates in tracking detectors. This uses a track model which is a full particle trajectory knowledge in analytical or numerical form satisfying the equation of motion (4.5). Let us consider the case when four tracking detectors (MDC1, MDC2, MDC3, MDC4) have delivered a combination of measurements $u^m = \{x_1^m, y_1^m, x_2^m, y_2^m, x_3^m, y_3^m, x_4^m, y_4^m\}$. The index "m" stands for the measurement-based value. Starting from an arbitrary point in space (which is one of the measured coordinates by one of the tracking detectors, say in the j-th detector (x_j, y_j)) one finds the corresponding (track model) trajectory propagating the track in the magnetic field using the Runge-Kutta method. As a result, one calculates a set of intersection points between the track and sensitive surfaces of tracking detectors: $u^t = \{x_1^t, y_1^t, x_2^t, y_2^t, x_3^t, y_3^t, x_4^t, y_4^t\}$. The index "t" stands for the track model based values. The z-coordinates are not used explicitly, but implicitly while constructing the vector of the track model intersections with the planes of the tracking detectors [7]. The dependence on the track model can be described

---

[6] For the moment being a non-dissipative motion idealization is considered.

[7] In practice, this requires a known alignment of the tracking detectors.

by five independent parameters, $\{p, x_0, y_0, (\vec{v} \cdot \vec{n}_x)/|\vec{v}|, (\vec{v} \cdot \vec{n}_y)/|\vec{v}|\}$, where p is the momentum of particle, the coordinates x_0, y_0 and the direction tangents of one point belonging to the track model. Here $\vec{v}$ is a velocity vector of the particle. In the numerical program, it is convenient to call this parameter vector as $P = \{p_1, p_2, p_3, p_4, p_5\}$. The coordinate components of the measured track point and the vector u_i^m are independent, because they correspond to x and y coordinates for track position measurements at four tracking detectors. Hence, according to the Least Squares Method, one can construct a functional to be minimized [Ead71]

$$\Phi = \chi_{RK}^2 = \sum_{i=1}^{8} \frac{(u_i^m - u_i^t(P))^2}{\sigma_i^2}, \tag{4.8}$$

where u_i^m are measured (x and y) coordinates of the track in each tracking detector, u_i^t are evaluated coordinates from track model at crossing points with each tracking detector, σ_i denotes the corresponding coordinate resolution, while the index i enumerates both x and y coordinates for 4 MDCs. The minimization of Eq. (4.8) is equivalent to the solution of the system

$$\sum_{i=1}^{8} \frac{(u_i^m - u_i^t(P))}{\sigma_i^2} \frac{\partial u_i^t(P)}{\partial p_1} = 0,$$
$$\sum_{i=1}^{8} \frac{(u_i^m - u_i^t(P))}{\sigma_i^2} \frac{\partial u_i^t(P)}{\partial p_2} = 0, \tag{4.9}$$
$$...$$
$$\sum_{i=1}^{8} \frac{(u_i^m - u_i^t(P))}{\sigma_i^2} \frac{\partial u_i^t(P)}{\partial p_5} = 0.$$

The initial-guess value for the momentum can be obtained from another tracking method (e.g., `KickTrack` or `SplineTrack`). Hits in two detectors before or after the magnet supply some approximation of the other four initial values of parameter vector P. The starting condition is provided from the hit information measured by one of the tracking detectors, the coordinate by $x_0 = x_1, y_0 = y_1$ and the direction vectors in this point are given by $(\vec{v} \cdot \vec{n}_x)/|\vec{v}| = (x_2 - x_1)/\sqrt{((x_2 - x_1)^2 + (y_2 - y_1)^2)}$ and $(\vec{v} \cdot \vec{n}_y)/|\vec{v}| = (y_2 - y_1)/\sqrt{((x_2 - x_1)^2 + (y_2 - y_1)^2)}$. Having this approximation at disposal, one puts them into Eq. (4.9) and notices that partial derivatives can be expressed via variations of the track model along one of the parameters, e.g., $\partial u_i^t(P)/\partial p_1 = (u_i^t(p_1 + \Delta p_1, p_2, p_3, p_4, p_5) - u_i^t(p_1, p_2, p_3, p_4, p_5))/\Delta p_1$. We get a linear system of equations depending on a set of unknown variations of the track model parameters p_1, p_2, p_3, p_4, p_5. The solution of the system on each step "k" gives new guess values for the parameters $p_{ik} = p_{ik} + \Delta p_i, i = 1, .., 5$. Repeating this procedure until the difference between two subsequent values of the functional become less than the required precision $|\chi_{RK}^2(P_{k+1}) - \chi_{RK}^2(P_k)|/\chi_{RK}^2(P_{k+1}) < O_{precision}$, one obtains the track model approximation for the set of initial measurements $\{u_i^m\}$, $i = 1, .., 8$. The precision was selected to be $O_{precision} = 0.009$. In addition, the approximation quality parameter χ_{RK}^2 is estimated. It quantifies the consistency of the track model and the measured track points attributed to this model. In practice, the normalized to the number degrees of freedom χ_{RK}^2/ndf value is used. This is a useful attempt of normalization in case when the number of tracking detectors used in fit is not the same for different tracks, e.g. in case of inefficiency of one of the tracking detectors. Such possibility is considered in Appendix A.

4.4   Implementation of Runge-Kutta tracking

Runge-Kutta (RK) tracking was implemented into the `mdctrackG/` library of HYDRA as a set of three classes: `HRKTrackB`, `HRKTrackBF` and `HRungeKutta`. Corresponding files are:
`hrktrackB.h,      hrktrackB.cc,`
`hrktrackBF.h,     hrktrackBF.cc,`
`hrungekutta.h, hrungekutta.cc`.

The `HRungeKutta` class originates from the momentum reconstruction routine of the KEK-246 experiment [Kan96] which was modified for the HADES purposes.

This implementation realizes high- and middle-resolution tracking options for the HADES experiment. The high-resolution tracking case is the one with four MDC hits along the track path, i.e. when hits from all four MDCs are at our disposal. Middle-resolution tracking might be needed as well in case of one missing hit, for example when one of the MDCs was not yet installed or was inefficient for a particular track.

The investigation and detailed description of these cases is delivered in Appendix A. The successful implementation of the RK tracking method was the essential prerequisite for the identification and subsequent analysis of K^+ mesons in inclusive $C + C \rightarrow K^+ + X$ production described in this thesis. The reason is the strong rejection power of RK tracking with respect to wrongly matched combinations of tracklets which is demonstrated in the next chapter.

5 Selection of K^+ mesons

The kaon production in carbon-carbon interactions with a fixed target and at beam kinetic energy of 2 AGeV is a rare process. The corresponding multiplicity (see section 5.1) is about 10^{-3} per event which makes this investigation demanding with respect to tracking. The main problem is the background contribution from proton and pion tracks, having multiplicities on the level about 1 each. The demonstration of the ability to properly resolve the track of interest from strong background contributions is an important independent check of the HADES detector performance and reliability of other results. Another context is that in the HADES experiment the signal-to-background ratio, while selecting for K^+ mesons without a special trigger, is comparable to the signal-to-background ratio when selecting for electrons with the dedicated trigger (based on RICH detector). This makes the K^+ investigation an independent check for the dielectron program of HADES. Apart from the clear technical aspect, the strangeness production at these energies has become a standard topic of interest due to its connection to physics principles and relation to properties of mesons in a dense hadronic medium (see e.g. reviews [Sto86a, Sen99, Fuc06, Sen06]).

5.1 Selecting tracks from the area of carbon target

To select K^+ tracks from the $C + C \rightarrow K^+ + X$ process one requires track candidates coming from the target area. Fig. 5.1 shows two dimensional distribution of the parameters R versus Z of the MDC segment before the magnetic field for all track combinations. R is the minimal distance between segment and beam axis Oz, and Z corresponds to the z coordinate
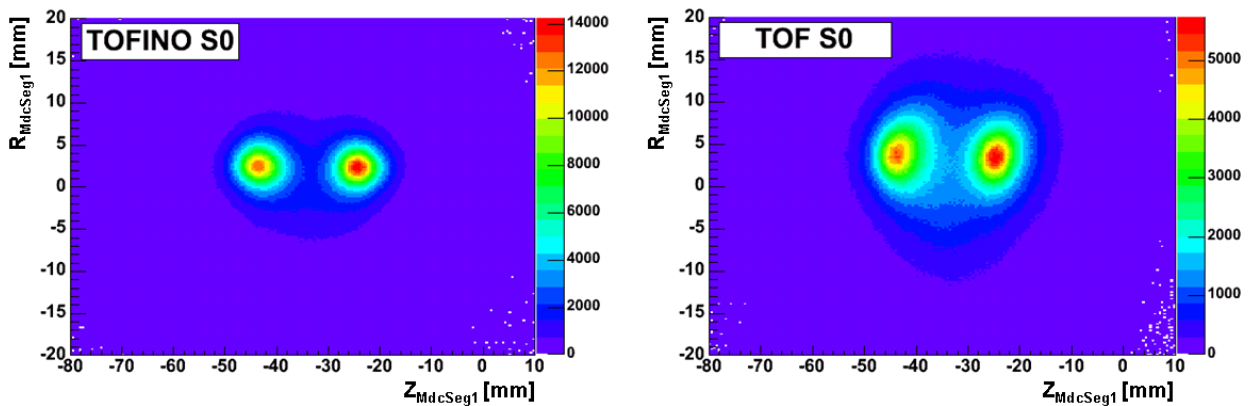

Figure 5.1: An example of R vs. Z distribution for MDC1-MDC2 segment for all track candidates registered in the upper most sector "S0". Left panel is for tracks connected to TOFINO region and right panel is for tracks within TOF region.
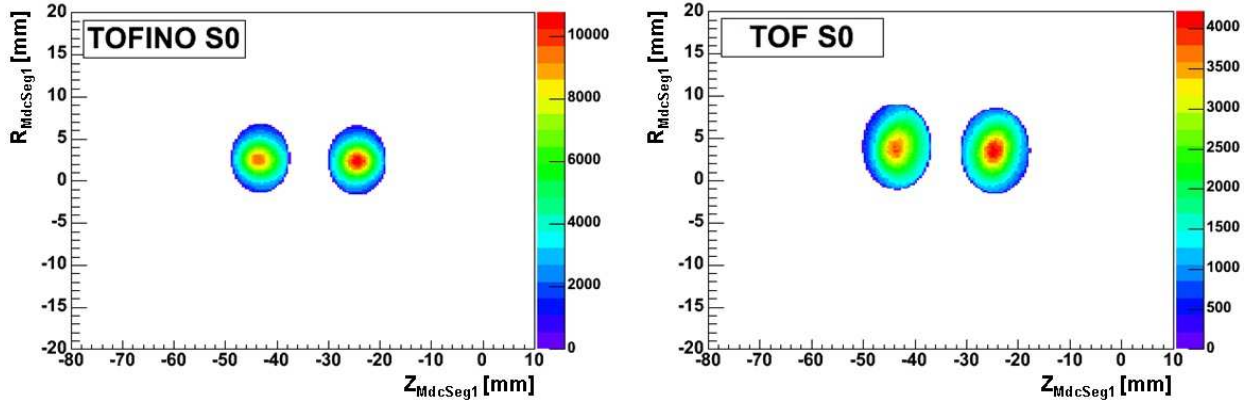
Figure 5.2: Same plots as in Fig. 5.1 but after applying the cut around target area.

of the point of closest approach between MDC segment and the axis Oz. One can see two targets with relative distance of 2 cm corresponding to the actual target setup during the experiment. The same distribution after the target selection cut is exhibited in Fig. 5.2. The cut rejects all tracklet candidates outside the elliptical region with corresponding parameters $a_x \approx 7$ mm and $a_y \approx 5$ mm.

5.2   Track candidate quality selection

For the detection of K^+ tracks one starts from the track candidate level, provided by the `HMetaMatch` container of HYDRA. This container stores all relevant combinations with the MDC segment before the magnetic field, the MDC segment after magnetic field and the META hit information. During the analysis stage it is made sure that the array of combinations does not exclude any reasonable combination[1] from a list of all possible combinations $HMdcSeg1 \bigotimes HMdcSeg2 \bigotimes META$.

Although some obviously wrong combinations, which can not be matched, are already rejected from the consideration, there are many cases left where it is difficult to decide on the level of momentum analysis whether it is a real combination or a wrong one. This is especially the case for such combinations of track candidates in which several MDC hits occur nearby to each other, nevertheless they have to be taken into account as different MDC segments. Such closely located MDC segments can point to the same hit of the META detector, which coordinates are known with a large error as compared to the precision of the MDC detectors. This means that several track candidates constructed from MDC hits can point to a single META hit.

Therefore one can not easily decide which track candidate in MDCs is attributed to the META hit. The problem of uncertainty can be also on the side of MDC detector, taking into account that the MDC cluster finding algorithm can also recognize as clusters these signals which are originating from the electronic noise induced at TDCs of some wires[2]. That makes it possible to have in addition a fraction of wrong combinations of MDC segments and as a

---

[1] This implies a certain matching between MDC and META hits, which is done in parallel with "Spline Tracking".

[2] This depends on the efficiency of the layers in the MDC and the required minimum numbers of wires in cluster setting to recognize the cluster as a real one.
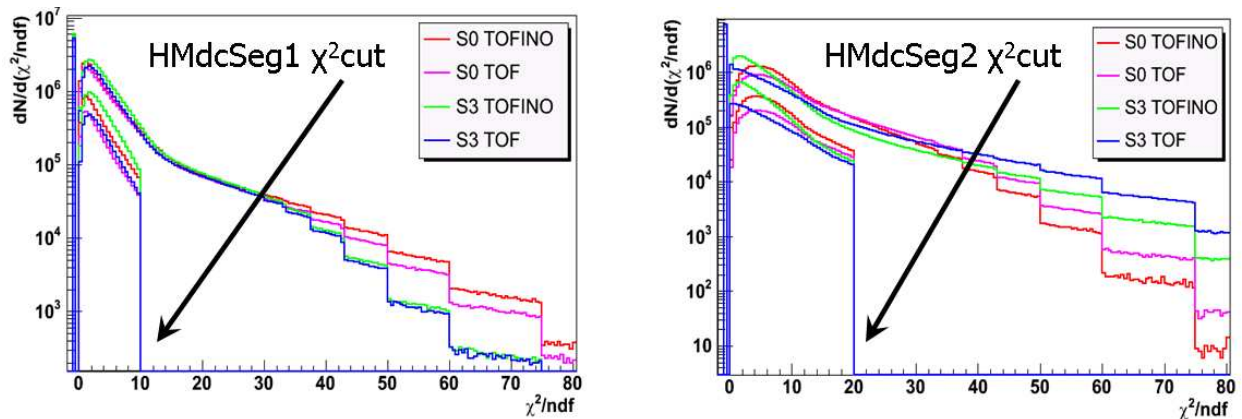
Figure 5.3: Illustration of the cut applied to the result of χ^2 fit performed with MDC segments before (left panel) and after (right panel) the magnetic field. The various curves depict distributions corresponding to the TOF and TOFINO parts of META detector from two sectors S0 and S3. The arrows indicate cut limits for the χ^2/ndf of the least-squares fit in the corresponding MDC segment.

consequence the presence of wrong track candidates in the analysis. Another aspect has a clear physical ground, namely the possibility that a particle can produce secondaries while traveling through the detector.

One way to control these possibilities is to use an information from the `HMdcSeg` class, which provides a χ^2 value after the least-squares fit of the TDC time-to-distance dependence of the track with all MDC wires involved in the corresponding cluster. Small χ^2 values of the fit indicate that the collected information from the wires is in agreement with the model of a linear tracklet in a segment (before or after the magnet). Large χ^2 would correspond mostly to cases where one of the clusters is formed by noise or has a significant number of wires affected by noise. The χ^2 cut in both segments is done to limit the contribution of MDC segments which do not agree with the assumption of a linear track model in the region outside the magnetic field – see Fig. 5.3, where χ^2 distributions corresponding to inner MDC segment ($HMdcSeg1$) and outer MDC segment ($HMdcSeg2$) are presented before and after selection cuts; the effect of the χ^2 cut is indicated by arrows.

Another separation between true and false track candidates can be established by exploiting the matching between the track candidate obtained from MDC detectors and the hit observed in the META detector, using Runge-Kutta track propagation from the last MDC till the surface of the META detector with the matched hit. The distribution of distances between the point taken from Runge-Kutta propagation of the track model till the surface of META subdetector involved in hit and the actual hit point on META detector is presented in Fig. 5.4. One sees histograms of track candidates before and after all selection cuts. The effect of the cut on MDC-META matching is indicated by the arrow.

The next possibility to ensure a high track reconstruction quality is to take into account the energy loss information in plastic scintillator pads of the META detector and to correlate it with the particle velocity measured via the time-of-flight signal taken from META detector and the length of track trajectory obtained with the chosen track model. According to the Bethe-Bloch formula the energy loss of a charged particle in a medium is inversely proportional to its velocity. Therefore it is convenient not to plot the dE/dx vs. β but $\beta^2 \cdot dE/dx$ vs. β dependence, which is to first order constant and therefore more convenient
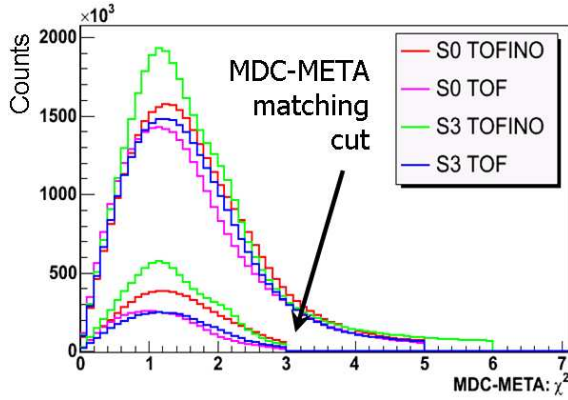
Figure 5.4: Illustration of the cut applied on the distance between two points on the surface plane of META detector: the first point from Runge-Kutta track propagation from last MDC till the surface of META detector, while the second point is a hit measured with the META detector. This allows for an additional cut to reject badly matched objects using information from track model after the Runge-Kutta tracking/fitting. The arrow points to the selected cut limit.
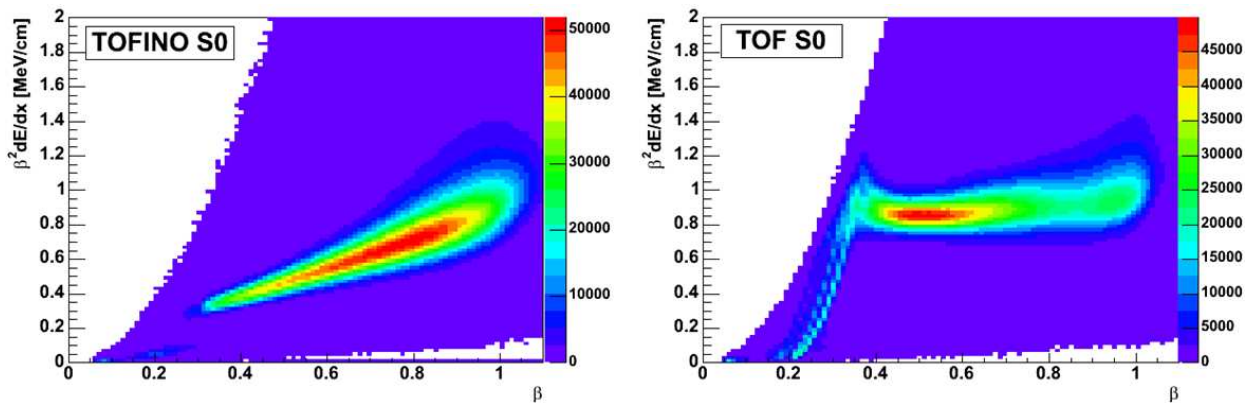

Figure 5.5: $\beta^2 \cdot dE/dx$ as a function of the particle velocity β which is useful to distinguish between good and wrong matching between track candidate taken from hits in MDC detectors and hits in TOF and TOFINO (META) detectors. Sector 0 is taken for illustration. The difference between TOFINO and TOF detector is due to different calibrations applied; it has no effect on the selection possibility.

for applying graphical cuts. The meaning of the cut is to reject such MDC track candidates matched with META hits which do not agree with the Bethe-Bloch formula and therefore correspond to wrong MDC-META combinations (e.g. cross-scattered particles not originating from the target). The distribution of track candidate energy loss before and after the cut for charge-one particles is shown in Figs. 5.5 and 5.6, respectively.

Finally, another powerful cut on χ^2_{RK} obtained from the Runge-Kutta track fitting can be established. This allows one to suppress track candidates based on coordinate measurements provided by the MDC detectors which are not in agreement with the equation of motion of a particle with charge $|q| = 1$ in the magnetic field of HADES spectrometer. This is a very effective cut since it is sensitive to events with some noise admixture to the hit points measured with MDC and META detectors. The influence of the χ^2_{RK} cut was investigated with realistic UrQMD simulation of C+C collisions at fixed target with the kinetic beam energy of 2 AGeV followed by GEANT simulation and full data analysis, see Figs. 5.7 (with target cut and quality cuts) and 5.8 (with target cut, quality cuts and additional χ^2_{RK} cut). The corresponding comparison based on analysis of the experimental data of $166 \cdot 10^6$ events is presented in Fig. 5.9. The K^+ signal-to-background ratio improvement due to the additional cut of $\chi^2_{RK}/ndf < 8.55$ of Runge-Kutta tracking/fitting is more than a factor 3
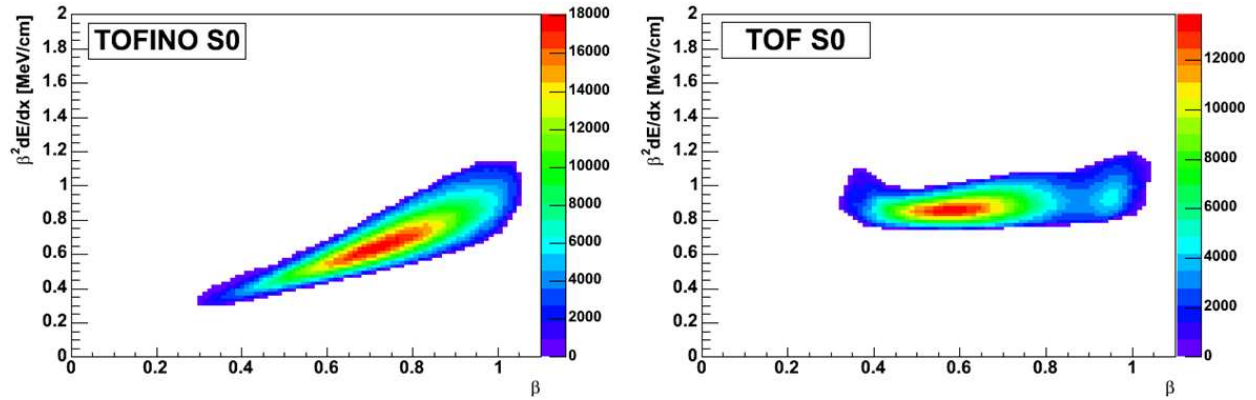
Figure 5.6: The same distribution as in Fig. 5.5, but here a cut is applied to reject wrong matching between track candidates taken from hits in MDC detectors and hits in TOF or TOFINO detector. The different calibrations of TOFINO and TOF detectors do not affect the possibility to establish a reliable cut on energy loss of track candidates.
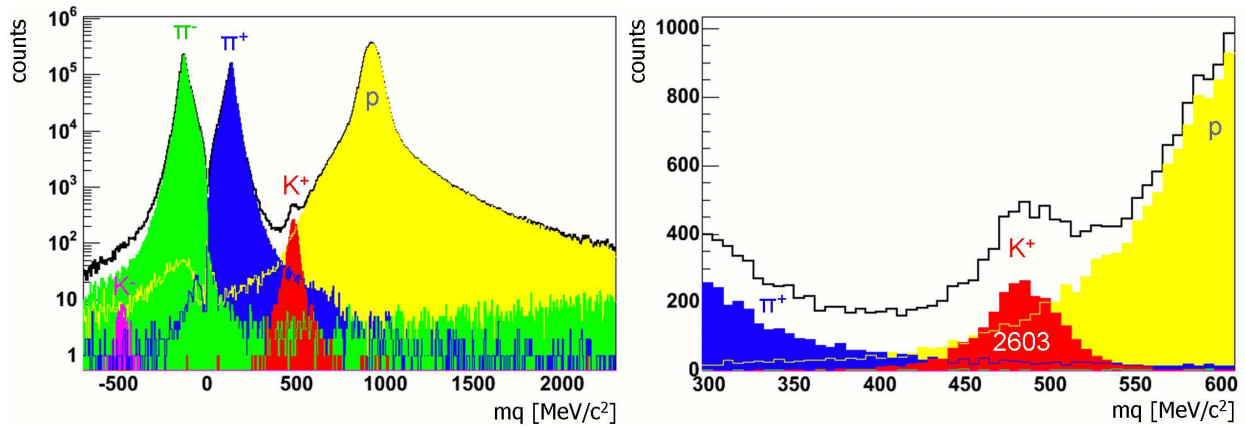

Figure 5.7: Data analysis of $71 \cdot 10^6$ events obtained from simulations of C(2 AGeV)+C collisions (UrQMD with subsequent GEANT propagation) in TOF region (sectors 0 and 3) with target cut and quality cuts applied. Distribution of tracks as a function of $q \cdot m$ for particles with charge $q = \pm 1$ (in units of absolute electron charge $|e|$). Different particles are indicated by different colors (π^- in green, π^+ in blue, protons in yellow, K^+ red and K^- in pink, while black histogram represents the total yield). The identification is taken from KINE information of GEANT before the magnetic field. The vertical axis on the left part is in a logarithmic scale while the right part is in linear scale for a region selected around K^+ mass. The total number of K^+ tracks after these cuts is 2603.

for the experimental data, while the loss of track candidates due to the cut in this case is only 30 %.

All together these "quality" and "target selection" cuts (except the cut on χ^2_{RK}/ndf) reduce the amount of accepted track candidates by 80 %. Another 30 % (out of the left over from previous cuts) are cut away by the $\chi^2_{RK}/ndf < 10...20$ cut (depending on sector). Finally, one has only about 15 % selected good tracks from all previous track candidates. The illustration of the χ^2_{RK}/ndf cut adjusted to keep 60 % of track candidates for two sectors in TOFINO and TOF regions of META detector is exhibited in Fig. 5.10.
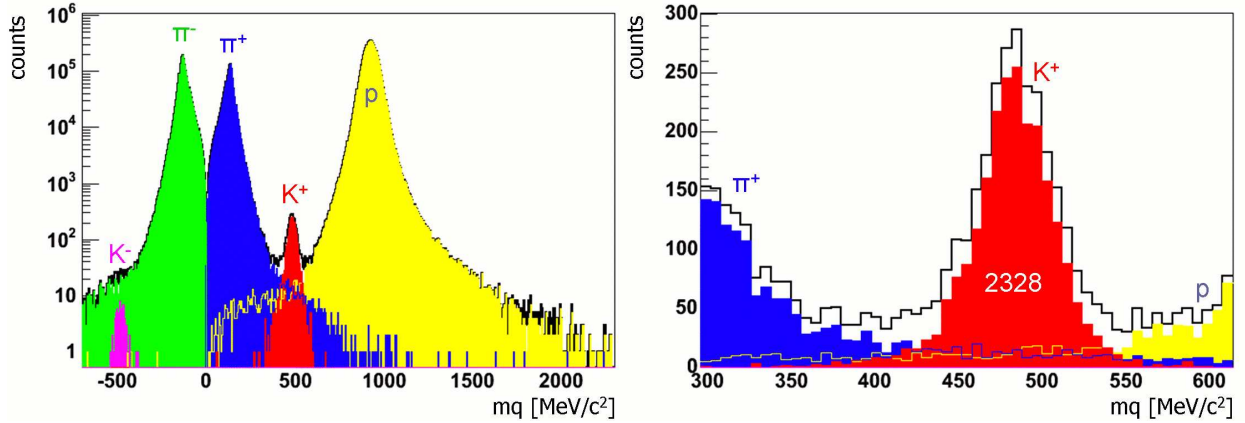
Figure 5.8: The same as in Fig. 5.7, but with additional $\chi^2_{RK}/ndf < 8.55$ cut applied. A strong background suppression is visible, while the loss of signal (K^+ tracks) in this case is only 10.5 %.
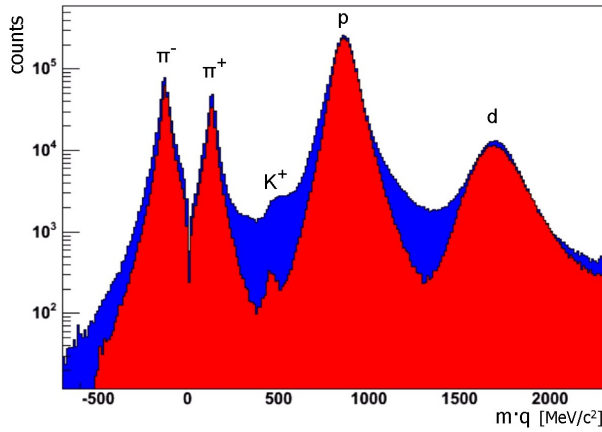

Figure 5.9: Illustration of the χ^2_{RK} cut effect applied to experimental data in sector 0 of TOF region. Blue histogram represents all track candidates passing target and track quality cuts, while the overlaid red histogram represents the effect of applying the additional cut $\chi^2_{RK}/ndf < 8.4$. Horizontal axis is mass multiplied by the charge of particle. Vertical axis is for counts per bin.
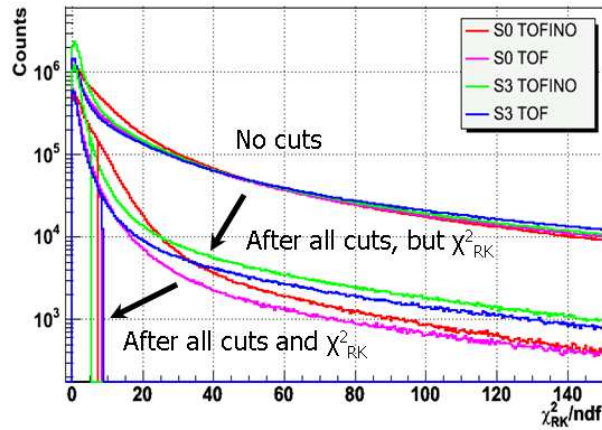
Figure 5.10: Illustration of the cut applied on $\chi^2_{RK}/ndf < 10.0...20.0$ using the Runge-Kutta tracking/fitting information. The cut is adjusted to keep about 60% track candidates left after all other quality/matching cuts applied before. Colors indicate different sectors and parts of META detector. The figure shows the effect of different cuts plotted as a function of Runge-Kutta quality parameter, starting from no cut applied, presenting the effect of track target and quality cuts and ending with the χ^2_{RK} cut.

5.3 $C + C \rightarrow K^+ + X$ process selection

Particle identification can be done using the correlation between momentum of the particle and the velocity. The mass is calculated via $m = p\sqrt{(1 - \beta^2)}/\beta$ with the particle momentum p, which is defined by the tracking, and velocity β (in units of velocity of light), which is

calculated from the time-of-flight. Ideally, the mass of a given stable particle is a fixed value. In reality, the momentum reconstruction in magnetic field and time-of-flight registration accuracy depends on the velocity of the respective particle. Therefore, one does not obtain a set of sharp mass peaks for each particle species but rather a continuous spectrum with peaks around corresponding particle masses. In order to take into account possible momentum (velocity) dependence of the mass estimate as well as mass resolution at different momenta, it is useful to consider a distribution of $p \cdot q$ versus squared mass for each track, see Fig. 5.11. In order to perform reliable particle identification the momentum range was divided into several intervals: $200 < p < 300 \, \text{MeV/c}$, $300 < p < 400 \, \text{MeV/c}$, $400 < p < 500 \, \text{MeV/c}$, $500 < p < 600 \, \text{MeV/c}$, $600 < p < 700 \, \text{MeV/c}$. Within each interval the selection of K^+ meson was performed individually. One observes that K^+ tracks in the TOFINO detector
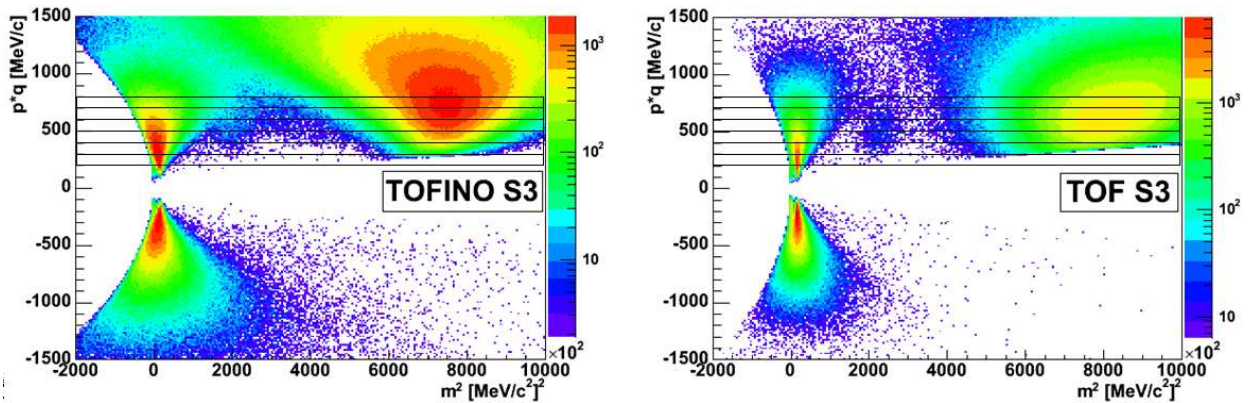

Figure 5.11: Distribution of $p \cdot q$ vs. m^2 for all good tracks in sector 3 of the HADES setup. Particle identification of K^+ is based on individual mass distributions for each momentum range indicated by horizontal lines.

can be well separated from protons and pions only in the momentum range of $200 < p < 500 \, \text{MeV/c}$, while in the TOF region a good separation is achieved up to $p \approx 700 \, \text{MeV/c}$, see Fig. 5.12 for sectors 0 and sector 3.

5.4 Background contribution estimate

The aforementioned cuts are optimized to keep the best signal to background ratio, while keeping reasonable K^+ statistics for the experimental data.

A realistic way to estimate the background contribution to K^+ candidates is to fit the mass distribution for each momentum interval with a function consisting of signal plus background contribution. The signal is assumed to be Gaussian, while the background is approximated (modelled) by an exponential function plus some constant which is a good approximation within a small window around the K^+ mass peak. An illustration of the signal-to-background estimate performed after the analysis of the real data for the TOFINO detector in sector 3 is illustrated in Fig. 5.13 for the momentum range $300 < p < 400 \, \text{MeV/c}$. The results for all momentum ranges from TOF and TOFINO detectors are summarized in table 5.1. The polynomial description of the background around the K^+ mass peak does not change the result by more than by 15 % as compared to an "exponential plus constant" one. In total, $166 \cdot 10^6$ events of experimental data were analyzed, in two opposite sectors
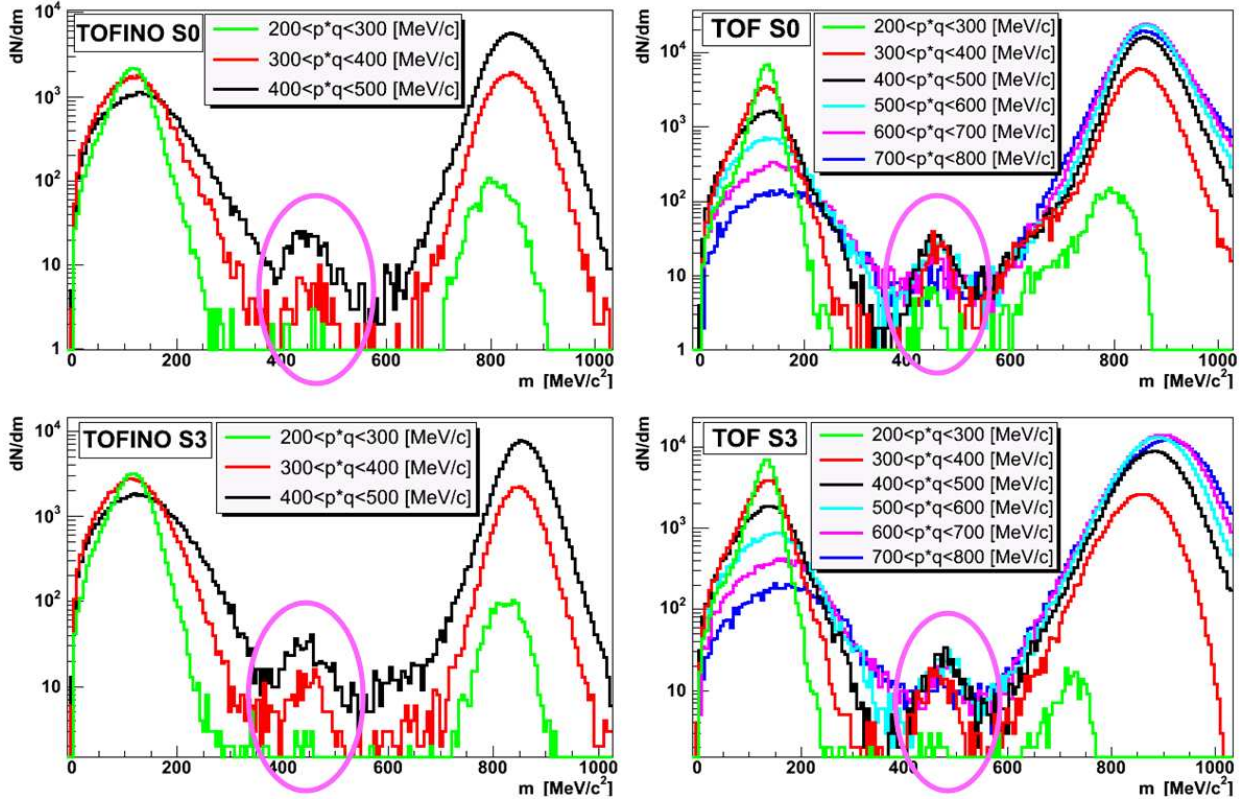
Figure 5.12: The mass distribution for all good tracks in sector 0 and sector 3 of the HADES setup in both regions TOFINO and TOF. Particle identification of K^+ is done individually for each momentum range distribution, indicated by histograms with different colors, the K^+ peaks are encircled.

(upper "S0" and down "S3") with high-resolution tracking setup of MDC detectors, and finally 3686 tracks were assigned to K^+ mesons. The fraction of background contribution is about 30 % of tracks. This allows one to estimate an overall signal-to-background ratio as $N(K^+)/N(bg) = 2562/1124 = 2.3$ and an total significance $sig/\sqrt{(sig + bg)} = 42.2$ within the selected region; bg stands for the background number, while $sig = N(K^+)$.

Momentum range	TOFINO $bg/(sig + bg)$		TOF $bg/(sig + bg)$		TOFINO $N(K^+)/N(bg)$		TOF $N(K^+)/N(bg)$	
MeV/c	S0	S3	S0	S3	S0	S3	S0	S3
$200 < pq < 300$	< 10%	< 10%	< 10%	< 10%	13/2	21/4	40/6	25/3
$300 < pq < 400$	25%	20%	8%	13%	60/20	124/31	322/21	171/26
$400 < pq < 500$	26%	36%	9%	12%	274/95	313/178	400/61	327/43
$500 < pq < 600$	——	——	20%	28%	——	——	303/76	251/98
$600 < pq < 700$	——	——	42%	45%	——	——	120/90	126/108

Table 5.1: Background contribution ($bg/(sig + bg)$) and signal-to-background ($N(K^+)/N(bg)$) estimate for several momentum ranges in TOFINO and TOF separately. Only the fully equipped sectors, S0 and S3, were analysed.
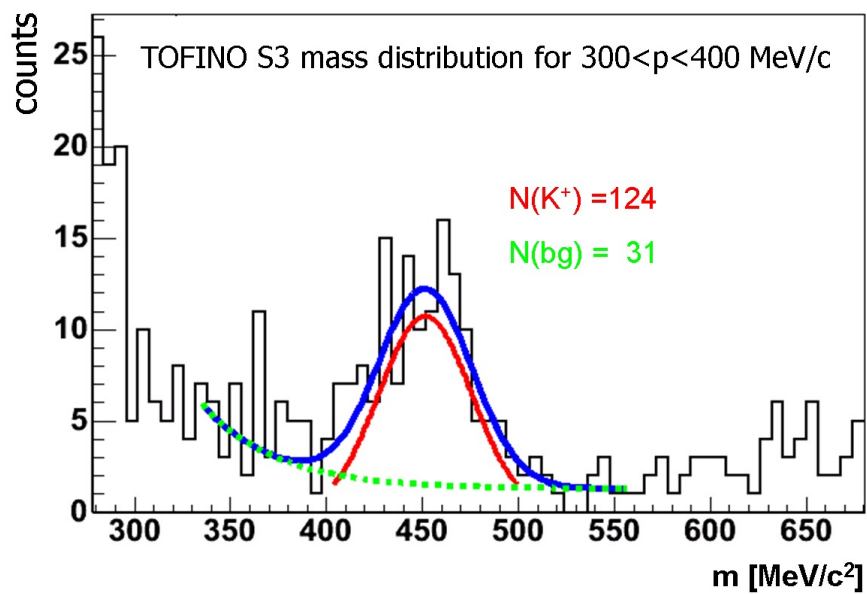
Figure 5.13: An illustration of the signal-to-background estimate. The fit function is Gaussian for the signal, and "exponential plus constant" for the background is used for the common fit (indicated by blue curve). The estimate of the signal is shown by the red curve, while that for the background is indicated by the green dashed curve. Estimated numbers are presented in corresponding colors, too.

6   Determination of K^+ yield

The reaction C+C was measured by the HADES experiment in November 2002 at a kinetic beam energy of $2\,\mathrm{GeV}$ per nucleon and is analyzed here with respect to K^+ production. The beam intensity was $(1-2)\cdot 10^6/\mathrm{s}$. About $210\cdot 10^6$ events were recorded with magnetic field. The superconducting magnet was operated with a current of $I = 2497\,\mathrm{A}$, which corresponds to a magnetic field setting of $0.5\,\mathrm{T}$. The experiment was performed with two types of trigger conditions: *(i)* the first level trigger (LVL1) which is responsible for preselecting of non-peripheral collisions and *(ii)* the second level trigger (LVL2) which is needed to select events with electron (positron) track candidates. Fractions of each of the triggered events were written into the data stream with a certain proportion. The multiplicity trigger LVL1 was operated under two conditions with corresponding scaling factors:

- META multiplicity (TOFINO + TOF) ≥ 2 for about $15\,\%$ of the events;

- META multiplicity (TOFINO + TOF) ≥ 4 for about $85\,\%$ of the events[1].

The LVL2 trigger requires at least one lepton candidate, in addition to the LVL1 trigger. The lepton candidate was defined by the azimuthal correlation $|\phi_{RICH_{IPU}} - \phi_{META}| < 8° + \phi_{RICH}/4$ between a hit registered within RICH and a hit in the META (SHOWER, TOFINO and TOF) detector. The matching is done section vise. The zero value of ϕ_{RICH} and ϕ_{META} is in the middle of sector. The $\phi_{RICH}/4$ term is needed to take into account the track deviation in azimuthal angle due to second order effects related to magnetic field close to the coils of magnet (i.e. the effect increases at the sector edges, close $\phi = \pm 30^o$), see [Toi04].

The third DST generation was used for the present analysis. Only official HADES DST files from the time intervals of stable operation of the experiment were taken into account. In addition to that, the selection of files accepted for subsequent analysis was performed with help of DST QA. For example (see Fig. 3.3 in chapter 3), the reconstructed proton mass distribution and its long-term stability was monitored for different sectors.

The selected files with total statistics of $166\cdot 10^6$ events were used in our analysis. In this sample, approximately $53.8\,\%$ of events were taken with condition of pure LVL1 trigger and $46.2\,\%$ with LVL2. The influence of the trigger conditions is discussed at the end of this chapter.

Two sectors (S0 and S3) out of six, covering 1/3 of azimuthal angle, were capable of high resolution tracking which is used in this work for K^+ identification and analysis. Another two sectors (S1 and S4) allowed for middle resolution tracking, but were not used in this analysis due to lower signal-to-background ratios not leading to a clean sample with sufficient statistics. An estimate of possible gain of statistics from additional consideration of these

---

[1]This condition selects non-peripheral collisions of about $70\,\%$ of the geometrical cross section.

middle-resolution sectors is on the level of 30 %. The corresponding decrease of statistical errors is small compared to the expected increase of the systematical errors if these sectors were incorporated in the analysis.

An unreliable performance of several strips of the START detector during the experiment caused problems for the absolute counts of beam particles determination. This necessitates a relative normalization for the analysis of November 2002 data. Therefore, to obtain a K^+ cross section estimate we rely on relative kaon to pion multiplicities, where pion multiplicities are taken from another experiment [Lau00, Stu01b].

Another problem occurred in some of the readout mother boards of the MDCs, which caused efficiency drops in some of the regions of the tracking detectors. The problem was carefully taken into account in GEANT simulations within the official HADES analysis framework. The necessary corrections were taken into account in the analysis. They are explained in detail in the following section.

6.1 Detection efficiency correction for K^+ tracks

The detection efficiency for kaon tracks can be determined by using the full chain of simulation and subsequent analysis, see Fig. 6.1. 10^7 K^+ tracks were generated with Pluto[2] with effective inverse slope parameter of $T = 78\,\mathrm{MeV}$ and zero radial expansion velocity of fireball, $\beta_r = 0.0$. On the next step, these tracks were propagated through the HADES official simulation hGeant [Hol05] (which is based on GEANT 3.21 package [Gea93]) where digitization and known individual detector efficiencies were taken into account based on the estimates obtained from the experimental data. Later the files containing the results of GEANT data were analyzed with HYDRA program in the same way as the experimental data. The obtained DSTs were compressed into micro DSTs containing only the meaningful information for hadron analysis. Finally, the K^+ selection was performed as described in the previous chapter. This allows one to make a realistic estimate of geometrical and tracking efficiency.
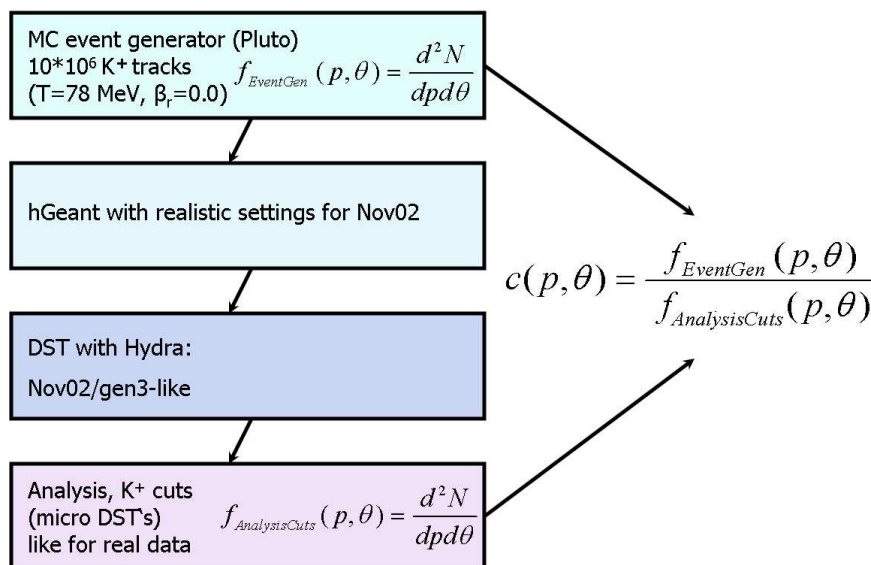

| MC event generator (Pluto) |
| 10*10^6 K+ tracks |
| (T=78 MeV, β_r=0.0) |

$$f_{EventGen}(p,\theta) = \frac{d^2N}{dpd\theta}$$

hGeant with realistic settings for Nov02

DST with Hydra:
Nov02/gen3-like

Analysis, K+ cuts
(micro DSTs)
like for real data

$$f_{AnalysisCuts}(p,\theta) = \frac{d^2N}{dpd\theta}$$

$$c(p,\theta) = \frac{f_{EventGen}(p,\theta)}{f_{AnalysisCuts}(p,\theta)}$$

Figure 6.1: The detection efficiency procedure for K^+ tracks. The correction is based on realistic simulations. Particle track distributions $d^2N/dpd\theta$ after full analysis are related to that before track propagation through hGeant. The same scheme is valid for pions.

---

[2]Pluto is a Monte Carlo simulation event generator of hadronic interactions [Kag00, Kag05].

Let us define the corrections as

$$
c(p, \theta) = \begin{cases} \dfrac{f_{EventGen}(p, \theta)}{f_{AnalysisCuts}(p, \theta)} & \texttt{if} \quad f_{AnalysisCuts}(p, \theta) \neq 0, \\[2em] 0 & \texttt{if} \quad f_{AnalysisCuts}(p, \theta) = 0, \end{cases} \tag{6.1}
$$

where $f_{EventGen}(p, \theta) = \frac{d^2N}{dpd\theta}$ is a two-dimensional distribution (histogram) of K^+ tracks produced by the event generator as a function of momentum and polar angle. $f_{AnalysisCuts}(p, \theta)$ $= \frac{d^2N}{dpd\theta}$ is a similar distribution of K^+ tracks left after the hGeant propagation, followed by the full analysis chain including K^+ selection cuts. The K^+ is an unstable particle with decay constant of $c\tau = 3.713\,\mathrm{m}$. Therefore K^+ mesons undergo noticeable decay while flying through the HADES spectrometer. This is taken into account by Eq. (6.1) since a proper simulation of hadron decays is done within GEANT propagation.

The binning of the histograms obtained after event generation and after full analysis chain which are used for correction was kept identical to allow direct bin-by-bin comparison. The bin size is $2°$ in polar angle and $50\,\mathrm{MeV/c}$ in momentum, which is larger than the achieved resolution in θ and p in the analysis, i.e. well above the detector response function. Therefore, unfolding of the detector response can be neglected in this case, and a bin-by-bin comparison is allowed to get correction coefficients.

Taking into account the correction for detection efficiency one can now construct the corrected $d^2N/dpd\theta$ distribution from the distribution of particles registered in the detector $d^2N^{det}/dpd\theta$ as

$$
\frac{d^2N}{dpd\theta} = c(p, \theta) \cdot \left(\frac{d^2N^{det}}{dpd\theta} \right). \tag{6.2}
$$

6.1.1   TOF and TOFINO overlap

Since particle identification is done with the help of TOF and TOFINO parts of META detector, one has two independent regions for efficiency and tracking correction which have to be treated specially in the overlap region of (p, θ) phase space. Despite the fact that tracks which have two simultaneous measurements from TOF and TOFINO (in case of geometrical overlap of both detectors) are always analyzed basing on the TOF measurement only (which has better accuracy compare to TOFINO), the tracks coming from the overlap region, but measured only by one of TOF or TOFINO detectors, still appear in the overlap region of these detectors. Therefore the overlap region is treated additively, as sketched in Fig. 6.2 and quantified in Eq. (6.3). Defining the efficiency relation as

$$
f_{EventGen}(p, \theta) = c(p, \theta)(f_{TOF}(p, \theta) + f_{TOFINO}(p, \theta)), \tag{6.3}
$$

one can compute correction coefficients in any region of the detector acceptance from simulations with subsequent application of the correction to the experimental data. The (p, θ) distribution of selected K^+ tracks from the experimental data after correction is presented in Fig. 6.3.
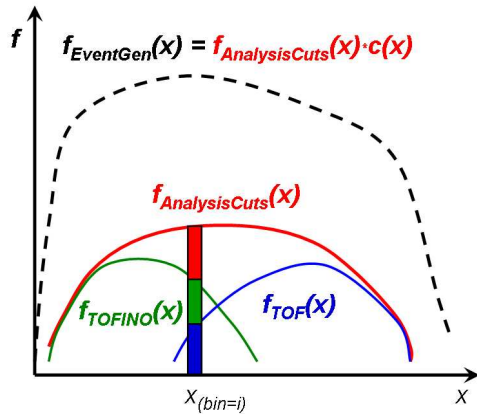
Figure 6.2: The treatment of the overlap region of TOF and TOFINO. The black dashed line stands for the distribution of tracks generated with the event generator. The tracks measured within TOFINO and TOF regions are represented by green and blue curves, respectively, and the red curve is the sum of them. The figure shows that in case of two detectors with partial overlap one computes correction coefficients using both regions $c_{TOF}(p, \theta)$ and $c_{TOFINO}(p, \theta)$. See text for details.
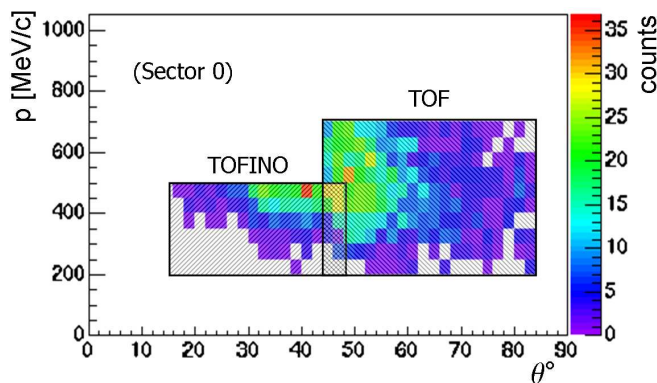

Figure 6.3: p vs. θ distribution of selected K^+ tracks after detection correction. Acceptance regions corresponding to TOFINO and TOF regions are indicated by rectangular areas with different textures. The distribution from sector S0 is presented.

6.2   Detection efficiency correction for π^+ and π^- tracks

The production of charged pions in C+C reactions was measured by other experiments (see e.g. [Lau00]) at beam energies around 2 AGeV. Our interest in charged pion tracks is caused mainly by the necessity to normalize the number of kaon tracks to the number of beam particles. For that reason, one does not need to cover a very large phase space, but rather can use a smaller region with better quality of particle identification. Therefore, the selection of π^+ and π^- tracks is done only inside the TOF region of META detector with additional graphical cuts applied to the same two dimensional plots of $p \cdot q$ as a function of m^2. The upper limit of momentum in this case can be taken as 1500 MeV/c, while the background contribution estimated from the simulation is well under 3 % for tracks from the selected area. An example of particle-identification selection of π^+ and π^- mesons in sector S0 of TOF region is presented in Fig. 6.4.

The detection-efficiency correction for π^+ and π^- tracks is performed in the same way as for K^+ tracks (see also Fig. 6.1), except of three minor differences. The first one concerns Pluto simulations, where corresponding inverse slope parameter $T = 82$ MeV with radial expansion velocity $\beta_r = 0.3$. The second feature is a better momentum resolution for pions and much richer statistics, which allows us to make finer binning for correction histograms in momentum p of 25 MeV/c, while keeping the θ binning the same as before, 2°. The third is that charged pions can be assumed as stable particles with respect to the length
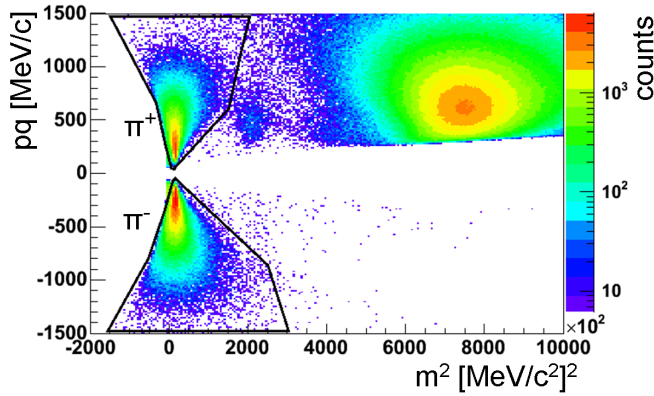
Figure 6.4: Two dimensional distribution of particle momentum times charge as a function of squared mass (experiment). An example of selection of π^+ and π^- tracks in TOF region of sector S0. The corresponding graphical cuts are indicated as black contours.

of HADES spectrometer[3] (nevertheless, their decays are also taken into account in the considered framework).

The distributions of π^+ and π^- tracks before and after corrections in TOF detector are presented in Fig. 6.5.
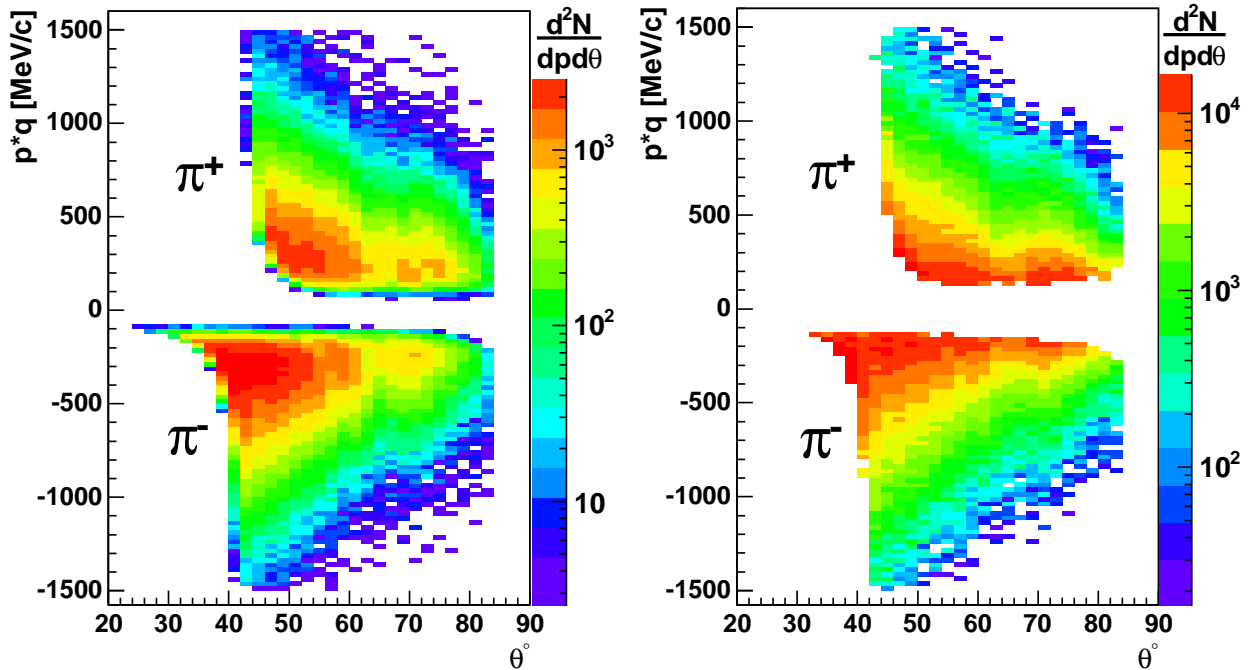
Figure 6.5: An illustration of the detection-efficiency correction for π^+ and π^- tracks in TOF detector of sector S0. In the left panel, the detected $d^2N/dpd\theta$ distributions are presented, while on the right panel the distributions after the correction are shown. The differences in distributions of π^+ and π^- mesons are caused by different acceptances for positive and negative particles due to the influence of the magnetic field. Corrections for sector S3 are done in the same way.

---

[3] The decay length of $\pi^\pm$ is $c\tau = 7.8$ m, [Par98].

6.3   Estimate of $C + C \rightarrow K^+ + X$ cross section

The differential cross section of particle production can be written as

$$\frac{d^2\sigma_{(\kappa)}}{dpd\Omega} = \frac{M}{N_A \cdot d \cdot N_{beam}} \cdot \frac{1}{\epsilon_{dead} \cdot \epsilon_{trig} \cdot \epsilon_{(\kappa)det}(p,\theta)} \cdot \frac{dN^{det}_{(\kappa)}}{dpd\Omega}, \quad (6.4)$$

where κ is the particle type, p and Ω are momentum and solid angle in the laboratory reference frame, M and d are the molar mass and thickness of the target, N_A is the Avogadro number, ϵ_{dead} is the efficiency due to electronics (dead time) occupancy, ϵ_{trig} represents the trigger efficiency, $\epsilon_{(\kappa)det}(p,\theta)$ is the detection efficiency for particle type κ, and $N_{(\kappa)det}$ is the number of particles of species κ detected inside some phase space region of (p, Ω). Under detection efficiency we assume the efficiency of cluster detection in MDCs and META detectors as well as the efficiency of proper track reconstruction including quality, target and Runge-Kutta cut efficiencies. As already mentioned, the estimate of the detection efficiency is done with the help of realistic simulations, which are based on estimated efficiencies of individual detectors taking experimental data. This efficiency may depend on the type of particle, because different particles may produce different ionization in tracking detectors. Also quality selection cuts may cause different effects. The trigger efficiency may also vary with the particle type, but it is not expected to differ for light hadrons which are considered here.

As the number of beam particles was not measured reliably in the experiment, one should consider a relative estimate of the K^+ cross section by comparing K^+ and $\pi^\pm$ multiplicities. For that goal, it is better to rewrite Eq. (6.4) simultaneously for K^+ and for π^+ (or π^-) tracks in a modified way:

$$\frac{d^2\sigma_{(K^+)}}{dpd\theta} = \text{Const}_{K^+} \cdot \frac{1}{\epsilon_{(K^+)det}(p,\theta)} \frac{dN^{det}_{(K^+)}}{dpd\theta}, \quad (6.5)$$

$$\frac{d^2\sigma_{(\pi^+)}}{dpd\theta} = \text{Const}_{\pi^\pm} \cdot \frac{1}{\epsilon_{(\pi^+)det}(p,\theta)} \frac{dN^{det}_{(\pi^+)}}{dpd\theta}, \quad (6.6)$$

$$\frac{d^2\sigma_{(\pi^-)}}{dpd\theta} = \text{Const}_{\pi^\pm} \cdot \frac{1}{\epsilon_{(\pi^-)det}(p,\theta)} \frac{dN^{det}_{(\pi^-)}}{dpd\theta}, \quad (6.7)$$

where an integration over azimuthal angle is performed and the constants Const_{K^+}, $\text{Const}_{\pi^\pm}$ carry all the characteristics of the target material, inefficiencies due to dead time of electronics and trigger conditions. One may derive Const_{π^+} from experimental multiplicities of π^+ comparing them with measured total cross section from another experiment. For that reason, Eqs. (6.5), (6.6) and (6.7) can be integrated over a kinematic region of good detection properties, to obtain

$$\triangle\sigma_{(\kappa)ij} = \text{Const} \cdot \int\limits_{p_{imin}}^{p_{imax}} dp \int\limits_{\theta_{jmin}}^{\theta_{jmax}} d\theta \int\limits_{\phi=0}^{2\pi} \frac{1}{\epsilon_{(\kappa)det}} \cdot \frac{d^3N^{det}_{(\kappa)}}{dpd\theta d\phi} \, d\phi. \quad (6.8)$$

Integrating over azimuthal angle and folding the detection correction with the corresponding counts within each single bin in the histogram, delivers

$$\triangle\sigma_{(\kappa)ij} = \text{Const} \cdot \int\limits_{p_{i_{min}}}^{p_{i_{max}}} \int\limits_{\theta_{j_{min}}}^{\theta_{j_{max}}} \frac{d^2 N_{(\kappa)}}{dpd\theta} \, dpd\theta, \tag{6.9}$$

where $\frac{d^2 N_{(\kappa)}}{dpd\theta}$ is number of particles per bin (i,j) (i.e. already corrected for the detection efficiency) as two-dimensional distribution of momentum and polar angle, see Eq. (6.2). The estimate for $\frac{1}{\epsilon_{(\kappa)det}}$ was provided by the detection corrections $c(p,\theta)$ for each type κ of particles, see Eq. (6.1).

Also, keeping in mind that all dependences are obtained as distributions within certain acceptances as accumulated into histograms with finite binning size in p and θ, one measures always only a fraction of the total cross section

$$\sigma_{(\kappa)}^{frac}(p \in \{p\}, \theta \in \{\theta\}) = \text{Const} \cdot \sum_{i \in \{p\}} \sum_{j \in \{\theta\}} N_{(\kappa)ij} \tag{6.10}$$

for any particle type κ, where the sum runs over bins i, j in the range of acceptance taken into account. The number of particle counts corrected for the detection efficiency per bin is $N_{(\kappa)ij}$. As already mentioned, acceptances $\{p \otimes \theta\}$ are different for different particle types.

To estimate the total cross section one applies an extrapolation procedure to estimate the remaining part of cross section which is not accessible by the experiment. The inclusive differential particle-production cross sections of C(2AGeV)+C interactions can be approximated by Maxwell-Boltzmann like distributions, proven as appropriate parameterization of the energy dependence of the differential cross section for larger collision systems. We apply this parameterization here also to carbon-carbon interactions due to its simplicity. It is also used in the Pluto event generator to generate phase-space distributions for pions and kaons in nucleus-nucleus collisions. Having this tool at our disposal, one can exploit the potential of the numerical simulations to obtain the required extrapolation of $\sigma_{(\kappa)}^{part}(p \in \{p\}, \theta \in \{\theta\})$ to the total cross section $\sigma_{(\kappa)}^{tot}$ considering the ratio

$$\frac{\sigma_{(\kappa)}^{tot}}{\sigma_{(\kappa)}^{part}} = \frac{N^{MCtot}}{N^{MCpart}}. \tag{6.11}$$

Here, N_{MC}^{tot} is the total number of tracks obtained from Monte-Carlo event generator and N_{MC}^{part} is a corresponding number of tracks which were generated in the part of the acceptance, i.e. in the region which is used for detection of this kind of particle in the experiment. The schematic illustration of the extrapolation of measured cross sections $\sigma_{(\kappa)}^{frac}(p \in \{p\}, \theta \in \{\theta\})$ to the total one, σ^{tot}, is illustrated in Fig. 6.6.

6.3.1   Absolute normalization to π^+ count rates

Taking into consideration Eqs. (6.11) and (6.10), where the latter one corresponds to Eq. (6.6), one concludes

$$\sigma_{(\pi^+)}^{tot} = \frac{N_{\pi^+}^{MCtot}}{N_{\pi^+}^{MCpart}} \cdot \text{Const}_{\pi^\pm} \cdot \sum_{i \in \{p\}} \sum_{j \in \{\theta\}} N_{(\pi^+)ij}, \tag{6.12}$$
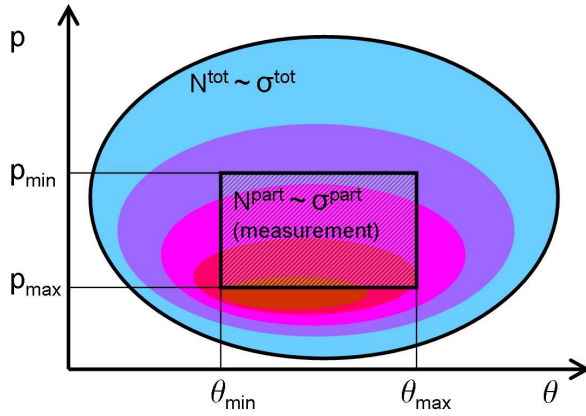
Figure 6.6: Schematic illustration of extrapolating the measured partial cross section to the total cross section. The distribution of tracks is illustrated with color which intensity goes from blue (low density of tracks) to red (high density). The measured region and the total region are surrounded by black border lines.

where the total cross section of π^+ production, $\sigma_{(\pi^+)}^{tot} = (0.69 \pm 0.1)b \cdot (1.106 \pm 0.132)$, can be taken from [Lau00] for the reaction C(1.8AGeV)+C with the corresponding scaling of the beam kinetic energy from 1.8 AGeV to 2.0 AGeV as provided in [Stu01a, Stu01b]. The fraction $N_{\pi^+}^{MCtot}/N_{\pi^+}^{MCpart} = 10^7/1.1188 \cdot 10^6$ was estimated from 10^7 tracks generated with Pluto running with realistic description of the π^+ momentum distribution for this system and energy, according to

$$\frac{d^3\sigma}{dp^3} \propto f e^{-E/T_1} + (1-f) e^{-E/T_2}, \tag{6.13}$$

where $f = C_1/(C_1 + C_2)$, $C_1 = 334 \, b/(GeV^3 \, sr)$, $C_2 = 43.3 \, b/(GeV^3 \, sr)$, $T_1 = 47.7 \, MeV$, $T_1 = 86.9 \, MeV$ and an isotropic thermal source was assumed as reported in [Stu01a]. The radial expansion velocity $\beta_r = 0$ is used. The acceptance region for appropriate detection of π^+ was selected as $200 \, MeV/c < p < 600 \, MeV/c$, $50° < \theta < 82°$. This momentum selection covers the main bulk of pion yields, see Fig. 6.5. In this analysis it might be problematic to take into account pions with higher momenta due to the decrease of their energy loss in matter and difficulty to simulate this effect with high accuracy. Providing that in the region of high momenta the amount of pions is much lower, it is better to focus to low energy pions, which have comparable energy loss to the kaons, which are heavier. The efficiency aspect is of particular importance in the present analysis, where the $\pi^\pm$ yields are used to normalize the K^+ yields. The sum of corresponding tracks measured by experiment in this acceptance region, corrected by the detection efficiency is $\sum_{i\in\{p\}} \sum_{j\in\{\theta\}} N_{(\pi^+)ij} = 1.162 \cdot 10^6$. This allows one to estimate $\text{Const}_{\pi^+} = 7.799 \cdot 10^{-8} \, b$.

6.3.2   Absolute normalization to π^- count rates

The same procedure as presented in section 6.3.1 was applied to π^- tracks in the acceptance region $200 \, MeV/c < p < 600 \, MeV/c$ and corresponding angular acceptance $40° < \theta < 76°$. The obtained fraction is $N_{\pi^-}^{MCtot}/N_{\pi^-}^{MCpart} = 1.0 \cdot 10^7/1.9116 \cdot 10^6$.

The total π^- cross section estimate from KaoS measurement of the reaction C(1.8AGeV) + C after the corresponding scaling to 2.0 AGeV according to [Stu01a, Stu01b] is $\sigma_{(\pi^-)}^{tot} = (0.64 \pm 0.1)b \cdot (1.106 \pm 0.132)$. The sum of tracks measured by experiment in this acceptance region, already corrected by the detection efficiency, is $\sum_{i\in\{p\}} \sum_{j\in\{\theta\}} N_{(\pi^-)ij} = 2.027 \cdot 10^6$. This allows one to estimate $\text{Const}_{\pi^-} = 6.673 \cdot 10^{-8} \, b$.

6.3.3   Estimate of K^+ cross section

The difference in the constants $\mathrm{Const}_{\pi\pm}$ obtained from Eqs. (6.6) and (6.7) lies inside the error propagated from π^+ and π^- cross section measurements. Taking in consideration that $\mathrm{Const}_{K+} \approx \mathrm{Const}_{\pi\pm} = \frac{1}{2}(\mathrm{Const}_{\pi+} + \mathrm{Const}_{\pi-}) = (7.2 \pm 1.1) \cdot 10^{-8}\,\mathrm{b}$ and inserting in Eq. (6.5) one obtains the estimate of K^+ differential cross section. Also, normalized to 4π, the K^+ total cross section estimate is performed as for pions (except the fact that the value of $\mathrm{Const}_{K+} \approx \mathrm{Const}_{\pi\pm}$ has been already estimated from pions) which is

$$\sigma^{tot}_{(K^+)} = \frac{N^{MCtot}_{K^+}}{N^{MCpart}_{K^+}} \cdot \mathrm{Const}_{K\pm} \cdot \sum_{i\in\{p\}} \sum_{j\in\{\theta\}} N_{(K^+)ij}. \tag{6.14}$$

Here, the acceptance region for K^+ detection is taken as $350\,\mathrm{MeV/c} < p < 700\,\mathrm{MeV/c}$, $46° < \theta < 82°$. The corresponding 4π normalization of the detector acceptance $N^{MCtot}_{K^+}/N^{MCpart}_{K^+} = 1.0 \cdot 10^7/0.6225 \cdot 10^6$ can be estimated from Pluto simulation of 10^7 K^+ tracks in assumption of isotropic distribution with inverse slope parameter $T = 78\,\mathrm{MeV}$ and radial expansion velocity $\beta_r = 0$. The sum of K^+ track counts corrected for detection efficiencies $\sum_{i\in\{p\}} \sum_{j\in\{\theta\}} N_{(K^+)ij} = 12178.6$. The total cross section for K^+ production in the C(2AGeV)+C reaction is estimated relative to the pion cross section, i.e. $\sigma^{tot}_{(K^+)} = 14.156\,\mathrm{mb}$, which is still to be corrected for the centrality trigger and for the background contribution for the selected region. After the correction for background contribution of $23.5\,\%$ the result is $\sigma^{tot}_{(K^+)} = (10.8 \pm 2.0)\,\mathrm{mb}$ where the error of background contribution of 10% is taken into account. Correcting for the multiplicity trigger condition by $1/1.49$ and electron trigger condition by $1/1.005$, one gets

$$\sigma^{isot}_{K^+} = (7.2 \pm 1.3)\,\mathrm{mb}, \tag{6.15}$$

where the error is propagated from errors of pion cross sections and the error of determination of background contribution is also taken into account. The possible errors related to the normalization minimum bias from our LVL1- and LVL2-triggered sample are not included here. The influence of the HADES trigger conditions as well as the estimate of possible systematic errors are discussed in the following subsections.

6.3.4   Influence of multiplicity trigger on K^+ multiplicity

As mentioned in the introduction of this chapter, the charged particle multiplicity trigger condition (LVL1 trigger) was applied during the experiment. The centrality of the event is characterized by the impact parameter of the collision. The multiplicity of charged pions is directly proportional to the number of participants, A_{part} [Sen01], i.e. described by $dM_K/d\Omega_{c.m.} \propto A_{part}$. The centrality dependence of the K^+ multiplicity was measured for Ni + Ni collisions [Bar97], i.e. $dM_K/d\Omega_{c.m.} \propto (A_{part})^\alpha$ with $\alpha = (1.70 \pm 0.25)$ at 1.0 GeV/nucleon and $\alpha = (1.65 \pm 0.15)$ at 1.8 GeV/nucleon. The value of $\alpha = (1.64 \pm 0.20)$ for K^+ at 2.0 GeV/nucleon can be established after linear extrapolation of the two measurements mentioned above. For lighter systems this dependence was not measured, therefore this extrapolation of Ni + Ni data is used here for C + C system, i.e.

$$\alpha_\pi = 1, \quad \alpha_{K+} = 1.64 \pm 0.20. \tag{6.16}$$

The maximum impact parameter for symmetric system C + C is $b_{max} = 2 \cdot R_C \approx 2 \cdot 1.25 A^{1/3}$ fm $= 5.7$ fm, where R_C is the radius of carbon nucleus ($A = 12$). The mean impact parameter is estimated as $\langle b \rangle = \frac{2}{3} b_{max} = 3.8$ fm for minimum-bias events. As described above, the measurements were done with the trigger on events with multiplicity ≥ 4 charged particles (85 % of events) and multiplicity ≥ 2 (15 % of events) within the acceptance of HADES, which is not a minimum bias condition any longer. The impact-parameter dependence on trigger condition for the case of "more or equal 2" and "more or equal 4" charged particles in geometrical acceptance of the HADES experiment has to be studied to correct the measured K^+ cross section for the trigger conditions. The influence of trigger conditions on the inclusive K^+ production can be investigated, e.g. with UrQMD simulation in a first approximation. In Fig. 6.7 one can see the impact-parameter distribution for events with conditions that some of the charged particle tracks were in the acceptance angles of HADES spectrometer $22° < \theta < 86°$, more specifically one of the following requirements were satisfied: **minimum bias:** no conditions applied; **multiplicity trigger 2:** at least two charged particle were counted in the acceptance; **multiplicity trigger 4:** at least four charged particle were counted in the acceptance.

The multiplicity trigger may act non-uniformly for different particle types. Therefore one has to investigate its influence on $\pi^\pm$ and K^+ separately and use the ratio[4]

$$\frac{M^{trig}}{M^{min.b.}} = \left(\frac{A^{trig}_{part}}{A^{min.b.}_{part}} \right)^\alpha , \qquad (6.17)$$

where M^{trig} is the particle multiplicity per event in case of applied trigger multiplicity and $M^{min.b.}$ is the multiplicity for the case of minimum bias. A^{trig}_{part} and $A^{min.b.}_{part}$ are numbers of participants for the case of applied trigger multiplicity and for the minimal bias case, respectively. The parameter α was defined in Eq. (6.16). One can see that the K^+ multiplicity grows faster with number of participants than the $\pi^\pm$ multiplicity by a factor of $(A^{trig}_{part}/A^{min.b.}_{part})^{\alpha_{K^+} - \alpha_\pi}$. The values of A^{trig}_{part} and $A^{min.b.}_{part}$ are estimated from the geometrical model of interpenetrating solid spheres, see Appendix B.

Considering two situations, one with minimum bias and the second one with applied trigger multiplicity for events having at least one pion or at least one K^+ in the acceptance, one can estimate the mean multiplicity of such events. This was done with the help of UrQMD simulations of 10^7 C(2AGeV)+C events presented in Fig. 6.7.
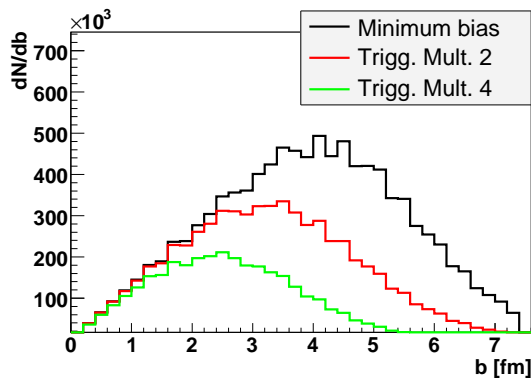

Figure 6.7: The impact-parameter distribution for minimum bias events (black histogram) and events produced in case of multiplicity trigger conditions of at least two and at least four charged particles in the geometrical acceptance of HADES (red and green histograms) according to UrQMD simulation.

The corresponding values are summarized in table 6.1. The influence of the multiplicity

---

[4]due to the use of K^+ to $\pi^\pm$ relative normalization

Minimum Bias events	Multiplicity Trigger events		
	$<b_{trig2}>$=3.27 fm		15%
	$<b_{trig4}>$=2.60 fm		85%
$<b_{min.b.}>$=3.89 fm	$<b_{trig}>$=2.70 fm		100%
$<A_{part}>_{min.b.}$=5.78	$<A_{part}>_{trig}$=10.78		

Enhancement compared to minimum bias

$\pi^{\pm}$ track	K^+ track
$\dfrac{M_{trig}}{M_{min.b.}} = \left(\dfrac{<A_{part}>_{trig}}{<A_{part}>_{min.b.}}\right)^{\alpha}$	
$\left(\frac{10.78}{5.78}\right)^1 = 1.87$	$\left(\frac{10.78}{5.78}\right)^{1.64} = 2.78$

$$\frac{\left(\frac{M_{trig}}{M_{min.b.}}\right)_{K^+}}{\left(\frac{M_{trig}}{M_{min.b.}}\right)_{\pi}} = 1.49$$

Table 6.1: The influence of the multiplicity trigger to events containing $\pi^{\pm}$ and K^+ tracks in the acceptance of HADES spectrometer. The notations are: b – impact parameter, A_{part} – number of participants. Indices $trig2$, $trig4$ and $trigg$ stand for events with trigger multiplicities 2, 4 and for the resulting overall trigger, correspondingly. The mean values of impact parameters are estimated from Fig. 6.7.

trigger LVL1 increases the multiplicities (with respect to minimum bias events) of $\pi^{\pm}$ and K^+ mesons by factors 1.87 and 2.78, respectively and results in a relative abundance of K^+ compared to $\pi^{\pm}$ of factor 1.49 which has to be taken into account in addition to background subtraction.

6.3.5   Influence of electron trigger on π^+ and K^+ multiplicity

In addition to the common LVL1 requirement a special electron triggering was applied (LVL2 trigger) for 46.2 % of all used events, i.e. LVL1 $\bigcup$ LVL2. The investigation of its influence on hadron tracks was done with real data using measured π^+ and K^+ multiplicities. The ratio between LVL1 and LVL2 trigger conditions resulting into π^+ and K^+ multiplicities are presented in table 6.2. The observed difference of few percents is to be taken into account for 46.2 % of events, which results in a ratio of $M_{K^+}/M_{\pi^+} = 1.005$ due to admixture of LVL2 events (normalized to sum of LVL1 and LVL2 events). That means, we overestimate the K^+ cross section only by 1 %; which is also a correction taken into account.

$\dfrac{\left(\dfrac{N_{\pi^+}}{N_{ev}}\right)_{LVL2}}{\left(\dfrac{N_{\pi^+}}{N_{ev}}\right)_{LVL1}}$	$\dfrac{\left(\dfrac{N_{K^+}}{N_{ev}}\right)_{LVL2}}{\left(\dfrac{N_{K^+}}{N_{ev}}\right)_{LVL1}}$
0.899 ± 0.005	0.91 ± 0.03

Table 6.2: Investigation of the influence of the LVL2 trigger on the detected π^+ and K^+ tracks. The acceptance region for π^+ tracks was $300 < p < 1000\,\mathrm{MeV/c}$, $46° < \theta < 82°$. The K^+ tracks are taken from the selection areas described below (including both TOF and TOFINO regions).

6.3.6   Estimate of systematical errors

Considering several sources of systematical errors in the current analysis of the HADES experiment one may expect influence of a) errors corresponding to alignment of the detectors, b) errors in momentum reconstruction due to the energy loss in matter along the track path (see Appendix A), c) errors related to knowledge about the efficiency of individual modules of the detector, d) errors arising from the correction of our data because of trigger conditions.

Systematic errors of class a) were not investigated due to the difficulty of misalignment determination, but should be of comparable size as the errors of class b). Errors of class b) are minor due to the binning selection. The momentum binning selected for the efficiency correction matrix is $50\,\mathrm{MeV/c}$ for K^+ tracks and $25\,\mathrm{MeV/c}$ for pions. It is well above the momentum resolution and systematical shifts (see Fig. A.2) for charged kaon and pion tracks provided by Runge-Kutta tracking. During this analysis it was found that the main contribution to systematic errors stems from classes c) (due to difficulties to describe in simulation the efficiency of MDC detectors for minimum ionizing tracks which might be essential for pions) and d) (due to assumptions in subsection 6.3.4).

In order to estimate the errors of class c) the selected momentum region of charged pions, $200 < p < 600\,\mathrm{MeV/c}$, was divided into two intervals with an equal number of tracks in each (see Fig. 6.8). The above described method of K^+ cross section normalization (see sections 6.3.1 – 6.3.3) was repeated with pions taken from these two subintervals. The corresponding two values of the cross section σ_{K^+} obtained by normalizing to pions taken from momentum regions A and B were considered as minimum and maximum variation of σ_{K^+}. The variation reflects the systematic error connected to the selection of the momentum region of pions used for normalization of the K^+ cross section.

These estimates lead to a systematic variation of the cross section within the range of $6.85\,\mathrm{mb} < \sigma_{K^+} < 8.07\,\mathrm{mb}$, while the cross section estimate from the region A+B was $\sigma_{K^+} = 7.24\,\mathrm{mb}$.

The additional systematic error of class d) due to the minimum bias normalization of the data is about 18%, see Eqs. (6.16), (6.17) and table 6.1.

The errors of classes c) and d) are not correlated. Therefore, the result[5] (cf. Eq. (6.15)

---

[5] The uncertainty of the Ni+Ni data extrapolation to C+C data with respect to K^+ multiplicity dependence as the function of number of participants can not be included here.
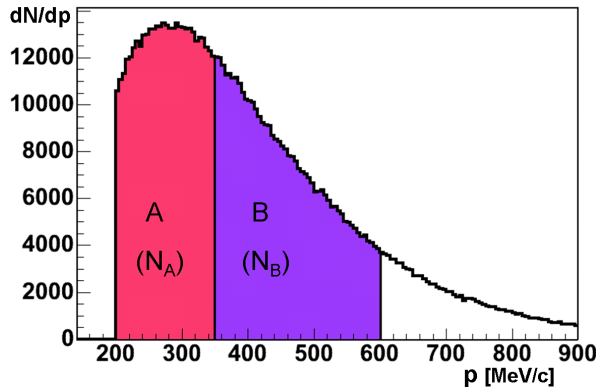
Figure 6.8: The selection of momentum intervals of pions used for the determination of systematical errors related to the absolute normalization of K^+ cross section. The areas A and B are selected to satisfy $N_A \approx N_B$.

assuming isotropic emission) can be written as

$$\sigma_{K^+}^{isotr} = (7.2 \pm 1.3(stat)_{-1.4}^{+1.5}(syst)) \text{ mb}. \tag{6.18}$$

This result implies the extrapolation over full phase space assuming an isotropic emission of K^+ mesons in center of mass system. However, the corresponding results from the KaoS collaboration [Lau99, Lau00] are extrapolated assuming an anisotropic emission. The reason for that is the significant anisotropy in the [Lau00] observed in C(1.8AGeV) + C system as a growth of the total cross section for K^+ meson production (when exploiting the isotropic emission assumption) with polar angle in the laboratory system. Applying here the same parameterization of the anisotropic emission to our data as measured for C(1.8AGeV) + C system [Lau00],

$$d^3\sigma/dp^3 \sim (1 + a_2 cos^2\theta_{c.m.}) \ e^{-E/T} \tag{6.19}$$

with anisotropy $a_2 = 0.54 \pm 0.25$, the final result is obtained as

$$\sigma_{K^+}^{anisotr} = (5.9 \pm 1.1(stat)_{-1.1}^{+1.2}(syst)) \text{ mb}. \tag{6.20}$$

Within the error bars, our total K^+ cross section is fully in agreement with that reported by the KaoS collaboration [Lau99]. The obtained reduction of $\sigma_{K^+}^{tot}$ assuming anisotropy as compared to Eq. (6.18) for the isotropic case, is a factor of 1.22. A systematic error of 7% has to be added in Eq. (6.20) due to the error of the anisotropy parameter a_2 used in Eq. (6.19). Concluding, one may invert this result to state that good agreement of this measurement with the KaoS data supports the assumption of Eqs. (6.16) and (6.17) used here.

The relative normalization scheme discussed in this chapter is applied for the absolute normalization of differential spectra of K^+ mesons obtained in chapter 7.

7 Differential spectra of K^+ mesons

In this chapter, the momentum distribution of K^+ mesons measured in the final-state of C + C collisions at 2 AGeV is presented. The selection criteria, efficiency corrections and the yield normalization of K^+ mesons already discussed in chapters 5 and 6 were applied here too. The amount of detected kaons offers us the possibility of investigating differential spectra normalized to the total cross section.

7.1 Kinematics

Defining the z-axis along the beam, the energy and momentum of a particle can be written as

$$E = m_t \cosh y, \quad p_x, \quad p_y, \quad p_z = m_t \sinh y, \tag{7.1}$$

where m_t is the transverse mass $m_t^2 = m_0^2 + p_t^2$ and $p_t^2 = p_x^2 + p_y^2$ is the transversal momentum, m_0 is the rest mass of the particle; the rapidity y is defined by

$$y = \frac{1}{2} \, ln \left(\frac{E + p_z}{E - p_z} \right) = \tanh^{-1}(\beta_z), \tag{7.2}$$

where for the longitudinal velocity $\beta_z = p_z/E$ is taken into account. The invariant cross section for inclusive reactions can be written as [Par98]

$$E \frac{d^3\sigma}{dp^3} = \frac{d^3\sigma}{d\phi \, dy \, p_t \, dp_t}, \tag{7.3}$$

where ϕ is the azimuthal angle. The energy spectra of systems of particles close to kinetic equilibrium are described by thermodynamic models (see e.g. [Hag68]), which anticipates that the center of mass (c.m.) momentum spectra are described by a temperature (slope) parameter T which characterizes a Maxwell-Boltzmann distribution

$$\frac{d^3\sigma}{dp^3} = const \cdot e^{-\frac{E}{T}}, \tag{7.4}$$

where p and E are momentum and energy in c.m. reference frame (see e.g. [Bro84]). Averaging Eq. (7.3) over azimuthal angle and comparing the result with Eq. (7.4) one can conclude that

$$\frac{d^2\sigma}{2\pi \, dy \, p_t \, dp_t} = const \cdot E \cdot e^{-\frac{E}{T}}, \tag{7.5}$$

where it is important to realize that (due to invariant cross section notation) the left part is invariant with respect to Lorentz transformations along the z-axis, while the right part is valid only in the c.m. frame. For the subsequent analysis it is useful to take into account the identity $p_t dp_t = m_t dm_t$ and the left part of Eqs. (7.1). Thus Eq. (7.6) can be rewritten accordingly

$$\frac{1}{m_t^2}\frac{d^2\sigma}{dy\,dm_t} = C \cdot \cosh y \cdot e^{-\frac{m_t \cosh y}{T}}, \tag{7.6}$$

where m_t is invariant with respect to a Lorentz transformation of the reference frame along the z-axis, and the constant is redefined by a factor 2π. It should be realized that the right part of Eq. (7.6) corresponds to c.m. reference frame (because of Eq. (7.4)). This form is convenient for practical purposes because the shape of rapidity is invariant with respect to some Lorentz transformations. Namely, the boost in the z direction to a reference frame with velocity β_z corresponds to the rapidity transformation from $y \longrightarrow y - \tanh^{-1}\beta_z$. Hence, the rapidity behaves as an additive variable with respect to the Lorentz boost, i.e. $(y)_{lab} = (y)_{cm} + (y_{cm})_{lab}$, where $(y)_{lab}$ is rapidity in laboratory reference frame, $(y)_{cm}$ is rapidity in c.m. reference frame and $(y_{cm})_{lab}$ is the c.m. rapidity with respect to the laboratory system.

For convenience, in comparisons of experimental data obtained with different projectile energies the so-called normalized rapidity is used. It is defined as the ratio in the c.m. reference frame of the rapidity to the projectile rapidity

$$y_0 = \left(\frac{y}{y_{proj}}\right)_{cm}. \tag{7.7}$$

Here y_{proj} is the rapidity of projectile (beam) particle. Subtracting the rapidity of c.m. system (y_{cm} which is also called midrapidity) with respect to the laboratory reference frame, the right part of Eq. (7.7) can be rewritten also in the laboratory system

$$y_0 = \left(\frac{y - y_{cm}}{y_{proj} - y_{cm}}\right)_{lab}. \tag{7.8}$$

For mass-symmetric systems ($A_{targ} = A_{proj}$) one may take into account also that $y_{proj} = 2y_{cm}$ in the laboratory frame, which allows one to rewrite Eqs. (7.7) and (7.8) in a simpler form

$$y_0 = \left(\frac{y}{y_{cm}} - 1\right)_{lab}. \tag{7.9}$$

Therefore, for symmetric systems, the normalized rapidities of -1, $+1$ and 0 corresponds to target, projectile, and center-of-mass reference frames, respectively.

Considering these transformations of rapidity one can rewrite Eq. (7.6) in variables y_0 and m_t as follows

$$\frac{1}{m_t^2}\frac{d^2\sigma}{dy_0\,dm_t} = C \cdot y_{cm} \cdot \cosh(y_0 y_{cm}) \cdot e^{-\frac{m_t \cosh(y_0 y_{cm})}{T}}. \tag{7.10}$$

7.2 Transverse-mass spectra and rapidity density distribution

The efficiency corrected double-differential yield of tracks identified as K^+ mesons is presented in Fig. 7.1 as a function of p_t and normalized rapidity y_0. The calculations of p_t and

y_0 are based on Eqs. (7.1) and (7.9), where K^+ meson mass $m_0 = 493.7\,\mathrm{MeV/c^2}$ and the midrapidity value of $y_{cm} = 0.904$ for reaction $\mathrm{C(2\,AGeV)+C}$ are taken into account. In
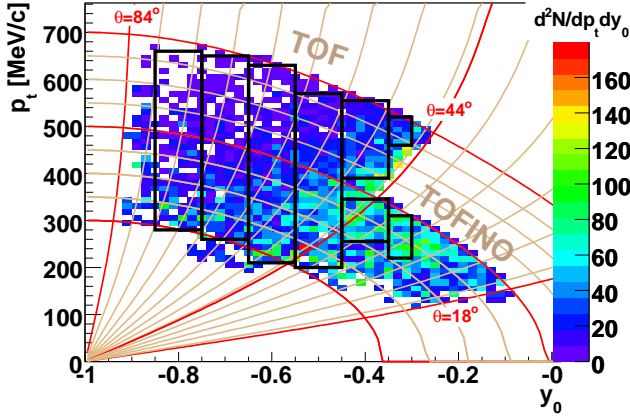
Figure 7.1: The double-differential yield $d^2N/dp_t dy_0$ of K^+ mesons vs. normalized rapidity and transverse momentum corrected for the detection efficiency. The acceptance grid in laboratory momentum p and polar angle θ is indicated by curves. An absolute normalization is not performed in this stage.

addition, isocurves of constant laboratory momenta and polar angles are drawn, and the regions covered by TOF and TOFINO detectors are indicated. The black rectangular areas represent the chosen binning along the rapidity which is used to generate transverse-mass spectra. Two rapidity bins (close to midrapidity) are composed from TOF and TOFINO regions and split into two subintervals along p_t in order to handle the empty region in between. The edge regions of each area are excluded to avoid systematical distortions connected with possible deviations between the measured and simulated data at the detector borders. The $d^2N/dm_t dy_0$ distributions weighted with the factor $1/m_t^2$ are shown in Fig. 7.2 for each of six y_0 bins. As indicated in Eqs. (7.6) and (7.10), in such a representation ($\frac{1}{m_t^2} \cdot \frac{d^2N}{dm_t dy_0}$ vs. $m_t - m_0$), the distribution of particles emitted isotropically from a thermally equilibrated source is described by the exponential function of a Maxwell-Boltzmann like distribution

$$\frac{1}{m_t^2} \cdot \frac{d^2\sigma}{dm_t dy_0} = A(y_0) \cdot e^{-\frac{m_t - m_0}{T_B}}, \qquad (7.11)$$

where for each bin of normalized rapidity the normalization factor

$$A(y_0) = C \cdot y_{cm} \cdot \cosh(y_0 y_{cm}) \qquad (7.12)$$

and the so-called apparent temperature

$$T_B = T_B(y_0) = T/\cosh(y_0 y_{cm}) \qquad (7.13)$$

for the selected y_0 region are introduced. Both parameters, $A(y_0)$ and T_B, are derived from fits with the exponential function (7.11) for each of six intervals in y_0. The fits are performed within limited regions of m_t depicted with filled symbols. Lower regions of measured m_t spectra are excluded from fits because there is a clear indication of a discrepancy between the efficiency corrected yields and the expectation which can be explained by lower detection efficiency at low momentum in experiment compared to the simulation used for efficiency correction, i.e. an efficiency correction is not performed reliably there.

In the representation (with vertical logarithmic scale) chosen for Fig. 7.2 the meaning of T_B is an inverse-slope parameter for each y_0 distribution. The $T_B(y_0)$ distribution derived
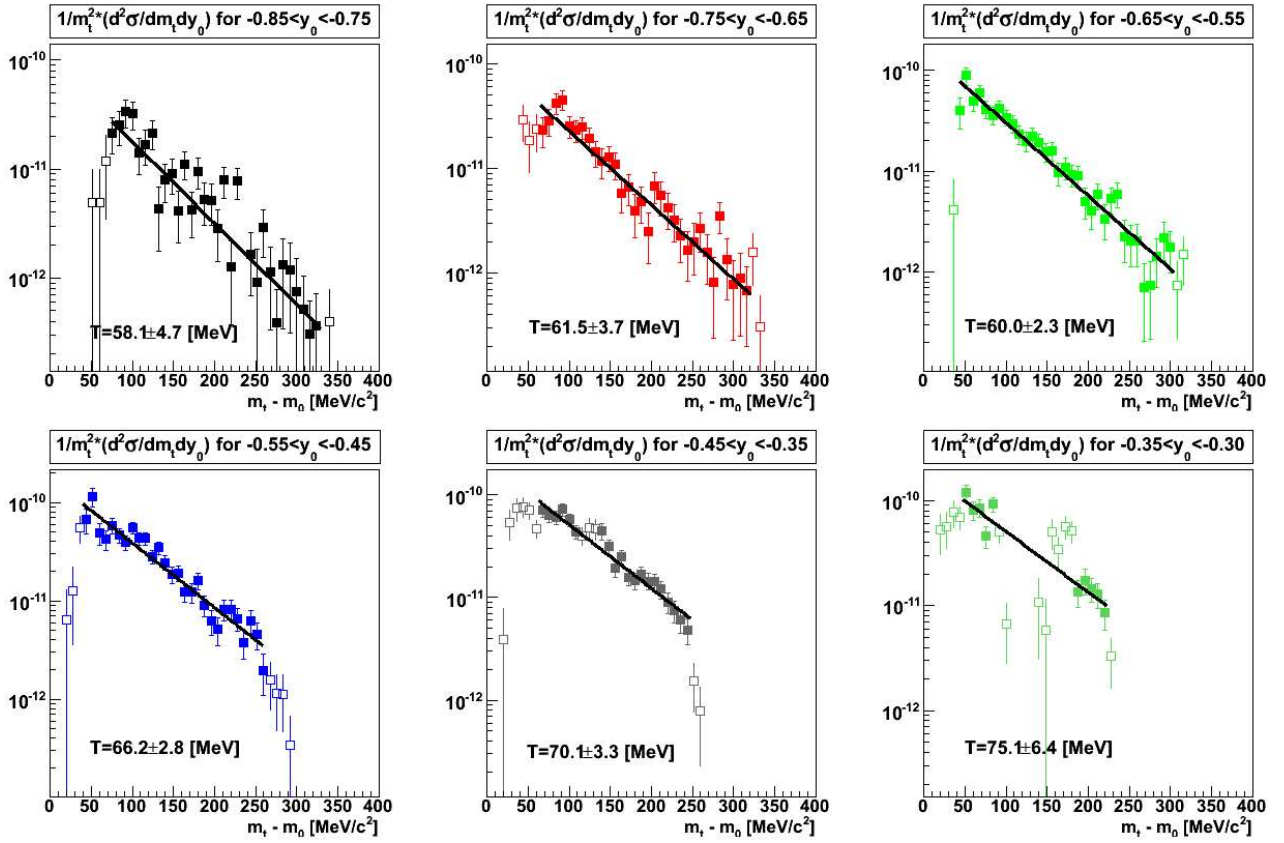
Figure 7.2: $\frac{1}{m_t^2} \cdot \frac{d^2N}{dm_t dy_0}$ spectra for different rapidity regions. The units for vertical axis are $b\,(MeV/c^2)^{-3}$, i.e. already normalized on the total cross section. The data (symbols) are fitted by Eq. (7.11). The selection of the m_t regions (indicated with filled symbols) used for the fits (solid lines) corresponds to p_t limits (see the rectangular selection boxes) in Fig. 7.1. The empty symbols are excluded in the fits (see text for details).
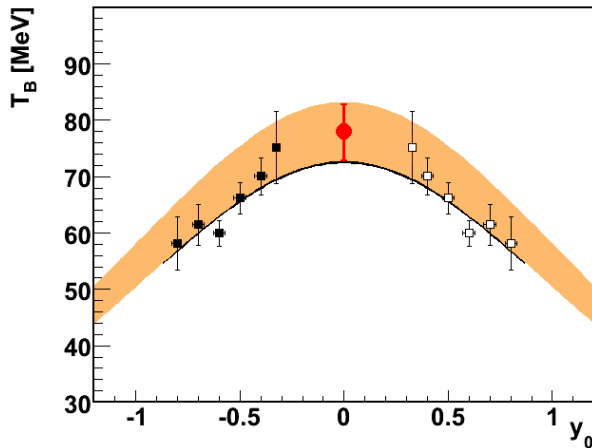

Figure 7.3: The inverse slope parameters T_B as a function of normalized rapidity y_0. The points estimated from measurements (full black symbols) are reflected with respect to mid-rapidity (empty symbols). The value estimated from the KaoS experiment [Lau99] is presented as red full circle at midrapidity. The orange band indicates an extrapolation of the KaoS measurement (including the variations within the error bar) outside the midrapidity region based on the assumption of thermally equilibrated K^+ source, Eq. (7.13). The solid curve is the fit by Eq. (7.13) of full black symbols.

from these fits is presented in Fig. 7.3. The $T_B(y_0)$ distribution was fitted in turn with

Eq. (7.13), $T = T_B \cdot \cosh(y_0 y_{cm})$, to estimate the characteristic momentum scale (temperature) of K^+ produced in this C(2 AGeV)+C reactions under the assumption of thermal equilibrium. As the fit result (black curve in Fig 7.3) one estimates an inverse slope parameter $T = (73 \pm 4)$ MeV at midrapidity point, where the error is combined from uncertainty of the fit (one standard deviation) and the systematic error (see next section). One can conclude that the distribution Eq. (7.13) is in good agreement with rapidity dependent slope parameters derived from m_t spectra. This supports the applicability of thermal source distributions for parameterizations the momentum distribution of K^+ mesons in this case. Whether thermal equilibrium is really reached in such relatively small systems of carbon-carbon at this energy region is an issue under debate. FOPI data of Ni + Ni for K^+ meson [Bes97] and for proton [Hon98b] production indicate that thermal equilibrium is not fully reached, which reveals in narrower width of the T_B vs. y_0 distribution as compared to Eq. (7.13).

The corresponding estimate of inverse-slope parameter with its error bar at mid-rapidity obtained by the KaoS experiment [Lau99] is shown in the same figure as red full circle for comparison. This result is extrapolated here for the sake of a comparison to our data by employing Eq. (7.13) and taking a temperature parameter at midrapidity as $T = (78 \pm 5)$ MeV (indicated with orange band).

The measured $T_B(y_0)$ distribution is consistent with the KaoS result, although within the assumption of thermal equilibrium distributions, our temperature estimate is systematically somewhat lower (within the errors) as compared to the KaoS one.

In high-energy heavy-ion collisions, the longitudinal "temperature" distribution is not described by a thermal distribution function, see review [Sen99]. One may argue what also for medium energies at small systems Eq. (7.13) is not appropriate. To quantify the deviation from Eq. (7.13) an ad hoc hypothesis is considered,

$$T_B(y_0) = T_k / \cosh(k \cdot y_0 y_{cm}) \tag{7.14}$$

and a fit of data is performed. The obtained result with Eq. (7.14) is $T_k = (76 \pm 6)$ MeV and $k = 1.16 \pm 0.21$, the errors are from the fit. The common fit of our and the KaoS data with the same formula (7.14) results in $T_{k*} = (76 \pm 4)$ MeV and $k_* = 1.19 \pm 0.21$, see Fig. 7.4. The observed deviation of k from 1 may serve as measure of the failure of the pure thermal distribution Eq. (7.13) to describe our data, i.e. about 20% in both cases. In first approximation, this allows one to continue with the analysis according to the framework of thermal model.

7.2.1   Rapidity density distribution

Besides the transverse momentum distribution in selected rapidity bins, also the rapidity density is of interest for characterizing the phase space distribution of K^+ mesons. To obtain the rapidity distribution one has to perform an integration of our transverse momentum spectra.

The K^+ rapidity-density distribution $d\sigma/dy_0$ presented in Fig. 7.5 was obtained by an integration over the full m_t range of the fitted distributions Eq. (7.11), i.e. extrapolating to non-measured regions at low m_t and at high m_t

$$\frac{d\sigma}{dy_0} = \int\limits_{m_t = m_0}^{\infty} \frac{d^2\sigma}{dm_t dy_0}\, dm_t. \tag{7.15}$$
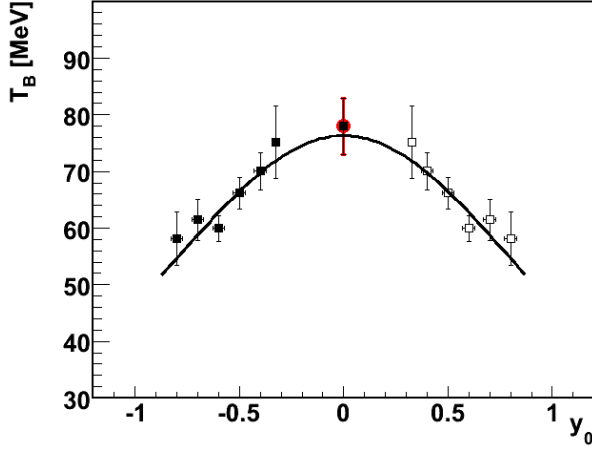
Figure 7.4: The same as in Fig. 7.3 but the fit is done according to Eq. (7.14) common for the HADES and the KaoS data. The points marked with black full symbols were used for the fit. The KaoS point is at $y_0 = 0$ is highlighted in red. The resulting parameters are $T_{k*} = (76 \pm 4)$ MeV and $k_* = 1.19 \pm 0.21$, the errors are from the fit.

The integration (see also [Mer04]) is done individually for each y_0 slice taking into account parameters $A(y_0)$ and $T_B(y_0)$ derived from the corresponding fit

$$\frac{d\sigma}{dy_0} = A(y_0) \int\limits_{m_t = m_0}^{\infty} m_t^2 \, e^{-\frac{m_t - m_0}{T_B}} \, dm_t = A(y_0) \left[m_0^2 T_B(y_0) + 2m_0 T_B^2(y_0) + 2T_B^3(y_0) \right], \quad (7.16)$$

where m_0 is the K^+ meson mass, T_B and $A(y_0)$ are extracted from the fits above. The presented here values $d\sigma/dy_0$ are calculated in the middle of the each y_0 slice.
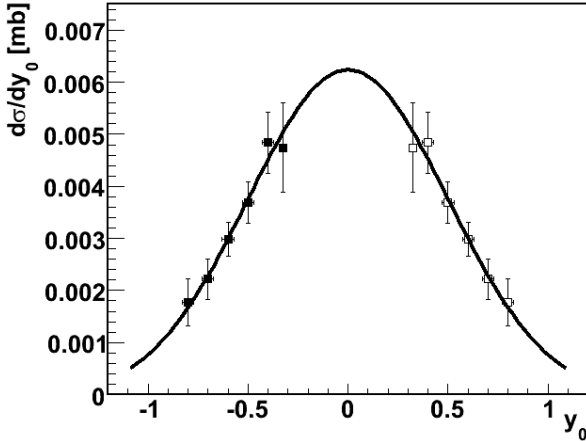
Figure 7.5: The rapidity-density distribution of K^+ mesons in C(2 AGeV)+C. The points obtained from measurements via Eq. (7.16) are shown as filled symbols, while empty symbols represent the reflection with respect to midrapidity. The distribution was fitted according to the isotropic thermal model (black curve) Eq. (7.17), resulting in the temperature parameter $T_\| = (110 \pm 30)$ MeV, with the error derived from the fit.

Taking into account Eqs. (7.12), (7.13) and (7.5) the $d\sigma/dy_0$ distribution can be fitted with

$$\frac{d\sigma}{dy_0} = C \cdot T^3 \cdot \left[\left(\frac{m_0}{T} \right)^2 + \frac{2m_0}{T \cosh(y_0 y_{cm})} + \frac{2}{(\cosh(y_0 y_{cm}))^2} \right] \cdot e^{-m_0 \cosh(y_0 y_{cm})/T}. \quad (7.17)$$

From this fit one can estimate the shape of the distribution, and the integral provides an independent estimate of the total cross section. We obtain $\sigma_{K+} = 7.7$ mb. This cross section is in good agreement with the one (see Eq. (6.18)) determined in chapter 6 and it represents another approach to a 4π normalization based on measured differential yields

extrapolation under assumption of an isotropic K^+ emission, see Eqs. (7.4), (7.11) and (7.15). Since transversal characteristics are integrated in this approach, the obtained value of temperature parameter has the meaning of longitudinal temperature, $T_{||}$, of the K^+ meson source. The value of the fit by Eq. (7.17) results in $T_{||} = (110 \pm 30)\,\text{MeV}$. Comparing this result with the one obtained from the T_B fit one concludes that the measured system is not isotropic, namely there is an indication for an longitudinal elongation. This might be related to some transparency of small systems in the collision direction.

In case when the anisotropic K^+ source is considered as proposed by the KaoS experiment with $a_2 = 0.54$ (see subsection 6.3.6), the fit procedure of the experimental data by the Eq. (7.17) with an isotropic assumption is not providing the exact estimate of the temperature parameter. A direct way would be to provide the anisotropy term as the additional multiplier $(1 + a_2 \cos^2 \theta_{c.m.})$ into Eq. 7.4; i.e. the integration of Eq. 7.15 would be more complicated[1]. Another approach is to keep Eq. (7.17) but rather apply the dedicated correction
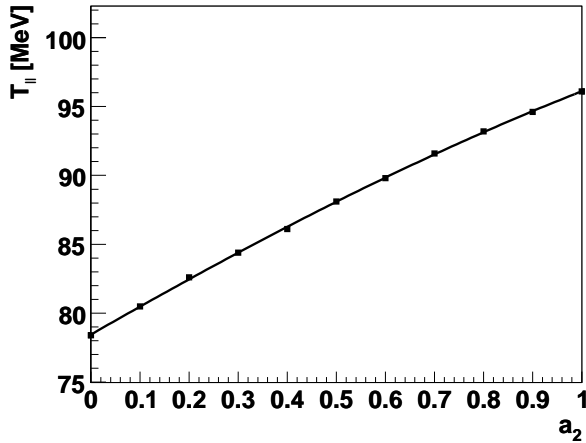
Figure 7.6: The estimates of $T_{||}$ for the set of a_2 parameters (indicated with black symbols). The curve represents an interpolation. The same fit procedure as in Fig. 7.5 was applied to K^+ distributions generated with Pluto assuming different values of anisotropy parameter a_2. Other parameters ($E_{kin} = 2\,\text{AGeV}$, $T = 78\,\text{MeV}$, $\beta_r = 0$) were kept constant. The distribution with anisotropy parameter $a_2 = 0.54$ fitted by Eq. (7.17) overestimates temperature parameter by $11\,\text{MeV}$ which has to be taken into account.

on the arising deviation which can be estimated from corresponding numerical simulations. The correction for the fit performed assuming an isotropic K^+ distribution which is applied to the simulation of K^+ mesons with certain parameter of anisotropy. The corresponding correction can be estimated from Fig. 7.6, where Pluto simulations of K^+ production at $2\,AGeV$ with $T = 78\,\text{MeV}$, $\beta_r = 0$ and different values of anisotropy parameter a_2 were fitted according to Eq. (7.17), exactly with the same conditions as the fit of the analysis of the experimental data presented above. Taking into account the deviation of the fit from the actual value $T = 78\,\text{MeV}$ for the anisotropy parameter, $a_2 = 0.54$, the corrected value of longitudinal temperature would be $(110 - 11 = 99)\,\text{MeV}$. Therefore the longitudinal temperature corrected for the anisotropy is $T_{||}^{(a_2=0.54)} = (99 \pm 30)\,\text{MeV}$.

The systematical errors in the $d\sigma/dy_0$ distribution are mainly coming from the extrapolation of distributions in Fig. 7.2 into non-measured regions.

The presented results are collected from the currently accessed normalized rapidity region of $-0.80 < y_0 < -0.32$. One observes that for the used setup at small polar angles, the time-of-flight detector has obvious limitations to access the midrapidity region due to insufficient momentum range for low-background registration of K^+ mesons. This calls for further improvements. The planned upgrade of TOFINO detector, i.e. its substitution by Resistive

---

[1]Here one has to take into account that $\theta_{c.m.}$ is a function of m_t and y_0.

Plate Chambers (RPC) with characteristic time resolution of 100 *ps* (compare with currently achieved resolutions of time-of-flight detectors in section 2.4), will increase the acceptance of K^+ mesons at midrapidity due to higher momentum range with sufficient mass resolution by a factor of two, making it comparable to the TOF region, see also Fig. 7.1. After such an upgrade one can expect that K^+ measurements with HADES can be extended up to rapidities of $y_0 < -0.15$ with sufficient m_t or momentum dynamic range for improved slope parameter determination.

7.3   Estimate of systematic errors

The systematic errors do not represent the dominant source of errors due to the low number of registered K^+ tracks. A non-negligible source of systematic errors is coming from the difficulty to establish strict borders of the $d^2N/dp_t dy_0$ distribution acceptable for subsequent fits, especially in p_t direction of the distribution. The investigation of the difference between the shapes of distributions (7.11) obtained from experimental data and from UrQMD simulation indicates a possible discrepancy up to the level of 40 MeV/c uncertainty in p_t, which is observed by the drop of the logarithmic shape distribution mainly in the low p_t region (the left side of spectra according to Eq. (7.11), see Fig. 7.2).

Therefore, this effect was investigated with respect to the systematic errors coming from uncertainties of the acceptance description by the simulation. The effect can be studied systematically by varying the area of included fit points from the complete distribution (see Fig. 7.1) so that *a)* either low transverse or *b)* high transverse momentum acceptance is reduced compared to the one presented in Fig. 7.2. These two reference regions of selection are presented in Figs. 7.7 and 7.8.
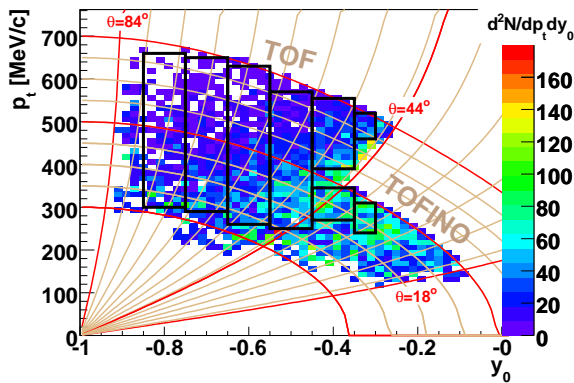
Figure 7.7: The same as Fig. 7.1 but low-p_t acceptance area is reduced for subsequent fits.
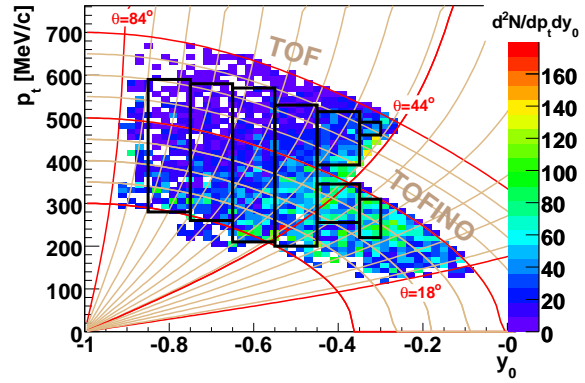
Figure 7.8: The same as Fig. 7.1, but the high-p_t acceptance area is reduced for subsequent fits.

The same estimates as in section 7.2 were performed. The results for T_B vs. y_0 corresponding to an acceptance reduction at low and high p_t regions are depicted in Fig. 7.9 by green and blue colors, respectively. The result from Fig. 7.3 is overlaid on top. The systematics due to acceptance reduction reveals a general trend of T_B distribution. Fits performed according to Eq. (7.13) give $T = (70 \pm 1.7)$ MeV in case *a)* and $T = (77.3 \pm 2.1)$ MeV in case

b) and are drawn as green and blue curves, respectively. The corresponding systematic deviation at midrapidity is about $2\,\text{MeV}$. Therefore, under the assumption of the applicability of thermal equilibrium distributions, the resulting estimate of the temperature parameter is $T = (73 \pm 4)\,\text{MeV}$.
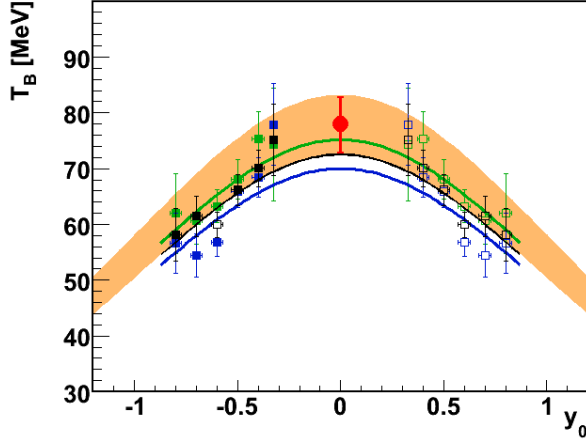
Figure 7.9: The inverse slope parameters T_B as a function of normalized rapidity y_0 for three cases of p_t acceptance selection. The normal one is shown as black symbols (see Fig. 7.3), while green points are for reduced acceptance area at low p_t (see Fig. 7.7) and blue points are for reduced acceptance area at high p_t (see Fig. 7.8). Points extrapolated from measurements are shown as filled symbols, while empty symbols represent the reflection with respect to midrapidity. The result of the KaoS measurement [Lau99] is shown as red point. See text for details.

The corresponding dN/dy_0 spectra superimposed with corresponding fits by Eq. (7.17) are presented in Fig. 7.9, where the color notation for the KaoS result including the coresponding error band as in Fig. 7.3 is used.
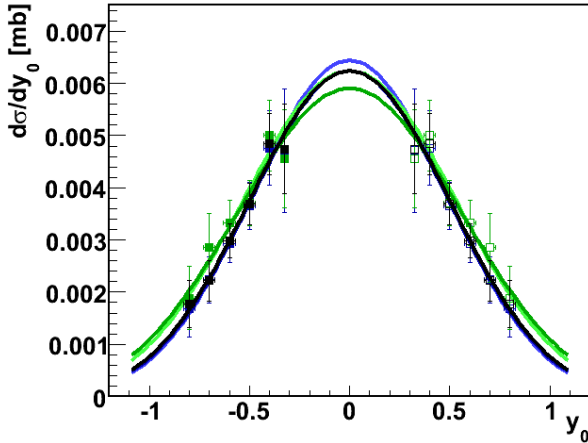
Figure 7.10: The rapidity-density distributions of K^+ mesons in C(2 AGeV) + C for three cases of p_t acceptance selection area. Black points are as in Fig. 7.5, while green and blue points correspond to lower and higher p_t selection ares, which are used for the study of systematical errors. The points extrapolated from measurements are shown with filled symbols, while the empty symbols represent the reflection with respect to midrapidity. The curves with corresponding temperature parameters are fits by Eq. (7.5).

Results of the fit for case *a*), normal case and case *b*) are $T_{\parallel}|_{a)} = (107 \pm 31)\,\text{MeV}$, $T_{\parallel}|_{exp} = (110 \pm 30)\,\text{MeV}$ and $T_{\parallel}|_{b)} = (142 \pm 53)\,\text{MeV}$. The point closest to midrapidity $(-0.35 < y_0 < -0.30)$ has low confidence level due to the large extrapolation to non-measured m_t region (see e.g. Fig. 7.1 and Fig. 7.2 for understanding of very limited acceptance in this case). Optionally, it can be excluded from the fit in this case[2]. The corresponding fits for cases *a*) and *b*) give slightly different temperature estimates: $T_{\parallel}|_{a)} = (102 \pm 32)\,\text{MeV}$ and

---

[2]In case of T_B distribution the influence of large extrapolation into non-measured m_t region has a much lower effect because only one parameter is extracted.

$T_\parallel|_{b)} = (127 \pm 86)\,\text{MeV}$. The obtained fits are exhibited as light-green and light-blue curves in Fig. 7.10 (hardly distinguishable from green and blue curves at this scale).

Taking these considerations into account, the longitudinal temperature estimate from the $d\sigma/dy_0$ yield according to a fit with Eq. (7.17) is $T_\parallel = (110 \pm 30^{+32}_{-8})\,\text{MeV}$. Large statistical and systematical errors in this case originate from the limited acceptance in m_t and the need of large extrapolations to non-measured regions.

For the case where the anisotropy with $a_2 = 0.54$ (as proposed by the KaoS experiment [Lau00]) is assumed, the corrected longitudinal temperature is $T_\parallel^{(a_2=0.54)} = (99 \pm 30^{+32}_{-8})\,\text{MeV}$. This result is in better agreement with the one obtained from T_B vs. y_0 distribution. This can be interpreted as a confirmation that the observed result is well explained with the help of anisotropy, possibly even on slightly higher level compared to the one reported by the KaoS experiment.

To provide an additional cross check of the normalization used in this chapter, the cross section estimates derived from $d\sigma/dy_0$ distribution corresponding to variations of acceptance intervals and fits (unconstrained and constrained to one of boundary values of one parameter from two possible parameters in Eq. (7.17) estimated from non-constrained fit) were performed. The resulting cross section is $\sigma_{K^+} = (7.7 \pm 3.3)\,\text{mb}$, where the error holds for the maximum deviation of the result with respect to mentioned fit procedures[3]. This result is in a good agreement with the one obtained in chapter 6 for isotropic emission, see Eq. (6.18). This ensures the consistency check of the differential spectra normalization.

The production cross section as well as the longitudinal and the transverse temperatures indicate a good agreement with the KaoS results, especially under the assumption of anisotropic emission of K^+ mesons produced in $C(2\,\text{AGeV}) + C$ reactions. Therefore, our experiment performed within a different phase space region and the corresponding analysis serves as an independent test of the earlier KaoS findings [Lau99, Lau00].

---

[3]If considered as a stand alone result for the cross section estimate the uncertainties due to the absolute normalization still have to be added here as in Eq. (6.18). Extrapolations involved into $d\sigma/dy_0$ distribution calculation result in large errors, which makes such an investigation useful only as a self consistency test.

8   Summary

Over the last decade, considerable efforts were put into the planning, construction, tuning and calibrating of the HADES detector. In this work, the data of the first beam time were used for the selection and analysis of the rare process of K^+ production in C+C collisions at kinetic beam energy of 2 AGeV. The analysis achievements covered in this thesis were:

- The quality-assessment software for the HADES data-summary-tapes production was improved. A semi-automatic off-line data-quality-control tool was proposed and realized in ROOT GUI classes enabling the end user interface to each of the data files in order to supervise the quality of the detector performance during whole time of the experiment. This allowed to select, among the amounts of data collected, those files with appropriate data quality for the actual analysis.

- The Runge-Kutta track-fitting algorithm was implemented into the official HADES analysis program and extensively tested. It considerably improved the performance of the high-resolution tracking with respect to momentum resolution and introduced a powerful background-rejection parameter, specific to the track fitting algorithm. This achievement opened the possibility of sufficient background suppression for the identification of rare probes without requiring dedicated trigger conditions in HADES. As a consequence of this work the Runge-Kutta tracking algorithm serves as the default momentum reconstruction method in the data analysis for many other processes in the HADES experiment.

- A HADES-specific K^+ particle identification procedure was developed, optimized and successfully applied for the analysis of the reaction data C + C at 2 AGeV. The introduced tracking algorithm provided high signal-to-background ratio for K^+ identification. Single K^+ tracks were identified in both time-of-flight detectors with high significance.

- An estimate of the K^+ production cross section was performed relying on the existing data of $\pi^{\pm}$ cross sections. The obtained result was found to be in a good agreement with the one obtained by the KaoS experiment in a narrower acceptance region.

- The collected statistics allowed for the estimate of the Boltzmann temperature parameter of the K^+ production from a wide rapidity region, which was found to be in a good agreement with the one measured around midrapidity at the same energy by the KaoS experiment. The estimated transverse and longitudinal temperature parameters support the assumption of non-isotropic emission of K^+ mesons in the center-of-mass system.

This work demonstrates the capabilities of the HADES experimental setup, especially in its tracking part, toward investigation of rare probes without dedicated trigger conditions applied. In addition, the analyzed production of K^+ mesons serves as an important complementary verification of the tracking possibilities of HADES with respect to the detection of light vector mesons via the electron/positron channel which exploit the same technique of momentum determination of charged tracks.

Appendix A   Implementation and tests of the Runge-Kutta tracking

In this appendix the survey of high and middle resolution cases of the Runge-Kutta tracking implementation into the official analysis software package of HADES experiment (HYDRA) is done. The corresponding mathematical formalism was described in section 4.3. The achieved momentum resolutions and systematical shifts are presented. The investigation of background rejection power and stability of the RK with respect to the initial momentum value delivered by either "Kick Plane" or "Spline Track" is provided.

A.1   High resolution case

The HADES spectrometer is designed for the case, when all four tracking detectors provide coordinate measurement for each track. The Runge-Kutta tracking takes a hit from MDC1 detector and starts track propagation inside the known magnetic field forward through MDC2, MDC3 and MDC4. As a starting point the MDC1 hit position is used. As initial direction a vector between two MDC hits from chambers before the magnetic field is used: $\vec{v}_{initial}/|\vec{v}_{initial}| = (\vec{hit}_{MDC2} - \vec{hit}_{MDC1})/|\vec{hit}_{MDC2} - \vec{hit}_{MDC1}|$. The starting value of the momentum of the particle is needed as well. It is taken from another tracking methods, either `HKickTrack` or `HSplineTrack`.

In principle, inside the Runge-Kutta tracking implementation there is even a small routine, which performs a rough estimate of initial momentum of the particle track based on the deflection of the particle trajectory in the magnetic field, where instead of the realistic magnetic field a very simple idealization with magnetic field located inside a very thin spatial region is used. The first-guess of the momentum can be obtained already within the Runge-Kutta tracking class, but it is not reliable for a fraction of about one third of all tracks due to simplicity of the idealization.

Historically, the Runge-Kutta tracking was implemented in the HADES analysis software after other tracking methods and there were no need in a developing a good momentum first-guess within Runge-Kutta class itself, because a much better momentum determination was already provided by "Kick Plane" and "Spline Track" methods. Hence, the initial momentum value for the fit performed by the Runge-Kutta tracking is obtained from another method for the track propagation inside the magnetic field. Indeed, this option is used in most cases.

The normalization of χ^2_{RK} is done for 4 existing MDC hits according to

$$\chi^2_{RK}/ndf = \frac{1}{ndf} \sum_{i=1}^{4} \left(\left(\frac{x_{tmi} - x_{hiti}}{\sigma_{xi}} \right)^2 + \left(\frac{y_{tmi} - y_{hiti}}{\sigma_{y_i}} \right)^2 \right),$$

where the sum runs over 4 MDC hits, "hit" stands for measured coordinates of MDC hits, and "tm" stands for "track model" coordinates. The number of degrees of freedom, ndf, consists of 8 measured coordinates {x,y} from four MDC hits minus five determined parameters $\{p, x, y, dx/ds, dy/ds\}$, i.e., $ndf = 2 * 4 - 5 = 3$.

A.2   Middle resolution case

In case when only 3 tracking detectors deliver hits, the situation is not so clear and it goes beyond the HADES specification. Nevertheless, in this case Runge-Kutta tracking can be applied as well, and it gives results of comparable quality with the four-points case. This will be shown in the forthcoming sections. In reality, the middle resolution case can be formulated as a set of the following MDC-hit combinations: {MDC123, MDC124, MDC234, MDC134}. There is no principal problem to propagate a track in case of 3 hits, the only drawback is that there is less information available, i.e. either before or behind the magnetic field the track position is measured only at one point. This follows from the realisation of the method which is based on the requirement of a realistic guess of initial parameters $\{p, x, y, dx/ds, dy/ds\}$, where the initial momentum may be taken from another tracking method but the initial direction vector of the track can be estimated only from one side of the track, depending on the side of the magnetic field from which we have information of two MDCs. Therefore, in cases of {MDC123, MDC124} the forward-track propagation is performed exactly like in the case of high resolution with 4 MDC hits (except of that the propagation is now done with 3 hits). But in cases of {MDC234, MDC134} a backward-track propagation is performed. Backward-track propagation uses the MDC4 hit position as the starting point. The direction vector is formed by two outer MDC hits, i.e. $\vec{v}_{initial}/|\vec{v}_{initial}| = (\vec{hit}_{MDC3} - \vec{hit}_{MDC4})/|\vec{hit}_{MDC3} - \vec{hit}_{MDC4}|$, and the track propagation is stopped when it reaches the surface of the first (counting from target) tracking detector which provided the hit information.

Since χ^2_{RK} for this case consists of 3 hits, it has to be properly normalized

$$\chi^2_{RK}/ndf = \frac{1}{ndf} \sum_{i=1}^{3} \left(\left(\frac{x_{tmi} - x_{hiti}}{\sigma_{xi}} \right)^2 + \left(\frac{y_{tmi} - y_{hiti}}{\sigma_{y_i}} \right)^2 \right),$$

where the sum runs over 3 MDC hits, the number of degrees of freedom, ndf, consists of six measured coordinates {x,y} from three MDC hits minus five determined parameters i.e. $ndf = 2 * 3 - 5 = 1$, the values x_{tm}, y_{tm} are fitted positions of the track model intersection with three MDC detectors, and x_{hit}, y_{hit} are corresponding measured hit coordinates.

A.3   Additional information

The main task of Runge-Kutta tracking is the momentum determination of the track. But it provides also a set of related values being very useful in the analysis of data. First of

all, χ^2_{RK}/ndf is delivered by the fit with a track model. In addition, after the momentum reconstruction has converged, the track propagation from first MDC backwards to z coordinate position of the target z_{target} is done. Also, forward track propagation from last MDC hit (MDC3 or MDC4) till the surface of the activated META subdetector (plane in space formed by TOF rod or TOFINO paddle delivering the corresponding META hit). From the forward propagation the values of residuals $dx = x_{META} - x_{RK}$, $dy = y_{META} - y_{RK}$, $dz = z_{META} - z_{RK}$ are stored among the output information to be used for additional cuts on matching between MDC and META detectors.

A.4   Debugging option

The HADES analysis is possible for both inputs, i.e. data taken from experiment and the data obtained from Monte Carlo simulation. The simulated data are produced with the hGeant package [Hol05] based on the GEANT 3.21 package [Gea93]. In case of an analysis of simulation data, some additional information available in GEANT is copied into an output file of analysis results in one of the HYDRA containers. This approach allows one to perform realistic simulations of the detector response as well as obtaining actual information from the simulation package. It can be used for debugging purposes and different kinds of tests of the analysis software.

An analysis based on simulated data uses the Runge-Kutta momentum reconstruction program allowing the user to store a special debugging NTuple (see ROOT Users Guide [Bru05] for more information on NTuple) in addition to the output of the HYDRA package. This NTuple allows to have a simple access to some auxiliary information available only inside the Runge-Kutta program and also from the simulation, using a special look-up method of HYDRA to access the information from GEANT KINE bank. This is done because one can not store all the information (including the debugging ones) inside the standard output of HYDRA for data size reasons[1].

Among the debugging information there are stored: 1) the most probable particle code (see GEANT particle codes [Gea93]) corresponding to the track crossing two MDCs before the magnetic field. In cases when several tracks were crossing two chambers almost at the same place, the track which has deposited signals at maximum number of wires in MDC1 and MDC2 provides the particle code. This means, that if in one or in both involved MDC hits there are wires deposited by different (for example very close in space) tracks, the most probable one is that which gives a signal in most wires after all cuts applied during the hit reconstruction algorithm (see HYDRA classes documentation [Mar] for more information). 2) Parameters of the direction vector of the MDC segment before the magnetic field for the most probable track (also looked up from the number of wires involved in the hit clusters in MDC1 and MDC2) provided by fitting a straight line using the first MDC segment (see HMdcSeg class for details). 3) Parameters of the direction vector of the MDC segment before the magnetic field for the most probable track (also looked up from the number of wires involved in the hit clusters in MDC1 and MDC2) provided by the track model fitting of Runge-Kutta tracking. 4) The momentum of the most probable particle in the point of its origin (vertex). 5) The momentum guess value provided by the tracking method called before Runge-Kutta tracking and used by Runge-Kutta tracking as a starting value

---

[1]This is a natural compromise between productivity and amount of data members stored.

for momentum propagation (if external tracking method was called for the first guess of momentum parameter[2]). 6) A momentum obtained from Runge-Kutta tracking/fitting. 7) χ^2_{RK}/ndf obtained from the particle trajectory fitting with Runge-Kutta.

When using simulated data, all these information can be used to provide tests of the Runge-Kutta tracking or to perform fine tuning and further developments.

A.5   Alignment consistency test option

Once the Runge-Kutta track model fitting converged, one can utilize information about displacements between the fitted position of a hit on an MDC detector middle plane and the measured MDC hit position. Plotting these displacement values for x and y coordinates versus a local coordinate system of MDC detectors one can observe sometimes that these displacements are different in different parts of the MDC detectors. This can be used as simple consistency check of the knowledge of the magnetic field and the quality of alignment of tracking detectors.

A.6   High resolution test

Tests of the Runge-Kutta resolution were performed using the debugging information, explained in the previous section for the case of four MDC hits attributed with the track hypothesis. To get the momentum resolution, a data sample simulated with Pluto and then propagated with hGeant with realistic parameters for the experiment C(2AGeV)+C (November 2002) was used. Momentum resolution tests were performed for tracks from different particle types determined by GEANT KINE based on an MDC segment before the magnetic field.

To get the momentum resolution, the following method was used. Certain particles, for example pions, were selected in different momentum ranges, say $50 < p < 150\,\mathrm{MeV/c}$, $150 < p < 250\,\mathrm{MeV/c}$, ... , $1950 < p < 2050\,\mathrm{MeV/c}$. For each momentum range the $\frac{p_{RK}-p_{Geant}}{p_{Geant}}$ distribution was plotted. A Gaussian fit around the peak position gives an optimistic estimate of the momentum resolution. Examples are exhibited in Fig. A.1. The same procedure was repeated for proton tracks.

To summarize these results, the momentum resolution of Runge-Kutta tracking for pions and protons is presented in Fig. A.2 as a function of the momentum value from GEANT KINE (corresponding to the MDC segment before the magnetic field). In Fig. A.3 the χ^2_{RK}/ndf distributions for pions and protons are shown.

In Fig. A.4, the θ and ϕ dependences of the momentum resolution for charged pions are presented (GEANT KINE identification related to MDC segment before the magnetic field was used). No additional cuts were applied.

A.7   Influence of initial guess of momentum

In this paragraph the stability of Runge-Kutta momentum reconstruction with respect to the initial guess of the momentum is tested. The simulation of Nov02/gen2 data set was

---

[2]It was mentioned that the Runge-Kutta tracking has its own possibility to estimate the initial guess of the momentum parameter in case of 4 MDC hits, but it is not optimized in the present implementation.
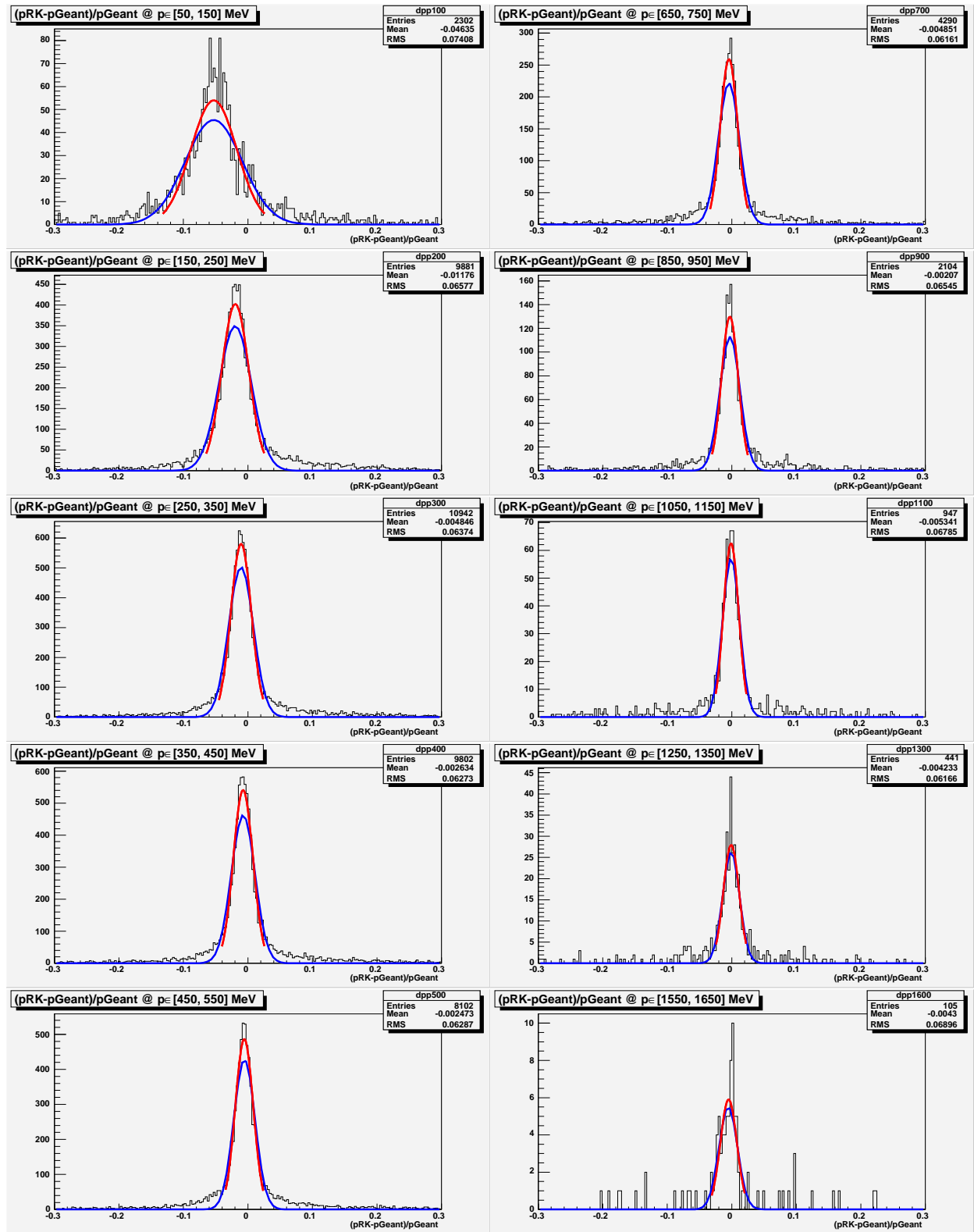
Figure A.1: Examples of MDC1234 Runge-Kutta tracking. The distribution of $\frac{p_{RK}-p_{Geant}}{p_{Geant}}$ as a function of p_{Geant} within different momentum regions for π^+ and π^-. The Gaussian width of the red curve was used for an estimate of the momentum resolution. The selection of particles is done using GEANT KINE information corresponding to the tracklet formed by MDC1-MDC2 hits. For details see text.
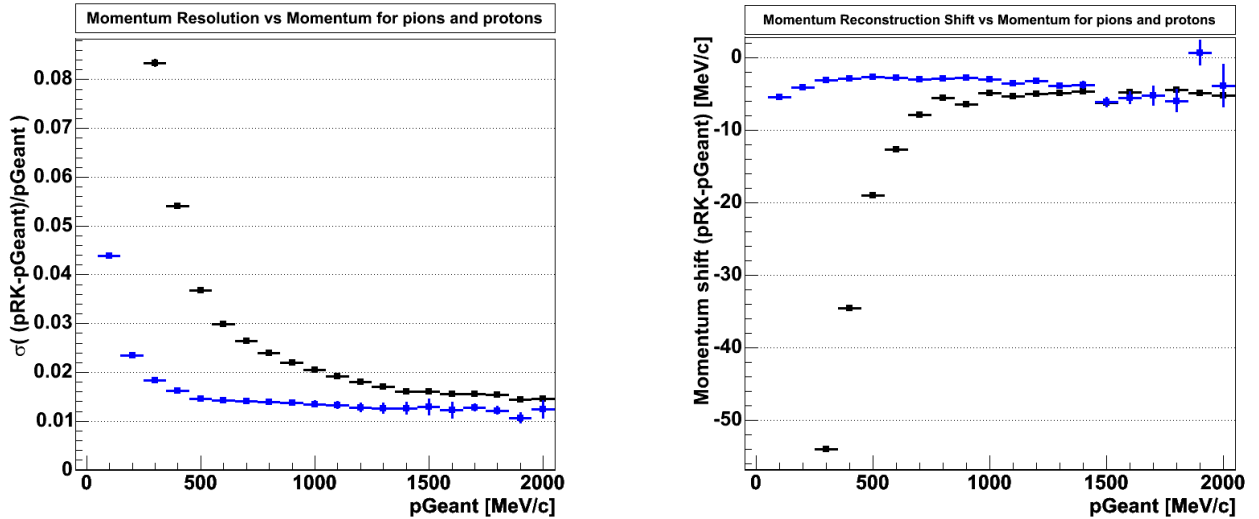
Figure A.2: Left panel: Estimate of the momentum resolution with Runge-Kutta (MDC1234) tracking for momentum range $p = 100 \cdots 2000\,\mathrm{MeV/c}$. Right panel: Estimate of momentum shift compared to actual momentum value at the target point as a function of momentum. In both figures, data for pions and protons are shown by blue and black symbols, respectively.
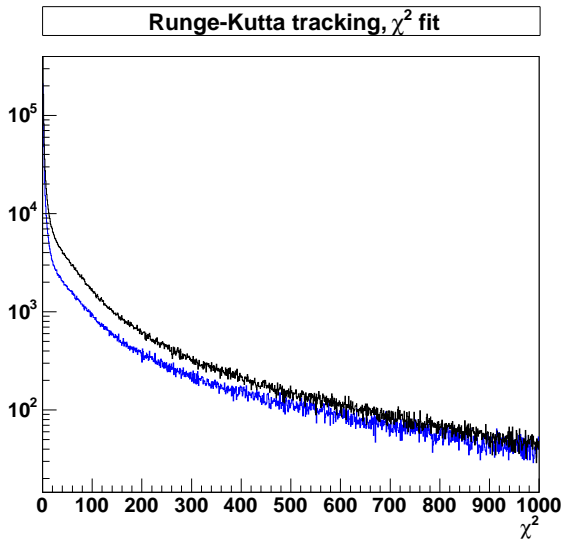
Figure A.3: The distribution of χ^2_{RK} with Runge-Kutta (MDC1234) tracking for pions (blue histogram) and for protons (black histogram).

analyzed.

The influence of the initial momentum guess on the result of 4-MDC Runge-Kutta tracking was investigated when running two tasks in parallel. One task used Runge-Kutta tracking starting from a momentum provided by the "Kick Plane" algorithm; another task implied Runge-Kutta tracking with the initial momentum taken from "Spline Track". No particle identification and no special selection cuts were applied for this investigation. The only requirement was that both the "Kick Plane" and the "Spline Track" methods provided the momentum reconstruction.

The distributions of the difference between the reconstructed momentum and an ideal momentum, taken from GEANT KINE at the target point for the two methods "Kick Plane" and "Spline Track" are presented in Fig. A.5.
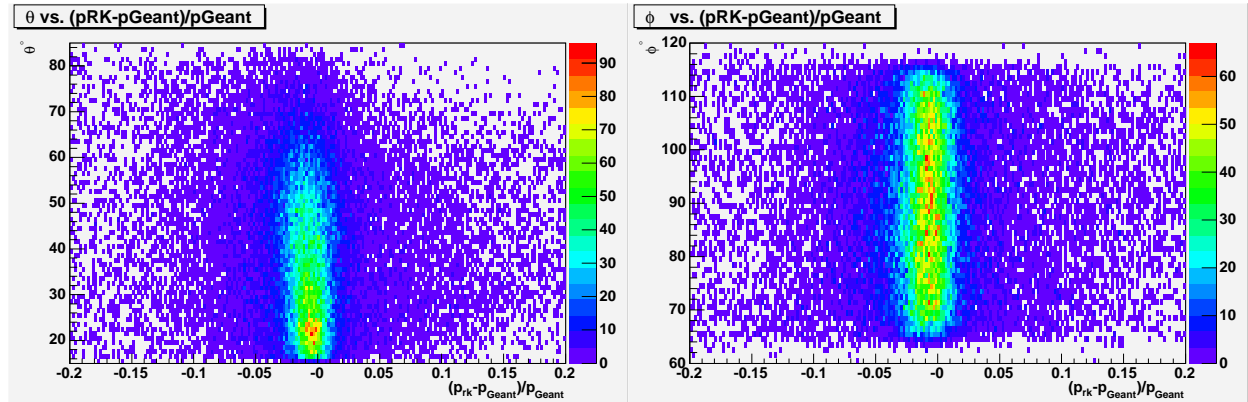
Figure A.4: Momentum resolution for pions with Runge-Kutta (MDC1234) tracking depending on θ (left panel) and ϕ (right panel).
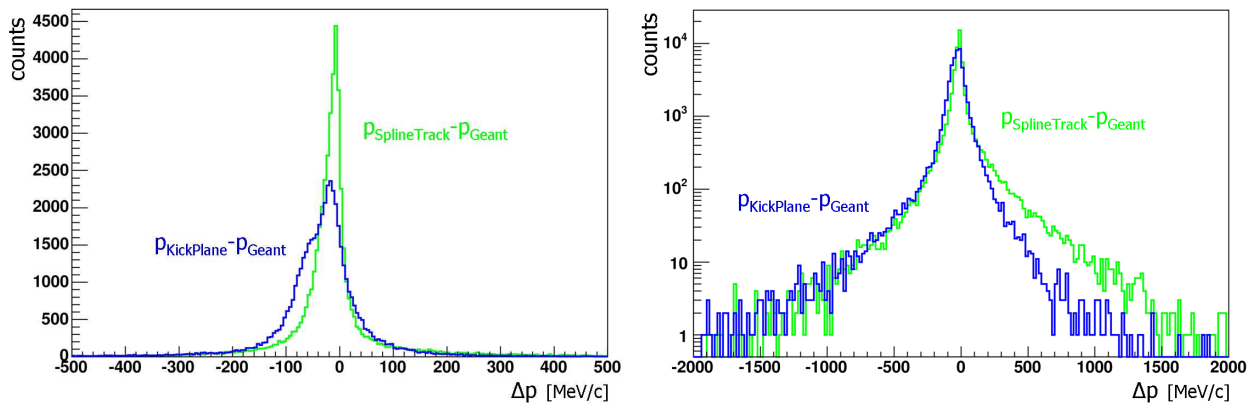
Figure A.5: Distributions of $p_{KickPlane} - p_{Geant}$ (green histogram) and $p_{SplineTrack} - p_{Geant}$ (blue histogram). The GEANT momentum is taken at the target point. Only the tracklets which were registered in four MDCs and the META detector were taken into account. Left figure is in linear vertical scale, while the right figure shows the same distribution in logarithmic scale for a much wider interval.

In Fig. A.6 one can see how the momentum taken from the high resolution "Kick Plane" is used by Runge-Kutta tracking as initial value and gets adjusted. In addition, the effect of the background suppression by a $\chi^2_{RK}/ndf < 10$ cut is indicated by a different color.

In Fig. A.7 one can see how the initial momentum taken from "Spline Track" is used by Runge-Kutta tracking and gets adjusted. In addition, the background suppression by applying the $\chi^2_{RK}/ndf < 10$ cut is indicated.

Fig. A.8 indicates that Runge-Kutta tracking, when started from different initial guesses of momentum provided by both "Kick Plane" and "Spline Track" methods converges to the same value in more than 99.9 % of samples. In that case, two requirements were applied: the first one is that only the tracks with four MDC hits were analysed, and the second one is that "Kick Plane" and "Spline Track" methods both have delivered the momentum estimate. All calculations in this section are made with Runge-Kutta internal step size (along the track path) of 20 mm.
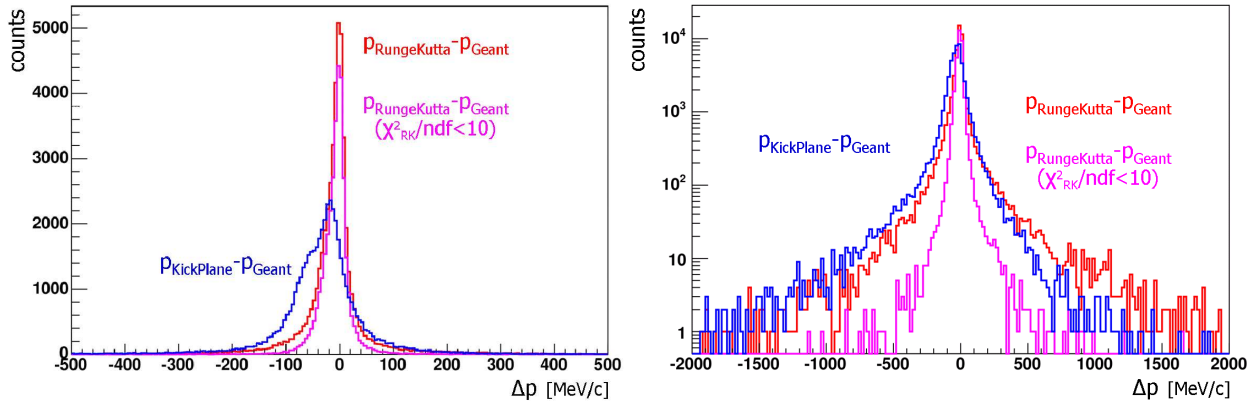
Figure A.6: Distributions of $p_{method} - p_{Geant}$ are shown. The "Kick Track" method corresponds to the blue histogram, the result of Runge-Kutta method corresponds to the red histogram, while the Runge-Kutta with additional cut on $\chi^2_{RK}/ndf < 10$ is represented by magenta histogram. Left and right figures exhibit same distributions presented in linear and logarithmic scales.
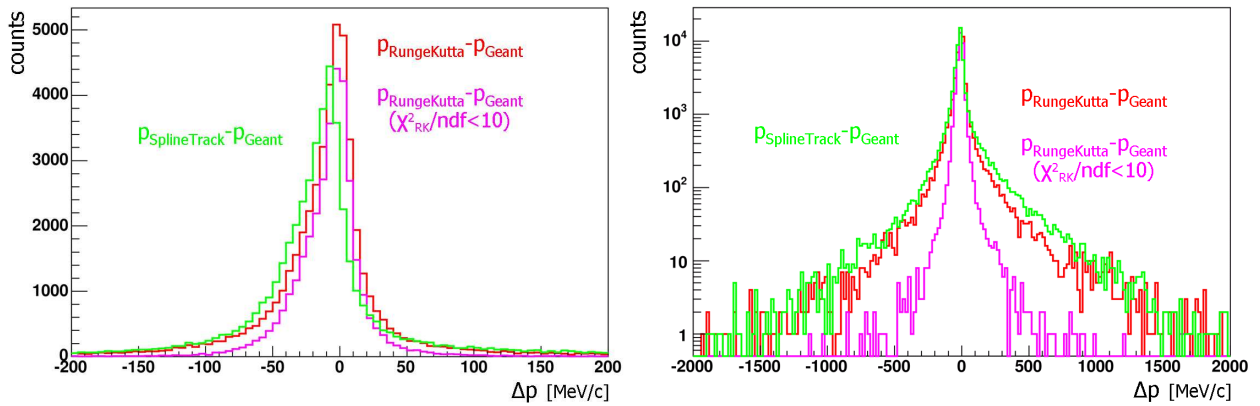
Figure A.7: The same procedure as in Fig. A.6 for "Spline Track", which is depicted by the green histogram.
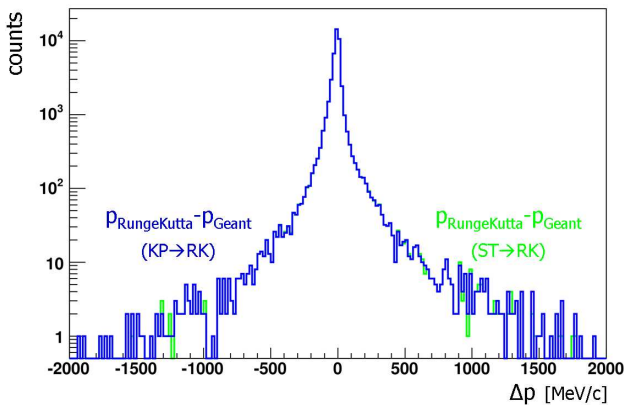
Figure A.8: $p_{RungeKutta} - p_{Geant}$ distributions. Blue histogram: initial momentum guess is taken from "Kick Plane". Green histogram: initial momentum guess is taken from "Spline Track". Only the tracks for which both "Kick Plane" and "Spline Track" algorithms provided the momentum are shown. The agreement between distributions proves that the Runge-Kutta tracking is stable with respect to the method used for the initial momentum guess.

A.8 The rejection power of wrongly matched tracklet combinations

In our simulations with subsequent HYDRA analysis we have an access to the GEANT KINE container from both inner and outer MDC segments (HMdcSeg1 and HMdcSeg2) which gives us the possibility to check the GEANT track IDentification number (ID). If the GEANT track ID taken from the first MDC segment is the same as the track ID from the second MDC segment one can suppose a real tracklet combination (based on MDC12-MDC34 hits). A fake track is a combination where GEANT track ID in the first and second MDC segments are not the same. This includes wrongly matched combinations of tracklets before and after the magnetic field and also combinations of tracks from particles which decayed somewhere inside the tracking path of the HADES detector, i.e. true tracks belonging to the same initial particle, but, in some of the tracking detectors, represented by one of its charged products. An example is the $\pi^\pm$ meson decay $\pi^\pm \to \mu^\pm \nu_\mu$, where the $\pi^\pm$ meson tracklet was measured before the decay in first HMdcSeg1 and a μ lepton from the decay of this pion was measured in outer segment MDC34.

Let us now consider the $\chi^2_{RK}/ndf < 10$ cut on Runge-Kutta track fit quality and compare this cut as a separation tool for real and for fake tracks, see Table A.1. One learns that the cut $\chi^2_{RK}/ndf < 10$ suppresses fake tracklet combinations by a factor of about 9 times more than the suppression of real tracklet combinations by the same χ^2_{RK} cut.

π tracks from	Cut effect $\dfrac{N(\frac{\chi^2_{RK}}{ndf} < 10)}{N(\frac{\chi^2_{RK}}{ndf} < \infty)}$
real combinations	0.573
fake combinations	0.067
real/fake suppression ratio	9.39

Table A.1: The χ^2/ndf rejection power for the case of MDC1234 Runge-Kutta tracking.

A.9 Middle resolution test: MDC123 combination

In case when the tracking is done with not fully equipped setup of MDC detectors (where the last MDC4 was inefficient) or the detector was not yet installed in the setup, one can use a reduced Runge-Kutta propagation through 3 MDCs {MDC123}. The quality of momentum reconstruction and also the selection quality based on the χ^2_{RK} cut are not as powerful compared to the high resolution case (with four measured points). The dedicated tests show that resolution decreases only by a factor $1.2\cdots1.8$ compared to the high resolution case.

The resolution tests were performed on the same data sample as for the high resolution case. In addition, a moderate cut of $\chi^2_{RK}/ndf < 10$ was applied to reject badly fitted track candidates[3].

---

[3] This is important because one accounts for a possible situation where two hits before the magnet can

The momentum range was divided from $50\,\mathrm{MeV/c}$ up to $2050\,\mathrm{MeV/c}$ into 20 intervals: $50\text{-}150\,\mathrm{MeV/c}$, $250\text{-}350\,\mathrm{MeV/c}$, ..., $1950\text{-}2050\,\mathrm{MeV/c}$. For each interval the $\frac{p_{RK}-p_{Geant}}{p_{Geant}}$ distribution was fitted by a Gaussian, around the peak of the distribution for each momentum interval. This allows us to estimate an "optimistic" momentum resolution. The examples of corresponding fits are exhibited in Fig. A.9. The same procedure was repeated for proton tracks.

A summary plot for the momentum resolution for pions using Runge-Kutta tracking with MDC1, MDC2 and MDC3 as a function of momentum value from GEANT KINE (corresponding to the HMdcSeg1 tracklet) as well as the mean shift value of reconstructed momentum compared to the original momentum from GEANT is shown in Fig. A.10.

In Fig. A.11, the θ and ϕ angular dependences of momentum resolution for charged pions (GEANT KINE identification related to HMdcSeg1 was used) is presented. A moderate cut $\chi^2_{RK}/ndf < 10$ was applied to reject badly resolved tracks.

A.10   The rejection power of wrongly matched tracklet combinations for MDC123

As mentioned above, real and fake tracklet combinations are subject of special separation power of the cut on χ^2_{RK}/ndf provided within the Runge-Kutta tracking/fitting routine. The effect of this quality cut for different thresholds is presented in Tab. A.2. One can see that the rejection power for three MDCs is not as good as for four MDCs. But still, an additional background suppression power of about $6-7$ times while keeping 59% of statistics can be provided.

	Cut effect			
Tracks from	$\dfrac{N(\frac{\chi^2_{RK}}{ndf}<0.9)}{N(\frac{\chi^2_{RK}}{ndf}<\infty)}$	$\dfrac{N(\frac{\chi^2_{RK}}{ndf}<3)}{N(\frac{\chi^2_{RK}}{ndf}<\infty)}$	$\dfrac{N(\frac{\chi^2_{RK}}{ndf}<5)}{N(\frac{\chi^2_{RK}}{ndf}<\infty)}$	$\dfrac{N(\frac{\chi^2_{RK}}{ndf}<10)}{N(\frac{\chi^2_{RK}}{ndf}<\infty)}$
real combinations	0.587	0.699	0.738	0.79
fake combinations	0.09	0.13	0.15	0.19
real/fake suppression ratio	6.52	5.37	4.92	4.15

Table A.2: The χ^2_{RK}/ndf rejection power for MDC123 Runge-Kutta tracking for different cut values.

A.11   Middle resolution test: MDC234, MDC134 and MDC124 combinations

When MDC1 was inefficient, one has to use a dedicated Runge-Kutta tracking with first MDC disabled. The same testing scheme (as for MDC123 combination) was applied for the

---

be matched with only one hit behind the magnet. For two hits before and two hits after the magnetic field the matching possibility is of much higher significance due to the fact that the track curvature in magnetic field is measured with sufficient lever arm from both sides. Therefore an additional cut on χ^2_{RK} is needed in case of only three measured points to reject obviously wrong tracklet combinations.
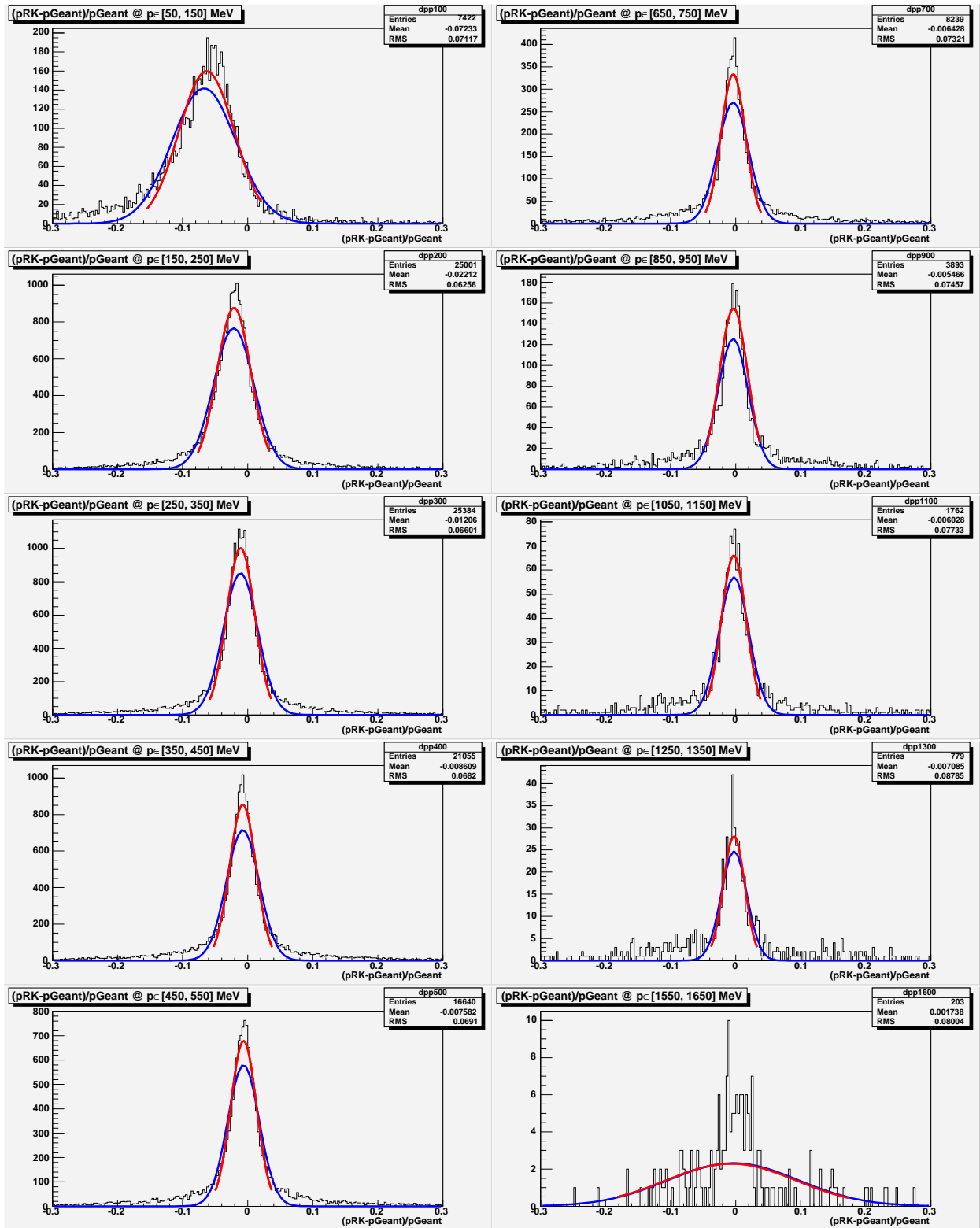
Figure A.9: Examples of MDC123 Runge-Kutta tracking: $\frac{p_{RK}-p_{Geant}}{p_{Geant}}$ for π^+ and π^- within different momentum regions. The Gaussian width of the red curve was used for an estimate of momentum resolution. Selection of pions is done using GEANT KINE corresponding to tracklet formed by MDC1-MDC2. A moderate cut of $\chi^2_{RK}/ndf < 10$ was applied to reject badly resolved tracks.
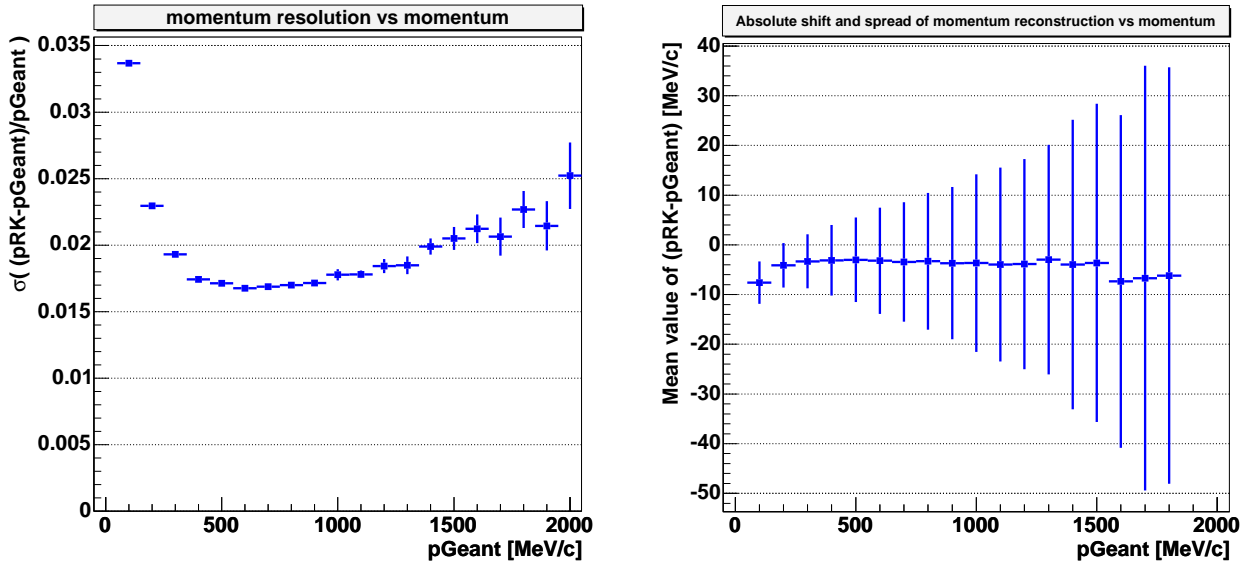
Figure A.10: Left panel: An estimate of momentum resolution for Runge-Kutta (MDC123) tracking in the momentum range $p \in [100 - 2000]\,\mathrm{MeV/c}$. A moderate $\chi^2_{RK}/ndf < 10$ cut was applied to reject badly resolved tracks. Right panel: A systematics of shifts of reconstructed momentum, compared to original momentum from GEANT KINE at the vertex point. As an error, the 1σ deviation of the absolute difference between the momentum reconstructed with Runge-Kutta tracking and the original GEANT momentum is assigned. Both figures are for $\pi^{\pm}$ mesons.
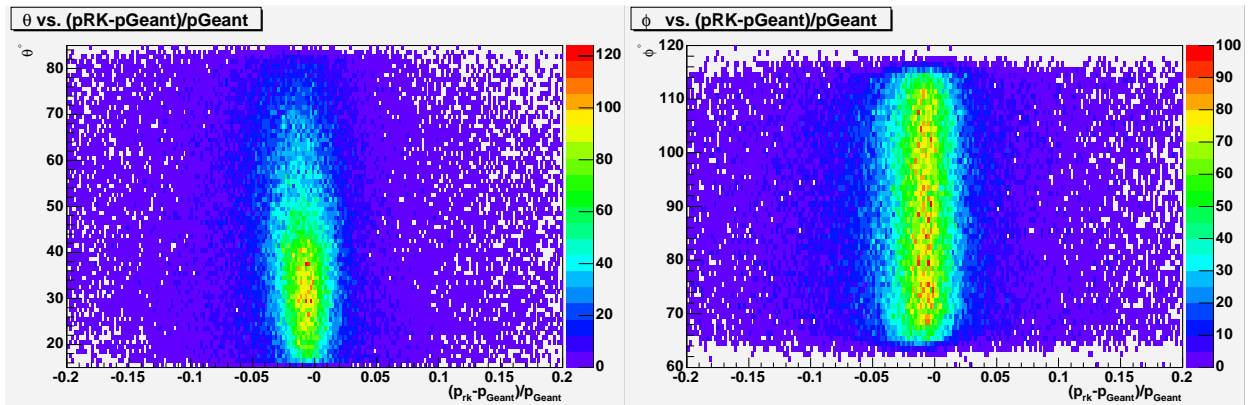
Figure A.11: Momentum resolution for Runge-Kutta (MDC123) tracking depending on angles θ (left) and ϕ (right). A moderate cut on $\chi^2_{RK}/ndf < 10$ was applied to reject badly resolved tracks.
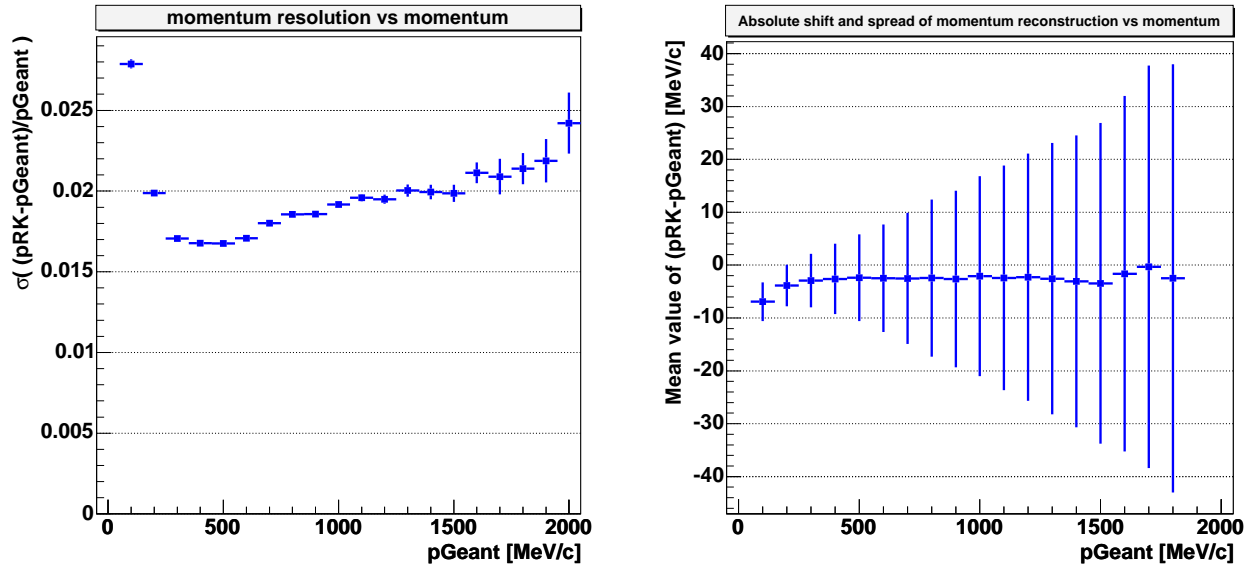
Figure A.12: An estimate of momentum resolution and shift for Runge-Kutta (MDC234) hit combinations. See also Fig. A.10.
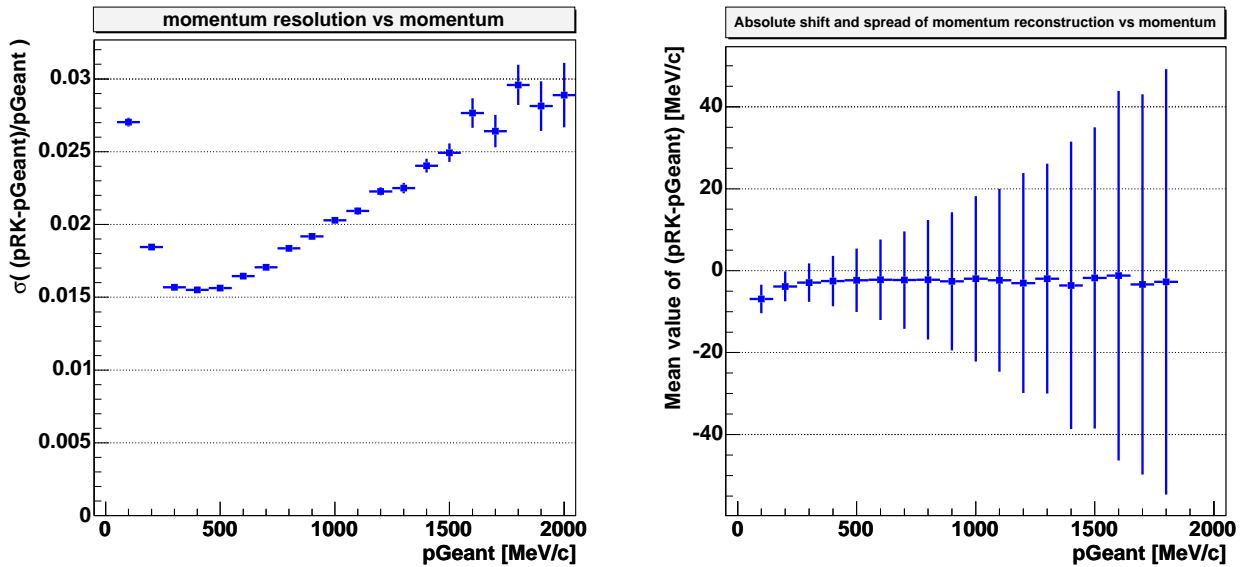
Figure A.13: Same as Fig. A.12, but for (MDC134) combinations.

momentum resolution test: 10^7 pion tracks were generated in Pluto, propagated through GEANT and afterwards analyzed with HYDRA, assuming MDC1 to be switched off. The resulting momentum dependences of the resolution and shifts of the reconstructed momentum are exhibited in Fig. A.12.

In cases where MDC2 was inefficient, one has to use dedicated Runge-Kutta tracking with second MDC disabled. The corresponding analysis with HYDRA, assuming MDC2 to be switched off was performed. The results are presented in Fig. A.13.

In cases where MDC3 was inefficient, one has to use dedicated Runge-Kutta tracking with third MDC disabled. The corresponding results are presented in Fig. A.14.
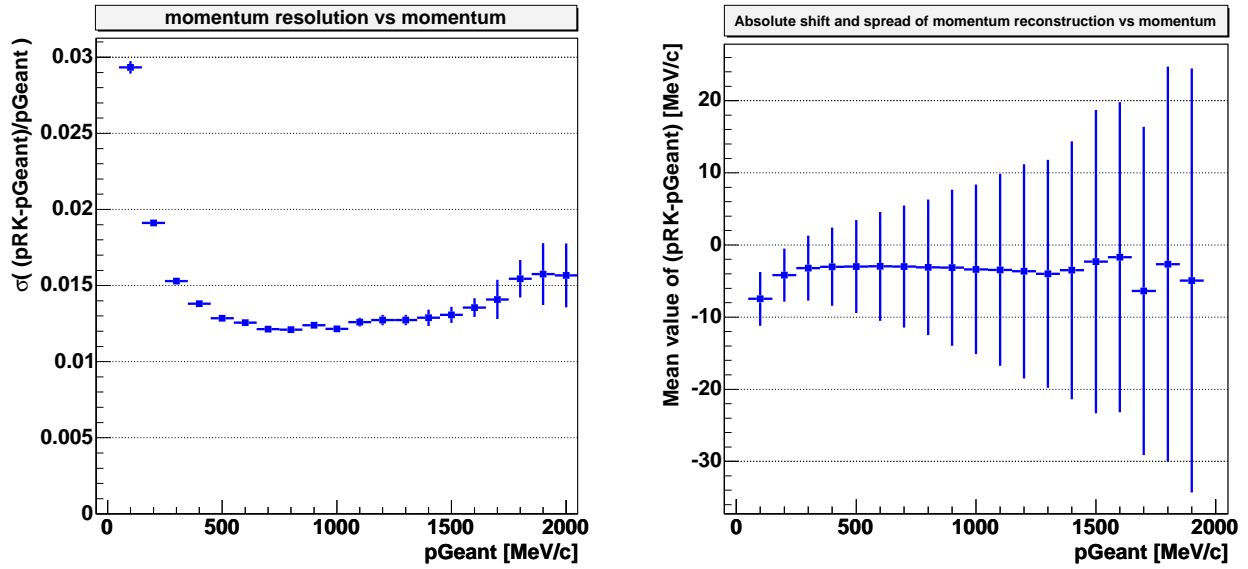
Figure A.14: Same as Fig. A.12, but for (MDC124) combinations.

A.12   Performance

The performance of Runge-Kutta tracking is about 400 tracks per second tested with a personal computer based on the AMD Barton processor 2500+. The efficiency of single track reconstruction with hit combinations obtained from real tracks when starting from good initial values guess is close to 100%. The mean track multiplicity per event in the HADES acceptance for $C + C$ at $2\,AGeV$ is below four charged particles without multiplicity trigger condition and below seven charged particles in case of trigger multiplicity of at least 4 charged particles (estimated by a UrQMD simulation). Providing six sectors of the detector one would be faced with an average sector multiplicity of well below two charged per sector. Thus, there is no inefficiency expected due to high track occupancy for the case of single track reconstruction in this particular experiment. The background suppression power of the Runge-Kutta tracking is demonstrated in practice in chapter 5 for the selection of K^+ tracks in inclusive $C + C \rightarrow K^+ + X$ production.

Appendix B Number of participants and the impact parameter

In this appendix the average number of participants produced in C+C collisions as a function of maximum impact parameter is presented. The often used approach based on geometrical model of interpenetrating spheres [Bar97, Bar05], see Fig. B.1, is followed here. That means that only the nucleons in the overlap region react with each other. This approximation was applied to scale the data taken with the multiplicity trigger to the minimum bias condition in subsection 6.3.4 of this thesis.

Figure B.1: A sketch of two nuclei before and after collision. The impact parameter quantifies the number of participants A_{part} affected in the geometrical overlap region of the reaction. The model allows prediction of the functional dependence of the number of participants on the impact parameter.

An inelastic reaction between two colliding nuclei can occur only in case of some overlap region, which sets the upper limit for the impart parameter $b < b_{UpLim} = R_P + R_T$, here R_P and R_T are radii of projectile and target nuclei.

The number of secondary particles produced in central collisions depends on the centrality of the event. The more central the collision is, the higher the multiplicity of produced particles is. This relation is exploited in multiplicity trigger concept. The multiplicity trigger is often used as a minimum threshold to some fixed number of secondary particles detected in certain acceptance. The (minimum) threshold of the multiplicity trigger corresponds in average to certain value of maximum impact parameter $< b_{max} >$ defining events centrality enough for the sufficient secondary particle production. In this sense, $b_{max} < b_{UpLim}$ except for the case when no multiplicity/centrality trigger is applied, in which $b_{max} = b_{UpLim}$.

Hence, the events collected with a certain multiplicity trigger have their impact parameters randomly distributed within $0 < b < b_{max}$, which means that the multiplicity is an average value in this range of impact parameters. The average number of participants A_{part} corresponding to $< b_{max} >$ defined by the trigger settings can be calculated with help of the

geometrical model of interpenetrating spheres. The Fig. 6.3.4 corresponds to the calculations done for carbon-carbon system analyzed in this thesis. The limit $b_{max} \to 0$ corresponds to the very central collisions trigger, while $b_{max} = 2R_C$ corresponds to minimum bias events, i.e. events without any trigger conditions applied.
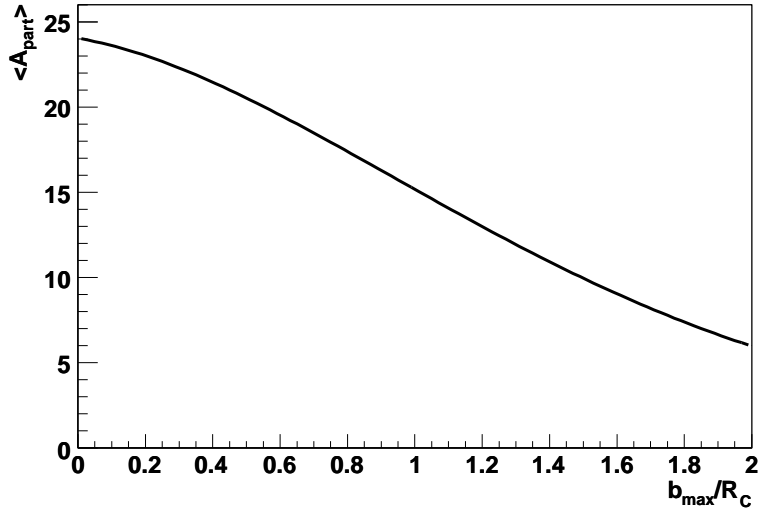
Figure B.2: The average number of participants A_{part} as a function of the maximum allowed impact parameter b_{max} for carbon-carbon collisions according to the model of interpenetrating spheres. The plot is presented in relative units b_{max}/R_C, where R_C is the radius of carbon nucleous. The upper value of b_{max} allowing interactions requiring that two nuclei at least touch each other, which implies $b_{max} \leq 2R_C$ in our case.

Appendix C   Functionality of post analysis DST QA

In this appendix the functionality of the developed *histogram history* tool for general Quality Assessment post analysis is described. The *histogram history* is operated from its menu and consists of four logical levels (organized as different pages). On the first page, the user specifies the location of ROOT files, containing QA histograms[1]. In addition the filename mask of the QA output ROOT-file has to be specified, see Fig. C.1.

In the left panel of Fig. C.1 the user has to select one histogram to be analyzed among the available files set, listed in the right panel. It is always possible to inspect a special histogram from a certain file just by selecting one histogram and one file from the panel on the second page called "hi/file". The file-by-file scanning page for a given histogram is possible on the third page, called "HH-player". This page contains all the functionality from well known video/audio players, namely "Play", "Fast Forward", "Fast Backward", "Pause" and "Stop". In addition, it has several buttons oriented to Quality Assessment, namely "One File Forward", "One File Backward" and three qualification/mark buttons "Good", "Warning" and "Bad", with corresponding colors green, orange and pink, respectively. The status of this histogram/file appears in the colored light indicator which is green on the

---

[1]QA histograms are created by another program. In HADES it is done in parallel with DST production for each of the data files.
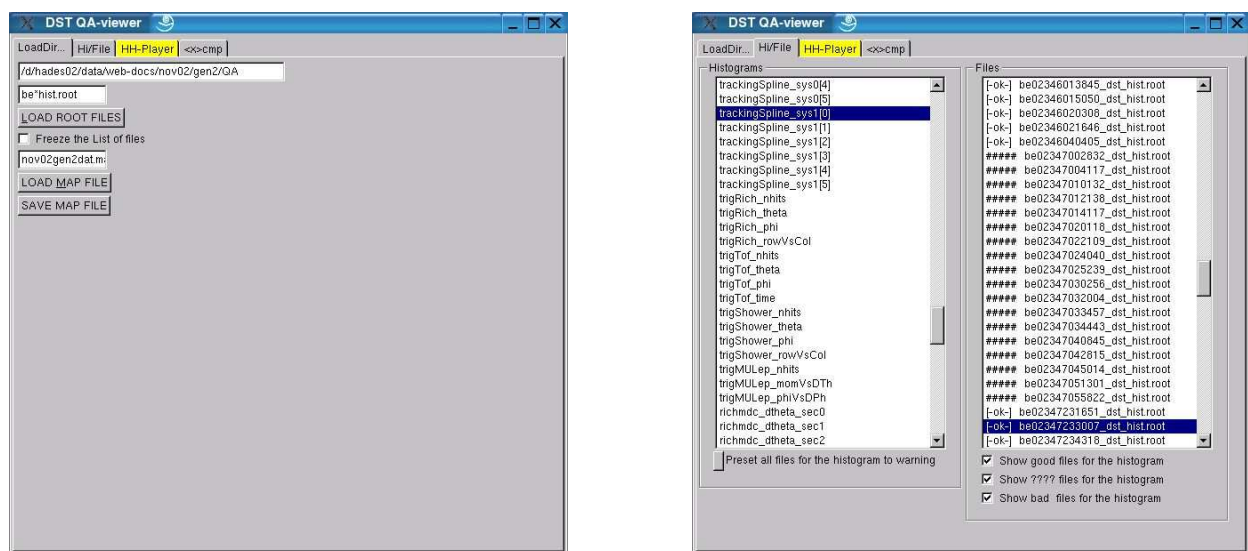
Figure C.1: The *histogram history* tool for offline QA diagnostics. Initialization page (left), and histogram/file selection page (right).

picture showing MDC hit distribution for second MDC plane (i.e. MDC2), see Fig. C.2. Initially all the files for each histogram are assumed and marked as "Good". Normally, the
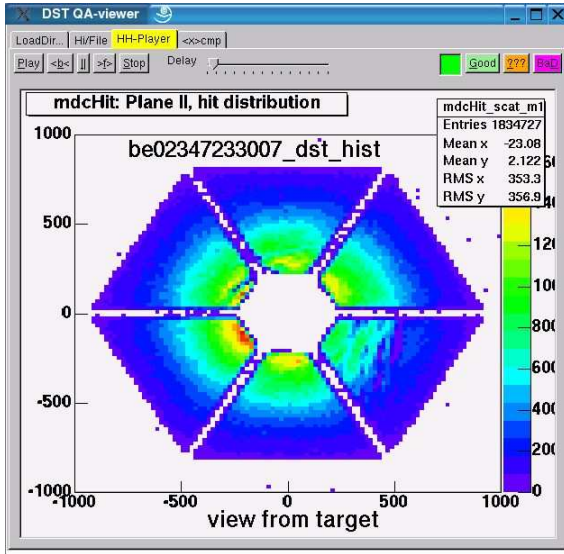
Figure C.2: The *histogram history* tool for off-line QA diagnostics. Shown is the histogram/history player page, allowing fast scanning among hundreds of diagnostic files with the standard set of histograms. The scanning is performed for one histogram at a certain time in experiment. The user can manually qualify a histogram for the currently "played" file. In this example the distribution of hits on the MDC2 plane is shown for the data file `be02347233007.dst`.

user scans one of the histograms along all available files from some sample (e.g. a certain experiment). The user can interrupt the scanning procedure at any time if a problem occurs, and specify a "Warning" or "Bad" flag for the file. But for certain classes of histograms such a visual observation might be insufficient. For one-dimensional histograms, where a distribution (e.g. a peak or a structure) is monitored it might be important to observe minor fluctuations of a peak position, the mean value of a certain distribution or the position of some structure. For this reason, an automatic and more accurate tool has been implemented, namely a mean value scanner for a certain range in a one-dimensional histogram. The automatic mean value scanner page is illustrated on Fig. C.3.

This method is implemented as a single file of a compiled ROOT macro which only works with ROOT-files containing a standard set of histograms. The application area of such diagnostic files containing the standard set of diagnostic plots is common for many experiments and the *histogram history* program can be used for all of them. In a way, this development is beyond the official HADES software HYDRA. It can be used in any other experiment without any changes if the corresponding analysis is based on ROOT software.
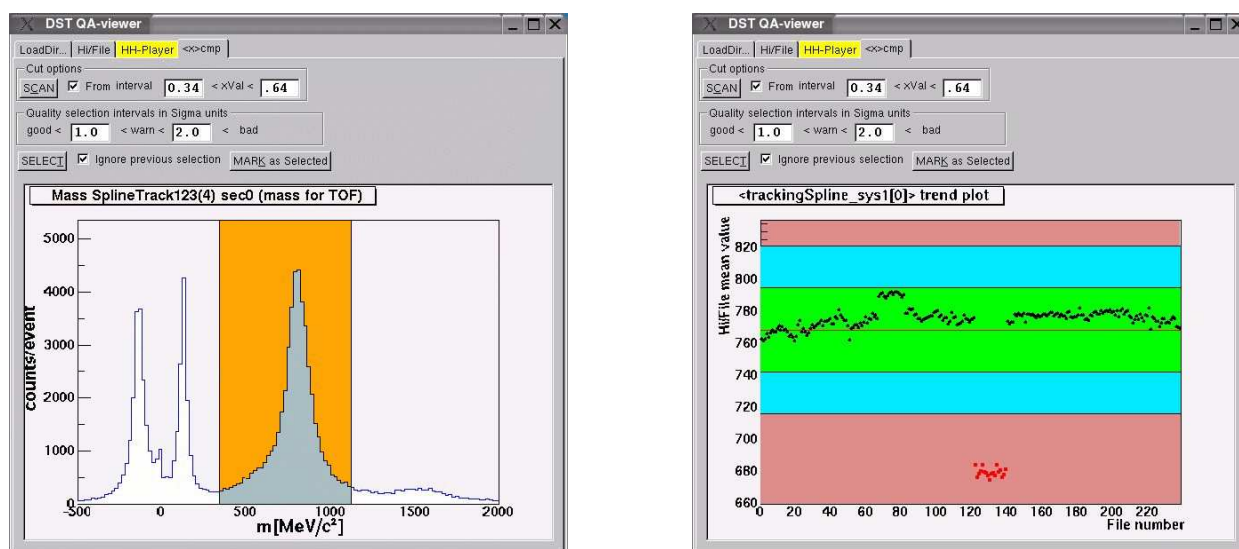
Figure C.3: The *histogram history* tool for offline QA diagnostics. This example illustrates the automatic scanning procedure applied to monitor the shape of a distribution inside an interval for a one dimensional histogram. The left panel is used to select the interval for the scanning procedure and also to specify the range of the deviations from the mean value to be attributed to "Good", "Warning" and "Bad" preselections. In the right panel the result of such preselections is presented with help of color bands. In this example a proton mass position is monitored as a course of file number. A reason for fluctuations is an instability of calibration of TOF-Start detectors. Red points on the right panel are caused by a set of files collected without target. Obviously, the mass peak of protons is not present in these files and the mean value scanner just indicated this change in the distribution. This picture illustrates the power of this simple method for quality assessment applications.

Acknowledgements

Bibliography

[Abb90a] T. Abbott et al., *Phys. Rev. Lett.* 64:847, 1990.

[Abb90b] T. Abbott et al., *Phys. Rev. Lett.* 64:847, 1990.

[Abr64] M. Abramowitz, I.A. Stegun, *Applied Mathematics Series.* 55:§25.5, 1964.

[Ada05] J. Adams et al., *Nucl. Phys.* A757:102, 2005.

[Aga00] G.N. Agakishiev et al., *Particles and Nuclei, Letters.* No.4[101]:54, 2000.

[Aga01] G.N. Agakishiev, V.N. Pechenov, *Intrenal HADES report*, 2001.

[Ago02] C. Agodi et al., *Nucl. Inst. Meth.* A494:14, 2002.

[Ahl98] L. Ahle et al., *Phys. Rev.* C58:3523, 1998.

[Ahl99] L. Ahle et al., *Phys. Rev.* C60:044904, 1999.

[Ahn97] W. Ahner et al., *Phys. Lett.* B393:31, 1997.

[Aic85a] J. Aichelin, C. M. Ko, *Phys. Rev. Lett.* 55:2661, 1985.

[Aic85b] J. Aichelin, C.M. Ko, *Phys. Rev. Lett.* 55:2661, 1985.

[Ale80] G.D. Alekseev et al., *Nucl. Inst. Methods.* 177:365, 1980.

[Ani82] M. Anikina et al., *JINR report (in Russian).* P1-82-333:1, 1982.

[Ani83] M. Anikina et al., *Phys. Rev. Lett.* 50:1971, 1983.

[Ars05] I. Arsene et al., *Nucl. Phys.* A757:1, 2005.

[Ata82] M. Atac et al., *Nucl. Inst. Methods.* 200:345, 1982.

[Ave97] R. Averbeck, *Mont Sainte Odile, France, Sept* 1997.

[Bac02] B. Back et al., *Phys. Rev. Lett.* 89:222301, 2002.

[Bal04] A. Balanda et al., *Nucl. Instrum. Meth.* A531:445, 2004.

[Bar97] R. Barth et al., *Phy. Rev. Lett.* 78:4007, 1997.

[Bar05] H.W. Barz, *Private communication*, 2005.

[Bas98] S.A. Bass et al., *Prog. Part. Nucl. Phys.* 41:225–370, 1998.

[Ber99]   E. Berdermann et al., *Nucl. Phys. (Proc. Suppl.).* B78:533, 1999.

[Bes97]   D. Best, et al., *Nucl. Phys.* A625:307, 1997.

[Bie61]   E. Bierman, et al., *Phys. Rev.* 147:922, 1961.

[Bin86]   F. Binon et al., *Nucl. Instr. Methods.* A248:86, 1986.

[Bra95]   P. Braun-Munzinger et al., *Phys. Lett.* B344:43, 1995.

[Bre99]   T. Bretz, *Ph.D. thesis.* Physik Department der Technischen Universitäet München, 1999.

[Bro84]   R. Brockmann et al., *Phys. Rev. Lett.* 53:2012, 1984.

[Bro91]   G.E. Brown, M. Rho, *Phys. Rev. Lett.* 66:2720, 1991.

[Bru05]   R. Brun et al., *http://root.cern.ch/* Users Guide v3.10, 2005.

[Bue96]   M. Buescher et al., *Z. Phys.* A355:93, 1996.

[Bug81]   L. Bugge, J. Myrheim, *Nucl. Inst. and Meth.* 179:365, 1981.

[Böh99]   M. Böhmer, *Diploma Thesis.* Physik Department der Technischen Universität München, 1999.

[Cas99]   W. Cassing, E.L. Bratkovskaya, *Phys. Rept.* 308:65, 1999.

[Che34]   P.A. Cherenkov, *Dokl. Akad. Nauk SSSR.* 2:451, 1934.

[Cse94]   L.P. Csernai, *John Wiley & Sons, Chichester.* ISBN 0471934208:310, 1994.

[Deb96]   M. Debowski et al., *Z. Phys.* A356:313, 1996.

[Dov77]   C.B. Dover, P.J. Moffa, *Phys. Rev. C.* 16:1087, 1977,

[Dov82]   C.B. Dover, G.E. Walker, *Phys. Rep..* 89:1, 1982,

[Ead71]   W.T. Eadie et al., *North-Holland Publishing Company,* 1971.

[Eid04]   S. Eidelman et al., *Phys. Lett.* B 592:1, 2004.

[Elm96]   R. Elmer et al., *Phys. Rev. Lett.* 77:4884, 1996.

[Eva97]   D. Evans, *Acta Phys. Slov.* 47:35, 1997.

[Fab03]   L. Fabbietti, *Ph.D. thesis.* Technischen Universität München, 2003.

[Fon01]   P. Fonte, *Nucl. Instr. Methods.* A478:170, 2001.

[Fri99]   J. Friese et al., *Nucl. Instr. Methods.* A438:86, 1999.

[Fuc97]   C. Fuchs et al., *Phys. Rev.* C56:606, 1997.

[Fuc01]   C. Fuchs et al., *Phys. Rev. Lett.* 86:1974, 2001.

[Fuc06]   C. Fuchs, *Prog. Part. Nucl. Phys.* 56:1, 2006.

[Gar98]   C. Garabatos et al., *Nucl. Instr. Methods.* A412:38, 1998.

[Gar03]   M. Sánchez García. *Ph.D. thesis.* Universidada de Santiago de Compostela, 2003.

[Gar05]   J. Garzón, *HADES XV collaboration meeting in Dubna.* Status report, 2005.

[Gaz96]   M. Gazdzicki, D. Rohrich, *Z. Phys.* C71:55, 1996.

[Gea93]   *CERN Program Library Long Writeup.* W5013, 1993.

[Gel68]   M. Gell-Mann et al., *Phys. Rev.* 175:2195, 1968.

[Gle01]   N. K. Glendenning, F. Weber, *Lect. Notes Phys.* 578:305, 2001.

[Gol02]   M. Golubeva et al., *INR preprint N° 1090*, 2002 (in russian).

[Gol05]   M. Golubeva, *Private communication*, 2005.

[GQL95]   C.M. Ko G.-Q. Li, *Phys. Lett.* B349:405, 1995.

[GSI]   GSI, *http://www.gsi.de/*

[Hag68]   R. Hagedorn, J. Ranft, *Nuovo Cim. Suppl.* 6:169, 1968.

[Har81]   J.W. Harris et al., *Phys. Rev. Lett.* 47:229, 1981.

[Har06]   Ch. Hartnack et al., *Phys. Rev. Lett.* 96:012302, 2006.

[Her96]   N. Herrmann, *Nucl. Phys.* A610:49c, 1996.

[Hog68]   W.J. Hogan et al., *Phys. Rev.* 166:1472, 1968.

[Hol05]   R. Holzmann, *http://www-hades.gsi.de/~holzmann/hadsimul.html* 2005.

[Hon98a]   B. Hong et al., *Phys. Rev.* C57:244, 1998.

[Hon98b]   B. Hong et al., *Phys. Rev.* C57:244, 1998.

[Hua94]   H. Z. Huang et al., *Phys. Rev.* C49:314, 1994.

[Kag00]   M.A. Kagarlis, *GSI report.* 03 Juli, 2000.

[Kag05]   M.A. Kagarlis et al., *http://www-hades.gsi.de/computing/pluto/html/PlutoIndex.html* 2005.

[Kan96]   J. H. Kang et al., *KEK Experiment E246 Technical Note.* 87, 1996.

[Kan06]   K. Kanaki, *Ph.D. thesis.* Technischen Universität Dresden, 2006.

[Kas00]   A. Kastenmueller, *Ph.D. thesis.* Technischen Universität München, 2000.

[Koc97]   V. Koch et al., *Ann. Rev. Nucl. Part. Sci.* 47:505, 1997.

[Kol95]   E.E. Kolomeitsev et al., *Nucl. Phys.* A588:889, 1995.

[Kur88]   A.B. Kurepin et al., *JETP Lett.47:17-22,1988, Pisma Zh.Eksp.Teor.Fiz.47:16-19,1988.* 47, 1988.

[Lan76]   L.D. Landau et al., *Nauka Publishing Company, Moscow.* p.1:1, 1976.

[Lau99]   F. Laue et al., *Phys.Rev.Lett.* 82:1640, 1999.

[Lau00]   F. Laue et al., *Eur.Phys.J.* A9:397, 2000.

[Lee96]   C.H. Lee, *Phys. Rept.* 275:255, 1996.

[Leh99]   J. Lehnert et al., *Nucl. Instrum. Meth.* A433:268, 1999.

[Leh00]   J. Lehnert, *Ph.D. thesis, II Physikalisches Institut, Justus Liebig Universität Giessen,* 2000.

[Leh03]   J. Lehnert et al., *Nucl. Instrum. Meth.* A502:261, 2003.

[Leo87]   W. Leo, *Springer-Verlag,* 1987.

[Lin01]   E. Lins, *Ph.D. thesis, II Physikalisches Institut, Justus Liebig Universität Giessen,* 2001.

[Lou61]   R.I. Louttit et al., *Phys. Rev.* 123:1465, 1961.

[Mag02]   P. Magierski, P.-H. Heenen, *Phys. Rev. C.* 65:045804, 2002.

[Mar]   J. Markert et al., *http://www-hades.gsi.de/docs/hydra/classDocumentation/*

[Mar05]   J. Markert, *Ph.D. thesis.* Johann Wolfgang Goethe-Universität in Frankfurt am Main, 2005.

[Men00]   M. Menzel, et al., *Phys. Lett.* B495:26, 2000.

[Mer04]   M. Merschmeyer, *Ph.D. thesis.* Ruperto-Carola University of Heidelberg, 2004.

[Mis94]   D. Miskowiec et al., *Phys. Rev. Lett.* 72:3650, 1994.

[Muh74]   K.N. Muhin, *Atomizdat, Moscow.* vol II:1, 1974.

[Mün]   C. Müntz et al,. *Nucl. Instr. Methods.* A734:78-81, 2004.

[Pan95]   V.S. Pantuev et al., *Nucl. Phys.* A585:13c, 1995.

[Par98]   Particle Data Group, *Eur. Phys. J.* C3:1, 1998.

[Pet98]   C. J. Pethick, A. Y. Potekhin, *Phys. Lett. B.* 427:7, 1998.

[Pet00]   M. Petri, *Ph.D. thesis, II Physikalisches Institut, Justus Liebig Universität Giessen,* 2000.

[Pie04]   J. Piekarewicz, *Phys. Rev.* C69:041301, 2004.

[Pre92]   W. Press et al., *Cambridge University Press.* page 707, 1992.

[Ray03]   L. Ray at al. *http://www.star.bnl.gov/STAR/comp/qa/* 2002, 2003.

[Ree68]   J.T. Reed et al., *Phys. Rev.* 168:1495, 1968.

[Rit95]   J.L. Ritman et al., *Z. Phys.* A352:355, 1995.

[Rup06]   J. Ruppert et al., *Phys. Rev.* C73:034907, 2006.

[Rus03]   A. Rustamov, *http://www-hades.gsi.de/mdc/note-01-03.pdf* HADES internal report, 2003.

[Sch82]   S. Schnetzer et al., *Phys. Rev. Lett.* 49:989, 1982.

[Sch89]   S. Schnetzer et al., *Phys. Rev.* C40:640, 1989.

[Sch94]   J. Schaffner et al., *Phys. Lett.* B334:268, 1994.

[Sch95]   W. Schön, *Ph.D. thesis.* Institut für Kernphysik, Johann Wolfgang Goethe-Universität, Frankfurt am Main, 1995.

[Sch96]   R. Schicker et al., *Nucl. Instr. Meth.* A380:586, 1996.

[Sch97]   J. Schaffner et al., *Nucl. Phys.* A625:325, 1997.

[Sch00]   W. Scheinast. *Acta Phys. Polon.* B31:2305, 2000.

[Sch06]   W. Scheinast et al., *Phys. Rev. Lett.* 96:072301, 2006.

[Sen99]   P. Senger, H. Ströbele, *J. Phys. G: Nucl. Part. Phys.* 25:R59, 1999.

[Sen01]   P. Senger al. *Nucl. Phys.* A685:312, 2001.

[Sen06]   P. Senger, *Acta. Phys. Pol.* B36:115, 2006.

[Shi98]   Y. Shin et al., *Phys. Rev. Lett.* 81:1576, 1998.

[Sho82]   A. Shor et al., *Phys. Rev. Lett.* 48:1597, 1982.

[Ste92]   M. Steiner et al., *Nucl. Instrum. Meth.* A312:420, 1992.

[Sto86a] R. Stock, *Phys. Rept.* 135:259, 1986.

[Sto86b] H. Stoecker, W. Greiner, *Phys. Rept.* 137:277, 1986.

[Sto98]   R. Stock, *Nucl. Phys.* A630:535c, 1998.

[Str98]   J. Stroth, *Vienna.* 19:103, 1998.

[Stu01a] C. Sturm, *Technische Universität Darmstadt.* Ph.D. thesis:99, 2001.

[Stu01b] C. Sturm et al., *Phys.Rev.Lett.* 86:39, 2001.

[Toi04]   A. Toia, *Ph.D. thesis.* II Physikalisches Institut, Justus Liebig Universität Giessen, 2004.

[Uhl05]   F. Uhlig et al., *Phys. Rev. Lett.* 95:012301, 2005.

[Ull96]   T. Ullrich et al., *Nucl. Phys.* A610:317c, 1996.

[Waa96]   T. Waas et al., *Phys. Lett.* B379:34, 1996.

[Wei96]   W. Weise, *Nucl. Phys.* A610:35c, 1996.

[Win74]   H. Wind, *Nucl. Inst. Meth.* 115:431, 1974.

[Wüs05]   J. Wüstenfeld, *Ph.D. thesis.* Johann Wolfgang Goethe-Universität in Frankfurt am Main, 2005.

[You99]   D. H. Youngblood et al., *Phys. Rev.* C60:067302, 1999.

[Zsc02]   S. Zschocke et al., *Contributed to 40th International Winter Meeting on Nuclear Physics. Bormio. Italy*, 2002.

[Zum05]   P. Zumbruch, *Ph.D. thesis.* Fachbereich Physik der Technischen Universität Darmstadt, 2005.